Velocity & Vorticity Transport In 3D-Printed Idealized & Realistic Human Airways Using Magnetic Resonance Velocimetry (MRV) & Particle Image Velocimetry (PIV)

A DISSERTATION
SUBMITTED TO THE FACULTY OF THE GRADUATE SCHOOL
OF THE UNIVERSITY OF MINNESOTA
BY

Sahar Jalal

IN PARTIAL FULFILLMENT OF THE REQUIREMENTS
FOR THE DEGREE OF
DOCTOR OF PHILOSOPHY

Advisor: Professor Filippo Coletti

July, 2019

Acknowledgements

This dissertation is the accumulation of 5 years of research done at the Aerospace Engineering and Mechanics (AEM) department in collaboration with the Center for Magnetic Resonance Research (CMRR). None of this work would have been possible without the support of many individuals in and outside of the lab.

My advisor, Professor Filippo Coletti, who continues to spark my curiosity about fluid mechanics. I am grateful for his mentorship and guidance during the past few years. Through our interactions, and his constant drive and ambition, I became a better scientist, a more determined researcher and most importantly, a good science communicator. I am thankful for his patience, friendship, support and the many, many stimulating conversations we had throughout the years.

I would like to thank my committee members: Professor Ellen Longmire, Professor Joe Nichols and Professor Pierre-Francois Van De Moortele for their insightful feedback and the invaluable lessons learned in their lectures and through our exchanges. Thank you to my colleagues: Dr Ute Goerke for teaching me everything I know about Magnetic Resonance Imaging (MRI), Dr Andras Nemes, Dr Omid Amili and Tristan Van De Moortele for their help setting up experiments and making it through the overnight MRI scans.

I am extremely grateful for my undergraduate liberal arts education at Grinnell College which instilled in me a strong sense of social justice I could extent to the science community. More specifically, I would like to thank my undergraduate advisor, Professor William B. Case for giving me my first opportunity to do research: I am forever grateful for his guidance, wit, friendship and for our endless conversations at Lonnski's! His love and dedication to physics fueled my passion for science.

Additionally, I want to express my gratitude to all the women in STEM I had the pleasure to meet: in my cohort (Luci Baker, Yi Hui Tee and the women in AEM), through my work with the Women in Science and Engineering (WISE) initiative and in various national and international conferences. Thank you for inspiring me, challenging me, encouraging me throughout the years and giving me a sense of community when I needed it the most; I wouldn't be here without you.

I would also like to thank Professor Josue Sznitman at the Israel Institute of Technology (Technion) for the opportunity to visit his lab during the summer of 2018 and join our efforts to further our understanding of respiratory fluid mechanics. I truly appreciated the opportunity to learn from his expertise and explore the scientific and cultural facets of this collaboration.

Last but certainly not least, I would like to thank my support system: my family back in Morocco and my friends all over the world. I am forever grateful for my parents' unwavering love, for their personal, financial and emotional sacrifices, my brother and sister for continuously inspiring me to be a better person and sibling, and my friends, for indulging me, encouraging me, keeping me grounded and giving me a home away from home. I am so lucky to have you all in my life.

Dedication

To my family, Souad, Noureddine, Rita, Mehdi and Aicha; this is for you and because of you.

Abstract

Furthering our knowledge of respiratory fluid dynamics is greatly beneficial to understanding lung diseases and improving aerosol drug delivery and mechanical ventilatory techniques. To this end, we develop an in-vitro platform to study detailed flow features in human airways. Idealized and realistic replicas of the bronchial tree are inserted in a flow loop circulating aqueous fluid, and detailed information on the structure-function relationship is collected using Magnetic Resonance Velocimetry (MRV) and refractive-index-matched Particle Image Velocimetry (PIV). By structure here we indicate the anatomical and morphological features, while function refers to momentum transport and mixing. We extract and analyze velocity and vorticity fields, as well as flow descriptors that characterize the longitudinal and lateral dispersion along the bronchial tree. We consider regimes of steady inhalation, steady exhalation, and oscillatory ventilation for a range of physiologically relevant Reynolds (Re = 100 - 5000) and Womersley (Wo = 1.2 - 12) numbers. Longitudinal dispersion is found to be higher during inhalation, while lateral dispersion is higher during exhalation. Counter-rotating streamwise vortices are observed along the airway tree due to the local curvature of the branches (Dean mechanism) and constitute one of the main transport mechanisms. At the higher Re, however, inertia induces significant non-local effects, and the vortices are transported across successive generation of bronchial branching. Flow reversal, a phenomenon consequential for gas mixing, particle transport and mechano-transduction at the epithelium, is also identified in both idealized and realistic airway geometries during steady and oscillatory regimes. The net flow drift during the ventilation cycle (steady streaming) is experimentally evaluated for the first time, and found to be much smaller than the advective flow, although not insignificant for the realistic airway geometry. The instantaneous flow fields and Reynolds stresses measured in the idealized airway model indicate great sensitivity to the inflow conditions, and show that the flow at the bifurcation is prone to unsteadiness even at regimes sometimes treated as laminar in earlier numerical studies.

Contents

List of Tables

List of Figures

Chapter 1

Introduction

1.0.1 Motivation

Respiratory diseases are among the leading causes of death today. According to the World Health Organization, Chronic Obstructive Pulmonary Disease (COPD) alone is projected to be the 3rd cause of death in the world by 2030. To assess the severity of a lung condition and/or its response to a treatment, lung functionality is typically monitored by spirometry, which measures the air flow during standardized breathing maneuvers. This is a black-box approach, whose interpretation is ambiguous and primarily based on empirical correlations (White, 2005). Due to an incomplete understanding of the relation between airway deformation and respiratory flows, airway diseases often go undiagnosed (Hnizdo et al., 2006). Additionally, aerosol drug delivery devices have deposition efficiencies below 30%, and medical imaging techniques applied to living patients (in-vivo) cannot provide detailed information on the air flow within the complex network of bronchi. Consequently, in this study, we try to develop a better understanding of respiratory fluid dynamics and its relationship with the structure of the bronchial tree, in both idealized and patient-specific airway models. We exploit advanced imaging techniques to collect detailed information on the structure-function relationship in the human airways. The structure here indicates anatomical and morphological features while the function refers to air flow, mixing and particle transport. Unfortunately, working with human subjects to collect this type of data can be complicated because the

duration, accuracy, repeatability and sometimes even sheer feasibility of detailed respiratory flow measurements is difficult if not impossible. To overcome these obstacles, we created an in-vitro platform featuring 3D printed lung models in which an aqueous working fluid is circulated to mimic the airflow. This allows us to explore all flow features in a safer and more controlled setting. Two kinds of imaging techniques are used here: first, we leverage the world-class facilities available at the Center for Magnetic Resonance Research (CMRR) and use Magnetic Resonance Velocimetry (MRV, Elkins & Alley, 2007) to acquire 3D flow measurements in the upper and central human airways (from the trachea up to the first ~ 7 generations of bronchial branching). While MRI in an excellent technique to study 3-dimensional features of complex flows, it remains a time average method which does not capture any instantaneous flow characteristics that could be crucial to transport mechanisms. To this end, we also design and build a refractive-index matched 2D Particle Image Velocimetry (PIV, Raffel et al. 2007) setup to use with our 3D printed models. This approach, while restricted to only extract 2D velocity information, allows us to study unsteadiness and turbulence effects. Several transport mechanisms are present, the relevance of each being dependent on the regime and the direction of breathing (inhalation vs exhalation, steady vs oscillatory). These mechanisms include advection by the bulk flow, longitudinal dispersion (due to variations of streamwise velocity along a given cross section), lateral dispersion (due to secondary flows), steady streaming (due to non-reversible fluid trajectories during the respiration cycle), turbulent diffusion, and molecular diffusion. The relative contributions of each mechanism have important consequences for gas exchange (Golshahi and Finlay 2009), and the details of the flow at the various regimes need to be well captured to reach a predictive understanding of the transport and deposition of spherical and non-spherical particles in the lungs (Kleinstreuer and Feng 2013).

1.0.2 Thesis outline

The vast majority of past respiratory flow studies have focused on the inhalation phase. Already in his classic review, Pedley (1977) wrote: "*A disproportionately small amount of work has been done on expiratory flow patterns. It is as if everyone doing a model experiment on inspiration ran out of time or energy when it came to repeat the measurements for expiration.*".While the expiratory fluid mechanics has great physiological

importance, the trend reported by Pedley has not substantially changed in the last 40 years. Motivated by the need to investigate respiratory fluid dynamics during both inspiratory and expiratory phases, the current study deals with respiratory flows in two main geometries: an idealized double bifurcation model (more formally introduced later on as the Weibel model) with canonical dimensions that isolate the curvature and branching effects; and a patient-specific healthy airway geometry to capture the influence of streamwise-plane bifurcations, varying branching angles, asymmetric branches with realistic boundary conditions. We first start with steady inhalation and steady exhalation (chapter 2) in the Weibel model using MRV to collect 3D flow measurements of streamwise and secondary velocities, streamwise vorticity and track the evolution of these features with increased inertia. In chapter 3, we tackle the same geometry but throughout the breathing cycle, alternating between inhalation and exhalation. Here, we explore the effects of respiration frequency, ranging from regular breathing ventilation to high-frequency ventilation. Following the idealized model, and still using MRV, in chapter 4 we explore similar transport mechanisms but this time in a patient-specific airway geometry, under steady inhalation, steady exhalation and high-frequency ventilation. Finally, in chapter 5, we introduce a PIV setup specifically designed to investigate evidence of unsteady effects on the main flow features during steady inhalation for the idealized model. The dissertation concludes with a summary of the current findings and recommendations for future work.

Chapter 2

Steady inhalation & exhalation in the Weibel geometry

2.1 Overview

The lung anatomy is a fairly complex network of branching airways. While the actual anatomy varies between different subjects, general features have been long identified which are remarkably consistent: at the ith bronchial generation, the daughter-to-mother branch diameter ratio is $h = D_i + 1/D_i \approx 0.85$, the length-to-diameter ratio of each branch is $L_i/D_i \approx 3.5$, and the bifurcation angle is $\theta \approx 60^\circ - 70^\circ$ (Pedley 1977; Weibel 1997; Mauroy et al. 2004). Such proportions minimize the through-flow time during the respiration process (Sapoval and Filoche 2013), and the diameter ratio is close to the value of $(1/2)^{1/3} = 0.79$ which minimizes the energy expenditure in bifurcating flow systems (Murray 1926). It is therefore not surprising that canonical airway models with such characteristics have been extensively studied. The most classic case is the planar version of the Weibel A model (Weibel 1963), in which the branches consist of circular tubes that bifurcate symmetrically and lay on the same plane. Despite the simplicity of such representation, it has been shown to capture many key aspects of the respiratory airflow (Pedley 1977; Grotberg 2001) and to display fairly complex features (Kleinstreuer and Zhang 2010). A characteristic trait of the inspiratory flow through the bronchial tree is that, in general, both the streamwise velocity and the local diameter decrease at each branching generation. Assuming a symmetric flow distribution at

each bifurcation, this results in a decrease of the Reynolds number of order $2 \times h$ per generation. Therefore, while the flow in the trachea is typically transitional or turbulent (Re = 1000 - 5000 depending on the breathing pattern), the rapid decrease in Reynolds number for $h \approx 0.85$ suggests it becomes laminar after a few bifurcations.

Several transport mechanisms are present, the relevance of each being dependent on the regime and the direction of breathing (inhalation vs exhalation). These mechanisms include advection by the bulk flow, longitudinal dispersion (due to variations of streamwise velocity along a given cross section), lateral dispersion (due to secondary flows), steady streaming (due to non-reversible fluid trajectories during the respiration cycle), turbulent diffusion, and molecular diffusion. The relative contributions of each mechanism have important consequences for gas exchange (Golshahi and Finlay 2009), and the details of the flow at the various regimes need to be well captured to reach a predictive understanding of the transport and deposition of spherical and non-spherical particles in the lungs (Kleinstreuer and Feng 2013).

The state of the knowledge on flows in bifurcating airway models builds on a significant number of experimental and numerical studies. Although the inhalationexhalation dynamics can play an important role already at moderate ventilation frequencies, the respiratory flow can be considered quasi-steady as long as the Womersley number $Wo = D_i/2\sqrt{(\omega/\nu)}$ is comparable to or smaller than unity (Zhang and Kleinstreuer 2002; Fresconi and Prasad 2007; Theunissen and Riethmuller 2007). Here, ω is the angular frequency of oscillation and is the kinematic viscosity.

Steady inhalation is relevant, for example, to the deep-breath inhalation maneuvers in aerosol drug delivery. Schroter and Sudlow (1969) and Pedley et al. (1971) were among the first to experimentally investigate the flow in bifurcating tubes using geometrical proportions and regimes appropriate to respiration, studying planar symmetric (Weibel-type) models in the range Re = 1001400 (defined at the mother branch). By using hot wire and flow visualization, they highlighted the key features of the inspiratory flow: the boundary layers forming on the inside walls of the bifurcation (carina), the separation on the outer wall of the bifurcation, and the Dean-type secondary flows set up by the branch curvature and generating counterrotating streamwise vortices. Measurements reported by Pedley (1977) and Isabey and Chang (1982) using two-wire and slanted hot-wire probes included secondary flow profiles in symmetric and asymmetric

models, with Reynolds numbers in the range Re = 460 -1060. The maximum secondary velocity ranged between 13% and 30% of the axial velocity depending on the radius of curvature (which in most models is typically 510 times larger than the airway radius, in keeping with anatomical observations).

The flow pattern was found to be significantly more complex after the second bifurcation, due to the influence of upstream flow features interacting with the successive airway branching. Zhao and Lieber (1994) used laser Doppler velocimetry (LDV) to measure axial and secondary velocity profiles in a single symmetric bifurcation over the range Re = 518 - 2089. They confirmed that the axial velocity profiles in the daughter branches are skewed toward the inner wall and found secondary motions already at the beginning of the turn. Fresconi and Prasad (2007) measured secondary flows in a Weibel-type planar triple bifurcation using particle image velocimetry (PIV) along planes perpendicular to the main flow direction. Besides the need of matching the refractive index of working fluid (in their case, water glycerol mixture) and model material (elastomer), the strong out-of-plane velocity component makes this type of measurements very challenging. Their study was limited to relatively low Reynolds numbers (Re = 6 - 350), and the authors measured secondary velocities smaller than 20% of the axial velocity. According to the authors, the secondary flow strength did increase with Reynolds number (up to about Re = 100), but so did the development length of the streamwise vortices; therefore, the limited branch length ($L_i/D_i = 3.5$) prevented the further growth of streamwise vorticity at higher Re. Perhaps the most important conclusion of their study was that the secondary flows were dictated by the local geometry and not by the upstream flow history so that the same pattern of Dean vortices repeated itself through successive generations. Numerical simulations have provided much insight into features that could hardly be captured by point-wise and planar measurement techniques. Comer et al. (2001) investigated a Weibel-type planar double bifurcation model at Re = 500 and 2000. Unlike Fresconi and Prasad (2007) they found that the upstream features strongly influenced the flow pattern in the subsequent generation. The authors used a solver that did not account for unsteadiness or turbulence. In fact, early experiments reviewed by Pedley (1977) as well as more recent PIV measurements of Theunissen and Riethmuller (2007) suggested unsteadiness and transition to turbulence already for Reynolds below 1000 in bifurcating tubes. Liu et

al. (2002) also used a laminar steady solver to investigate a Weibel-type planar double bifurcation in the range Re = 2001600. The authors did not notice significant changes in flow pattern over this range and, unlike Comer et al. (2001), found that vortical flows at the second bifurcation always followed the Dean mechanism according to the local curvature. They noticed; however, how the symmetry was broken by the flow inertia for increasing Re, causing the medial branches (better aligned with the high velocity core of the previous generation) to receive higher flow rates than the lateral branches in the second generation. Mauroy et al. (2003) also studied Weibel-type double bifurcations using a laminar Navier Stokes solver in the range Re = 1001200 but reported much lower flow asymmetry compared to Liu et al. (2002): For a planar bifurcation at Re = 1200, Mauroy et al. (2003) found that the medial branches received about 30% higher flow rate than the lateral branches versus an almost 80% increase found by Liu et al. (2002). It should be noted that the geometries did not match exactly: θ was 90° in the former study and 70° in the latter. All the numerical investigation mentioned above imposed a uniform pressure boundary condition at the outlet. From this limited review of the literature, it is clear that the flow in successive bifurcations poses significant challenges to both experimentalists and modelers. The ranges of geometrical parameters and regimes relevant to respiration make the flow hard to observe and/or model satisfactorily.

As for steady exhalation, there has not been as much effort to study the mechanisms happening in this regime, and how the structure-function relationship changes over the wide range of physiologically relevant Reynolds numbers. Therefore, several questions remain open, including: Is the velocity field predominantly influenced by the local geometry or by the upstream flow? How much does the flow partitioning vary with Reynolds number? How does transition to turbulence modify the field? How does the relative importance of the different transport mechanisms vary with flow regime? Addressing such questions in simple representations of the human airways is critical to gain a predictive understanding of the airflow in the real respiratory system.

In this chapter, we investigate the three-dimensional flow in a symmetric planar double bifurcation over a wide range of physiologically relevant Reynolds numbers, from laminar to turbulent regime, during steady inhalation and steady exhalation. Time-averaged three-dimensional velocity fields are obtained using magnetic resonance velocimetry (MRV), allowing a more comprehensive characterization of the flow topology

with respect to previous experiments. We analyze the detailed distributions of velocity and vorticity, along with flow descriptors that characterize the longitudinal and lateral dispersion.

2.2 Methodology

The airway geometry we investigate is a planar Weibel double bifurcation model, and it replicates the model studied numerically by Comer et al. (2001). A schematic of the geometry with dimensions is given in **Fig. 2.1**, along with a 3D rendering. Defining the generation length L_1 from the intersection of the airway axes (**Fig. 2.1**, left), the length-to-diameter ratio at G_1 is $L_1/D_1 = 3.5$. The branching angle is $\theta = 60°$, and the normalized radii of curvature are $r_1/(D_1/2) = 6$ and $r_2/(D_2/2) = 10.3$. Similar (when not identical) geometries have been used in several previous experimental and numerical studies (Zhang and Kleinstreuer 2002; Longest and Vinchurkar 2007; Fresconi and Prasad 2007, among others). This specific model was chosen because of the full description of the geometry and velocity fields reported by Comer et al. (2001). Their study suggests that fine details as the rounding radius at the carina have a moderate effect as compared to more macroscopic features such as the bifurcation angle. We label the three branching generations G_0 (mother branch, receiving the inflow), G_1 (daughter branches, after the first bifurcation), and G_2 (granddaughter branches, after the second bifurcation). We denote the medial and lateral granddaughter branches with G_{2M} and G_{2L}, respectively. Typical airway labeling schemes use G_0 for the trachea, G_1 for the main bronchi, etc., but here we do not strictly associate the mother branch with the trachea. Rather, assuming a quasi-homothetic airway model, this geometry may represent a different location in the airway tree depending on the Reynolds number. We consider steady inspiratory and expiratory flow rates characterized by the inflow Reynolds number defined as $\mathrm{Re} = \frac{U_0 D_0}{\nu}$, where U_0 is the bulk velocity at G_0. Inhalation measurements are taken over the range Re = 100 - 5000 and exhalation measurements over the range Re = 250 - 4000 values are listed in **Table 2.1**. This is a broader range compared to previous studies and covers regimes found within the first ~ 10 generations, which account for more than 90% of the airway resistance (Pedley et al. 1970). This range is also relevant for breathing conditions in the upper airways spanning from rest to

exertion and safely encompasses the transition between the laminar and fully turbulent regime.

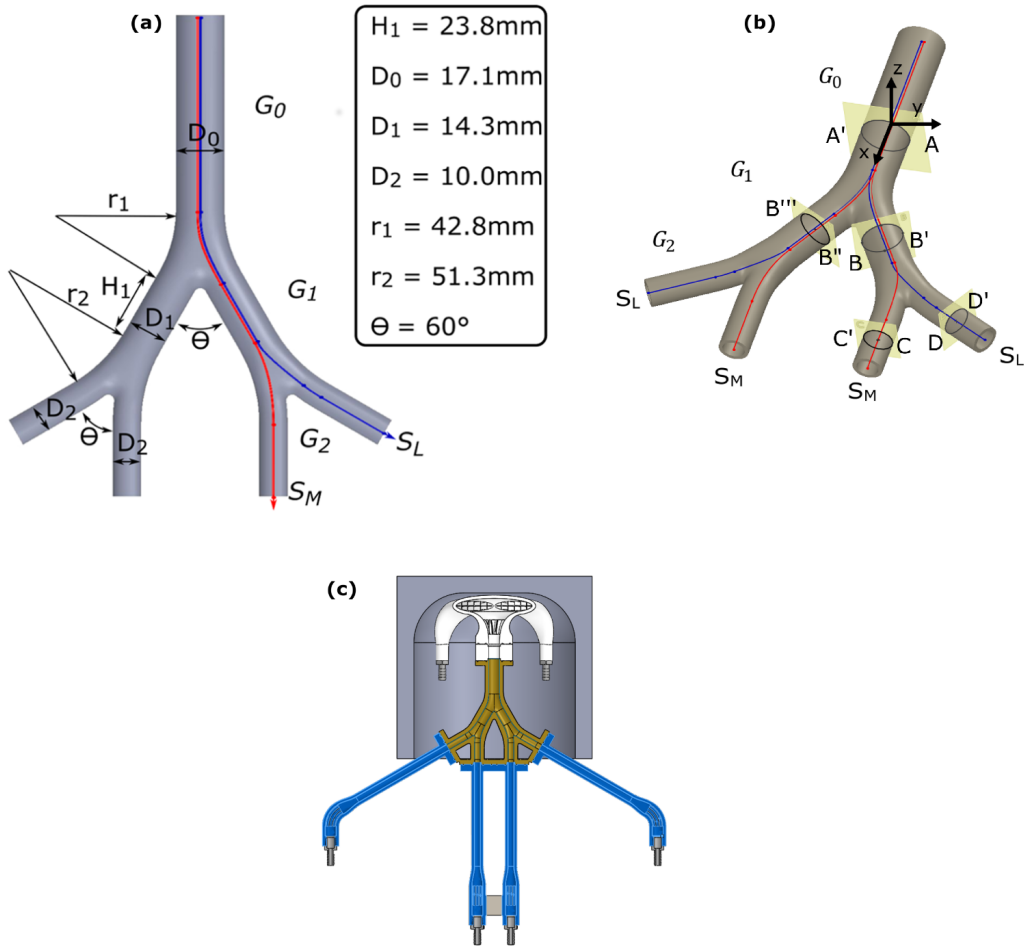

Figure 2.1: **a)** Schematic of the geometry of the double bifurcation **b)** 3D rendering of the double bifurcation. SL denotes streamwise path from G_0 to G_2 through the lateral granddaughter branch; SM denotes the path through the medial granddaughter branch **c)** CAD model of the bifurcation n model (in yellow) in the exhalation configuration, with the extension tubes connected at G_2(in blue), and the upper piece connected to G_0 (in white) fitted into the coil.

The centerline is obtained from the bifurcation volume using the software Mimics (Materialise, Belgium) and essentially coincides with the branch axes in the cylindrical

portions of the model, and with circular arcs joining successive branches in the bifurcation regions. The abscissa S is used to identify the streamwise location of various cross sections; its origin is taken at a distance $2 \times D_0$ from the first carina (the tip of the bifurcation), D0 = 17 mm being the diameter of the mother branch. At each location in the fluid domain, we define the streamwise or axial velocity Uax as the projection of the velocity vector along the direction tangent to the closest centerline curve. The transverse or secondary velocity Usec is the projection of the velocity vector along the plane normal to Uax. The bifurcation geometry is used to 3D print a model in Watershed XC 11122 with a wall thickness of about 8 mm at the W. M. Keck Center (University of Texas El Paso, TX). The high-resolution print (25-m layer thickness) guarantees that the inner walls of the model are hydrodynamically smooth. The main bifurcation piece is connected in two different ways to the rest of the flow loop, each one corresponding to one regime, inhalation or exhalation (**Fig. 2.1**). During inhalation, a 25-cm-long 3D printed pipe of circular cross section connects the inlet of the mother branch to a 1-m-long Plexiglas tube. The diameter of the 3D printed pipe varies according to a fifth order polynomial and provides a smooth transition from the diameter of the Plexiglas tube (20 mm) to that of the model inlet (D0 = 17 mm). The outlets of the granddaughter branches are connected to a 3D printed plenum much larger than their diameter (30 mm as minimum dimension).

Re	Regime	Venc [m/s]	SNR	Number of scans,N	$\frac{\delta_u}{u_0}\%$
100	Inhalation	0.12	33.5	20	5.29
250	Inhalation	0.13	41.8	20	4.45
500	Inhalation	0.12	39.6	16	4.75
1000	Inhalation	0.12	46.6	16	2.04
2000	Inhalation	0.30	35.4	16	3.30
3000	Inhalation	0.30	36.4	16	2.20
4000	Inhalation	0.50	32.1	16	3.38
5000	Inhalation	0.55	39.5	16	2.28
250	Exhalation	0.12	154.9	20	2.5
1000	Exhalation	0.25	187.6	14	2.1
2000	Exhalation	0.50	130.6	16	2.7
4000	Exhalation	0.50	70.3	16	2.6

Table 2.1: Velocity encoding, SNR, absolute velocity uncertainty, bulk inflow velocity, and relative uncertainty for all measured Reynolds numbers

In exhalation, as seen in a longitudinal cut of the assembly in **Figure 2.1 (b)**, the main bifurcation piece is connected to four extension tubes at G_2 branches with an upper piece connected to the G_0 branch. This design is dictated by the need of lodging the bifurcation inside the helmet-shaped coil used for the MRV measurements, while providing some developmental length to the granddaughter branches during the exhalation regime. The upper piece attached to the mother branch connects it to the tubing through a lofted honeycomb, limiting unwanted secondary flows that would be caused by the strong bending during the inhalation phase. The arrangement is effective in that the secondary velocity component Usec at the entrance of G_0 is measured to be less than 0.03Uax. The sudden contraction results in a plug-like inflow, as shown by the streamwise velocity profiles at G_0 close to the peak inhalation phase [Fig. 2.1 (c)]. The G_2 extension tubes also have honeycombs at the bending and are about 16d2 long (D2 being the diameter of the G_2branch), providing developed inlet flow during exhalation. The parts are hermetically flanged together and connected via plastic tubing to the pumping system. For Re = 1000 - 5000, the flow is driven by a centrifugal pump (TE-6-MD-SC, Little Giant) that circulates the fluid from a reservoir through the test section and back to the reservoir (Fig. 2.2) which are connected via plastic tubing 2.5

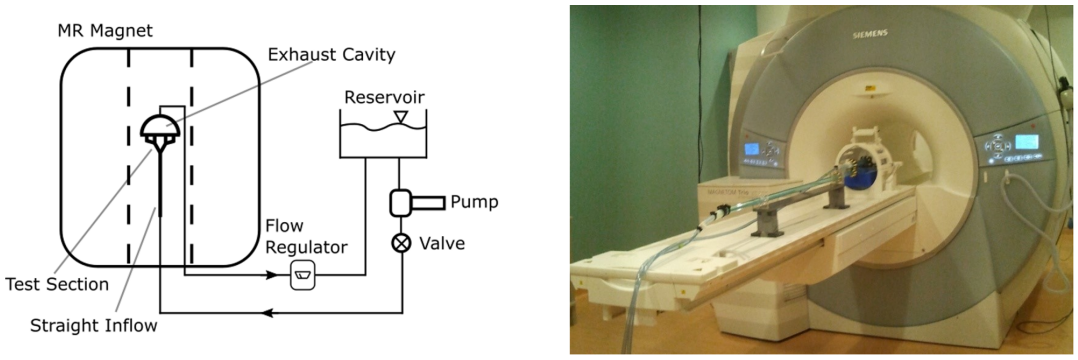

Figure 2.2: **a)** schematic of experimental setup **b)** 3 Tesla Siemens whole-body scanner with test section placed on the patient table

cm in diameter. The volume flow rate is regulated by a digital flow controller (LCR-5LPM-D, Alicat Scientific Inc.) with approximately 2 % accuracy as verified by separate calibration.

At low Reynolds numbers (Re = 100 - 500), in order to avoid flow rate oscillations from the centrifugal pump, a custom-made piston pump is used. This consists of an aluminum piston 60 mm in diameter driven by a stepper motor and controller (VXM controller, PK266 motor, Velmex) and sliding inside a Plexiglas cylinder. The fluid temperature in the reservoir is continuously monitored with a digital thermometer. To regulate temperature and compensate for heating due to the pump work, bags of ice are periodically immersed in the fluid, and the temperature is kept at 21 ± 0.5°C. For safety purposes, the pumping devices, the reservoir, the flow controller, and all magnetic components of the flow loop are located in a separate room adjacent to the magnet room. The tubing through which the fluid circulates passes through waveguides in the wall separating both rooms.

In the inhalation case, MRV measurements confirm that the velocity in the plenum is at least an order of magnitude smaller than in the branches so that the outflow boundary condition approximates that of a uniform pressure. During exhalation, four independent valves at the far end of the tubing are adjusted to maintain an equal flow rate through each granddaughter branch, as verified by a ME-6PXLTransonic clamp-on flow meter with 10% accuracy. This choice of boundary condition in the exhalation case is aimed at simplifying the analysis, as opposed to a nonuniform flow rate distribution

among the distal branches, which would be inherently arbitrary. We remark that imposing a uniform pressure here would also result in approximately equal flow rates in all granddaughter branches in steady exhalation at the lowest Reynolds number (for which the local geometry dictates the flow resistance); but this may not be the case at higher Re or in the oscillatory cases. The effect of different boundary conditions is outside the scope of the present study, but it is likely that the medial branches would offer less resistance (and carry more flow) (Jalal 2016). For Reynolds numbers between 500 and 5000, the working fluid is water, while for Re = 100 - 250, a mixture of water and glycerin (23 % in volume) is used. The latter has a kinematic viscosity of 2 106 m2/s, determined through empirical tables (Glycerine Producers Association 1963). The kinematic viscosity is tuned and verified by measuring the index of refraction of the mixture at 21 $\pm$0.5°C and using the same empirical tables to compare the measured glycerin volume percentage to the target value. The viscosity of the waterglycerin mixture allows the bulk flow velocity to remain above $\sim$ 3 cm/s. This is required to achieve a signal-to-noise ratio (SNR) high enough for accurate MRV measurements, as well as keeping the velocity well above the noise floor for the low Re cases. In all measurements, the fluid is doped with 0.06 mol/L of CuSO4, which greatly increases the SNR without appreciably altering the fluid properties.

2.3 MRV Measurements

Measurements are taken using a 3 Tesla Siemens whole-body scanner for Magnetic Resonance Imaging (MRI) at the University of Minnesota Center for Magnetic Resonance Research (CMRR). The test section and inflow are laid and secured on the patient table, with the bifurcation model inserted in a transmit-and-receive radio-frequency coil commonly used for human head imaging. Velocity data are obtained using the method described by Elkins and Alley (2007), with the signaling and data acquisition sequence from Markl et al. (2012). Three-dimensional, three-component (3D-3C) velocities are obtained on a uniform Cartesian grid at a resolution of 0.6 mm. The field of view is 153.6 by 307.2 by 26.4 mm3 and includes both the fluid and the solid walls of the test section. The velocity fields are masked to the double bifurcations wetted area by thresholding the magnitude signal above that of the background noise distribution and

masking out the exhaust cavity downstream of the double bifurcation. The acquisition process for each scan (i.e., each measurement of the 3D field) lasts several minutes, and therefore the velocities acquired are time-averaged, as described in several previous publications including Banko et al. (2015), who studied the steady inspiratory flow in a subject-specific airway model. For each experiment, the velocity encoding values (Venc), which control the maximum measurable velocity and determine the dynamic range of the acquired velocity fields, must be prescribed in each spatial direction. Because of the highly three-dimensional nature of the flow in the bifurcation, the same Venc is defined in all three directions. The values vary for the different Re cases and are verified to be at least 25 % larger than the maximum component measured in each field. The expected uncertainty in the MRV measurements is calculated as (Pelc et al. 1994):

$$\delta_U = \frac{\sqrt{2} \times Venc}{\pi \times SNR}$$

where the signal-to-noise ratio (SNR) is given by the ratio of the average signal in the fluid over the standard deviation of the signal in the background. To increase the SNR, scans are repeated N times for each condition, which provides a factor $\sqrt{N}$ improvement (Haacke et al. 1999). To correct for velocity bias and artifacts in measurements (that might arise from inhomogeneities in the magnetic field, temperature drifts, and eddy currents), we follow a variation of the procedure outlined by Benson et al. (2011) and Coletti et al. (2013): flow-off scans are performed with the same MRI acquisition parameters as the actual measurements but at zero flow rate (quiescent conditions).

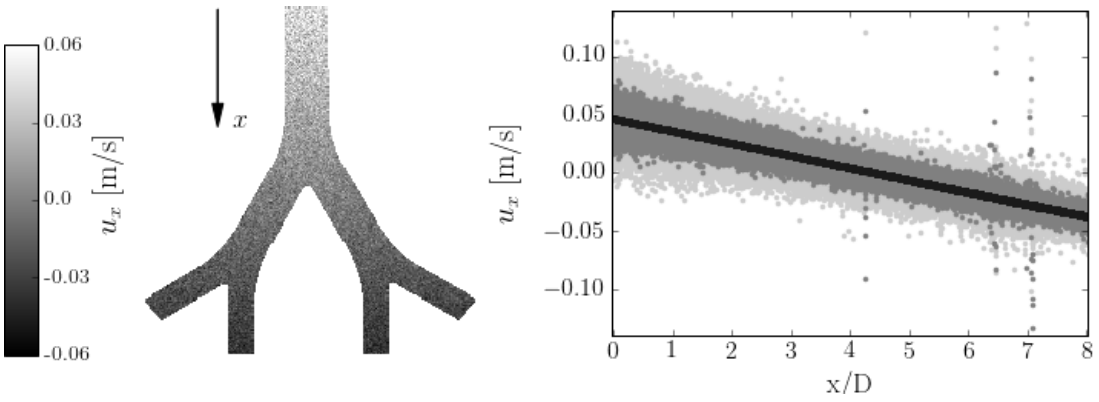

Figure 2.3: **a)** Contours of axial velocity, u_x, measured during a flow-off scan at Re = 2000 in the xy plane of the bifurcation (for which typical flow-on velocities are of order 0.2 m/s); **b)** Scatter plot of flowoff velocities for all voxels in the fluid domain as a function of axial distance, x (normalized by the mother airway diameter, D). Light gray denotes velocities measured in a single flow-off, dark gray denotes average of four flow-offs, and black denotes the analytical fit of u_x in the axial direction showing the linear bias in velocity along the axis of the model

An example of the measured flow-off is shown in the velocity contours of **Fig. 2.3** (left) for one component of velocity ux (oriented with the axial direction, x) in the xy plane. The field is composed of both velocity bias (a linear variation of ux as a function of x in the figure) and random noise associated with the experimental parameters. Multiple flow-off scans are averaged to reduce the random noise, after which a third order polynomial vector field is fitted in a least-squares sense to the measured data to model the bias. This is shown in **Fig. 2.3** (right), which is a scatter plot of ux at all fluid voxels ordered along the coordinate x. The plot illustrates both the decrease in random noise error with successive flow-off scans, and the analytical fit that captures the spatial variation of the bias error. The bias errors in the three velocity components are treated independently and corrected for in each experimental measurement. The analytically fitted bias vector field is then subtracted from flow-on scans in which the flow rate is set at the test point. Such a procedure results in significantly less error compared to subtracting the raw flow-off field, which is inherently noisy. At each Reynolds number, we typically perform one flow-off for every four flow-on scans. The flow-off scans are also used to verify whether any temporal drift has occurred during the acquisition, in which case flow-off fields are fitted to independent flow-off scans. **Table 2.1** summarizes the

uncertainty, and the contributing parameters for each considered Reynolds number. The velocity uncertainty, V, varies between 2 and 5 % of the bulk velocity. Uncertainty may be higher in the near-wall region due to the partial-volume effect (voxels being partially immersed in the solid wall). However, because the model geometry is known, such voxels are easily identified and are not included in the quantitative analysis presented in this paper. In **Fig. 2.4**, we plot the measured-to-nominal mass flow ratio for the different generations and Reynolds numbers in inhalation and exhalation. The measured mass flow rate is obtained by integrating the streamwise velocity over transverse cross sections at the different generations. In all cases, the total measured mass flow rate at G_0 is within 5 % of the nominal mass flow rate imposed by the pumping system. The higher discrepancies in G_1 and G_2reflect the fact that cross sections of further generations have a larger perimeter-to-area ratio, exacerbating the partial-volume effect.

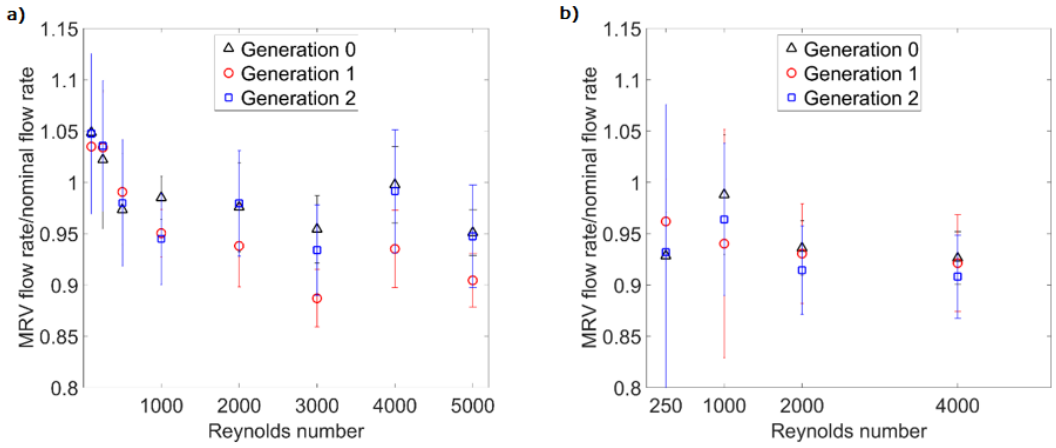

Figure 2.4: Measured-to-nominal mass flow ratio for all generations and Reynolds numbers at **a)** inhalation **b)** exhalation

2.4 Streamwise velocity distribution

2.4.1 Steady inhalation

We begin the flow analysis by considering the distribution of the streamwise velocity, responsible for the advective transport. **Figure 2.5** shows color contours of streamwise velocity along the xy plane containing the bifurcation centerline. Selected Re cases are

shown to highlight the general trend. The velocity in G_0 follows the expected profile for fully developed pipe flow, and therefore it becomes more uniform across its cross section for increasing Reynolds numbers. Downstream of the first carina, the flow inertia causes the high-momentum fluid to favor the internal side of the bifurcation for all cases. This leads to a strong velocity deficit at the external side of the G_1 branch, although no significant mean flow reversal is present. This effect is more pronounced for increasing Reynolds numbers up to Re = 2000, reflecting the increasing importance of inertial forces.

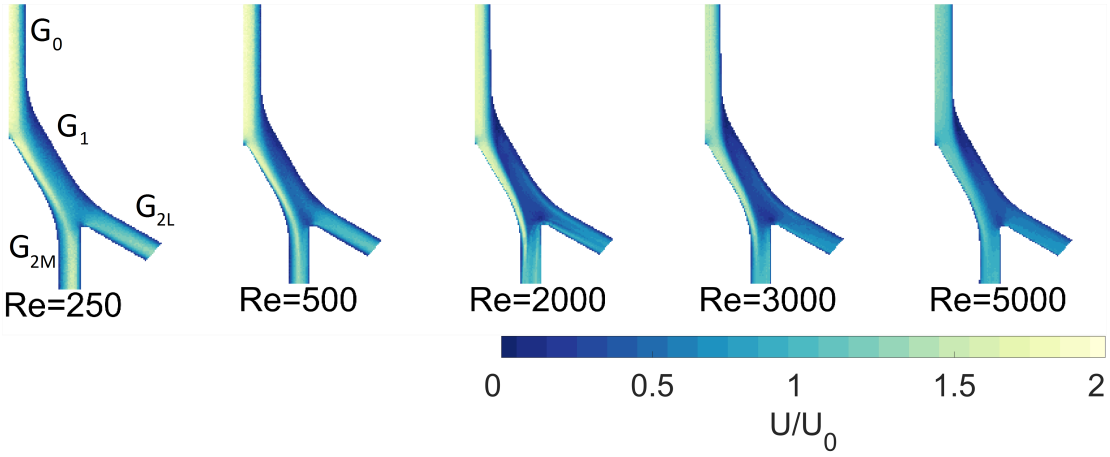

Figure 2.5: Contours of magnitude of velocity (flowing from top to bottom) in the xy plane covering the range Re = 250-5000. Only half the x-y symmetry plane is shown

For higher flow rates, the mean velocity gradients are generally smoother and the velocity distributions even out. This is largely caused by turbulent transport, as the fully developed pipe flow feeding the mother branch is turbulent for the cases Re = 3000-5000 (Pope 2000). The secondary flows also contribute to spread the high-momentum region over the cross section of each branch. However, as it will be shown later, the mean transverse velocities become weaker for Re > 2000, and therefore they are unlikely to be the main mechanism responsible for the homogenization of the streamwise velocity at these regimes. The contours in **Fig. 2.5** show that, at all Re, the flow partitioning in the xy plane at the second bifurcation favors the medial branches, which are aligned with their grandparent branch G_0. This behavior was already shown by Andrade et al. (1998) using 2D simulations and is dependent on the Reynolds number. Following

Liu et al. (2002), we quantify the asymmetry in the flow partition using the ratio $\bar{m}$ between the mass flow rate through G_{2M} and G_{2L}:

$$\bar{m} = \frac{m_M}{m_L}$$

This is plotted in **Fig. 2.6** for different Reynolds numbers, with the error bars reflecting the uncertainty on the mass flow rates discussed earlier. The power-law fit obtained by Liu et al. (2002) is also shown for comparison. In the present measurements, the flow asymmetry increases sharply up to Re = 1000 and then reaches a plateau. This suggests that, while the inertia forces cause flow asymmetry, the transition to unsteady/turbulent behavior (expected for Re = O(10^3)) favors a more homogeneous distribution of momentum among the daughter branches. We note that the local Reynolds number at $G_2$is about three times smaller than in G_0, so the equivalent pipe flow would be expected to be fully laminar.

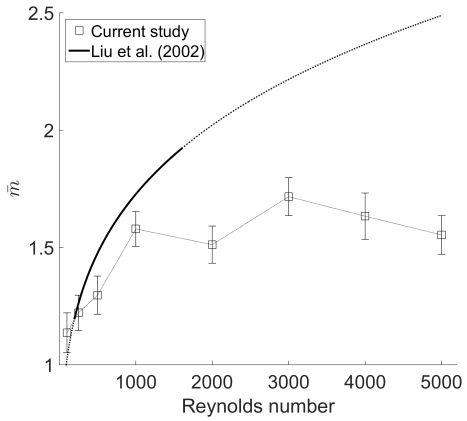

Figure 2.6: Ratio of medial-to-lateral flow rate in G2,$\bar{m}$, as a function of the Reynolds numbers. The solid line denotes the power law (fitted to simulations) by Liu et al. (2002), and the dashed line denotes extrapolation of the curve beyond their investigated regime (Re = 200 - 1600)

The perturbations, however, propagate downstream through the relatively short branches and are likely fed to the successive bifurcations. The calculations of Liu et al. (2002) show a similar trend for Re < 500, but for higher regimes, they indicate a much more asymmetric behavior compared to the present measurements. Their simulations

imposed steady laminar flow up to Re = 1600, whereas it is possible that unsteadiness starts to play a role already at this regime, due to the geometry expansion, the curvature, and the impingement on the carina. If the trend found by Liu et al. (2002) is extrapolated to higher Reynolds numbers, the predicted flow partitioning distribution greatly diverges from our measured mass flow rate ratio. Because the flow is highly three dimensional, its visualization is eased by the 3D-3C nature of the present velocimetry technique.

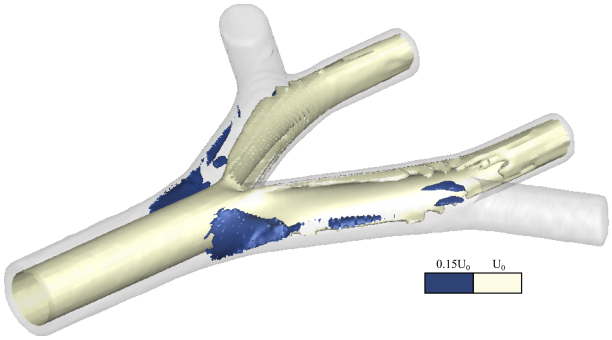

Figure 2.7: Isosurfaces of low (dark) and high (light) streamwise velocity in the double bifurcation at Re = 2000

Figure 7 shows a representative case of the velocity field in the bifurcation, using iso-surfaces of high (U = U_0) and low (U = $0.15U_0$) streamwise velocity for the case Re = 2000. The core flow from the mother branch impinges on the first carina and forms high-momentum regions that stretch along the inner side of the bifurcation for about half of the airway circumference. Beyond the second bifurcation, the fast fluid is then channeled predominantly through the medial branches. The slow velocity pockets, caused by the increase in cross section, are confined to the flanks of the first bifurcation. In order to quantify the degree of streamwise velocity variation in each cross section, we calculate the momentum distortion parameter, D (Padilla 2012) used also in the subject-specific airway flow study of Banko et al. (2015). This is defined as:

$$D = \frac{\int_A (U_{ax})^2 dA}{Q^2 A} - 1$$

where A is the cross-sectional area and Q is the local volumetric flow rate. The D parameter represents the relative difference between the streamwise momentum flux of

the actual flow and that of a plug flow carrying the same mass flow rate. For context, fully developed laminar (parabolic) and turbulent (1/7th power law) pipe flows have values D = 1/3 and D = 0.02, respectively. The D parameter is a measure of longitudinal dispersion due to the mean flow, being associated to the amount of axial strain experienced by the fluid at each cross section.

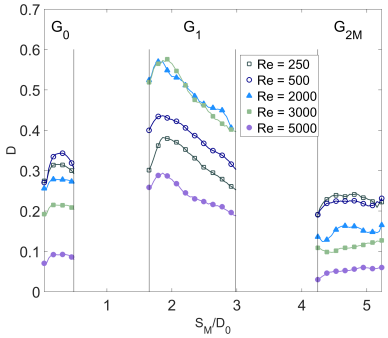

Figure 2.8: Momentum distortion parameter along the medial path for selected Reynolds numbers

Figure 2.8 plots the D parameter as a function of the streamwise abscissa SM for different Reynolds numbers. Trends along S_L are sufficiently similar to be omitted here for brevity. We discuss only the results within the branches, as in the carinal regions the appropriate cross-sectional area is not trivial to define. In this and successive line plots in this section, only a subset of all investigated Re cases is shown, so as to illustrate the trend without cluttering the figure. Levels of the D parameter close to the theoretical value of 0.33 are found in G_0 for the laminar cases, while lower values are found for the transitional and turbulent cases, as expected. The G_1 branch displays much higher D values at the entrance of the branch, due to the strong gradient in velocity profile across the branch diameter of the first bifurcation (see **Figure 2.5**). The D parameter decreases significantly along the branch, due to viscous effects dampening the strong velocity gradients and secondary flows spreading the axial momentum in the transverse plane. In G_1, the values of D increase with Reynolds number up to Re = 20003000 and then markedly decrease. This can be interpreted as a consequence of the turbulence transport enhancing the transverse momentum transfer and diffusing the mean velocity gradients. The effect of turbulence fluxes on the mean flow attenuates mean longitudinal

dispersion and leads to the progressive decrease in D up to the highest considered regime of Re = 5000. G_2 shows much lower D values, indicating that the streamwise velocity is more uniform across the cross sections in the branch. We remark that the D values in the daughter and granddaughter branches (D = 0.1 - 0.5) are consistent with those found by Banko et al. (2015) in a realistic airway model based on the CT scan of a human subject.

2.4.2 Steady exhalation

Like the analysis above, we first focus on the streamwise velocity fields responsible for the bulk advective transport during steady exhalation. **Figure 2.9** shows contours of the velocity magnitude along the plane of the x-y bifurcation for the cases Re =250 and 2000, the latter displaying qualitatively similar behavior as Re =1000 and 4000. The flow streams from G_2towards G_0, merging after each junction. As the streams from G_{2L} and G_{2M} merge, a high-momentum region is created at the center of G_1, flanked by low-momentum regions near the wall. At Re =250 the velocity gradients in G_1 are relatively mild, while at Re =2000 the high momentum of both streams leads to a jet-like merging with sharp jumps in velocity magnitude. This is also illustrated by B-Bsection, which shows that the high-velocity region extends across the entire branch in the direction normal to the bifurcation plane. Secondary velocity vectors are also displayed, highlighting streamwise vortices whose structure and propagation will be addressed later in this chapter.

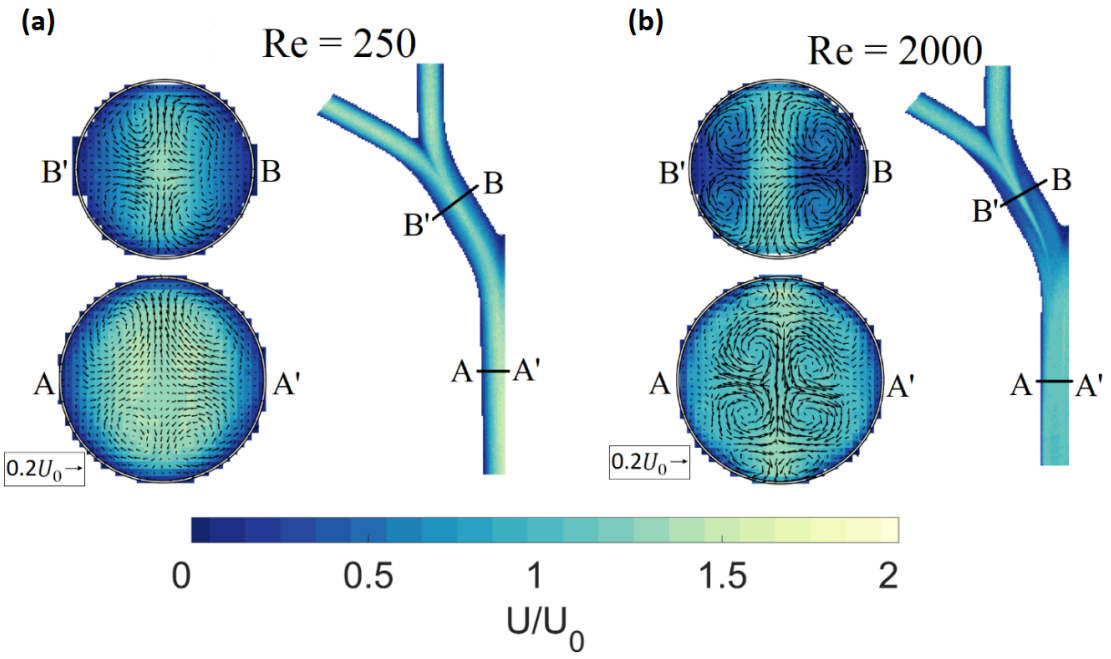

Figure 2.9: Contours of velocity magnitude along the bifurcation plane and streamwise velocity along cross sections A-A' and B-B', for steady exhalation at Re = 250 **a)** and Re = 2000 **b)**. Secondary flow vectors are shown in the cross sections. A reference velocity vector is shown at the bottom left.

Figure 2.10 shows the streamwise velocity profiles along the bifurcation plane in G_1 and G_0 (stations B-B' and A-A', respectively). At G_1 [**Fig. 2.10(a)**] the profile for Re =250 is fairly symmetric around the branch centerline, reflecting the symmetry of the local geometry, and the increase in velocity from the wall to the center of the branch is gradual. For higher Re, as mentioned above, the fast-central region contrasts with the slower fluid near the walls, a feature also noted by Lieber and Zhao in their classic single bifurcation study. However, the mutual impact of the successive bifurcations is evident in the asymmetry of the profiles at B-B' for Re =2000 and Re =4000, which are influenced by the downstream turn at the G_1-G_0 junction. At G_0 [**Fig. 2.10(b)**] the velocity profile for Re =250 displays two peaks, resulting from the merging of the two pointy profiles from the daughter branches. For Re 1000, the distribution flattens due to the strong secondary velocities pushing the fluid away from the center of the branch. This is in contrast with the Re =250 case, where the secondary flows have opposite

sense of rotation (as discussed below).

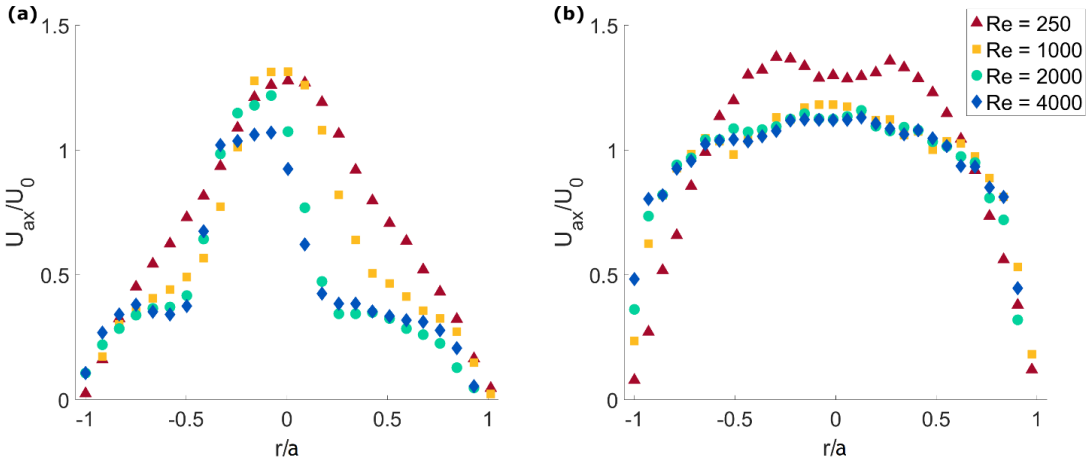

Figure 2.10: Streamwise velocity profiles under steady exhalation for all considered Reynolds numbers, at stations **a)** B-B' and **(b)** A-A'.

Turbulent or unsteady transport is also likely to play a role in blunting the profile at the higher Re, but this is not quantified here. **Figure 2.11** shows D as a function of the streamwise abscissa for the various Re, averaged between the medial and lateral paths (which were negligibly different). Here again, we report only the results within the straight branches since the streamwise components in the carinal regions are not trivial to identify univocally. At G_2, D is around the theoretical value 0.33 for the lower Re cases (supposedly laminar and fully developed), while at higher Re the profiles are flatter and D decreases accordingly. At G_1, D remains relatively high for Re =250, reflecting the pointy shape of the velocity distribution, and is almost constant throughout the branch. With increasing Re, because of strong secondary flows spreading the momentum over the cross section, D decreases and tends to drop along the branch. By G_0, the value of D for Re =4000 is close to the expected value for fully developed turbulent pipe flow. Overall, D has lower values compared to the inspiratory case for the same Reynolds numbers, indicating generally flatter profiles (Zhao and Lieber 1994).

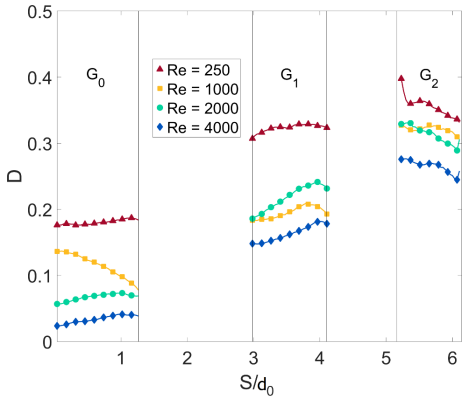

Figure 2.11: Momentum distortion parameter D under steady exhalation for all considered Reynolds numbers. The flow direction is towards smaller values of the abscissa

2.5 Secondary flows & streamwise vorticity

2.5.1 Steady inhalation

The secondary velocities at each cross section are responsible for the so-called augmented or lateral dispersion, which can induce strong mixing especially in regions of reduced streamwise velocities (Fredberg 1980). According to previous experiments in single and double bifurcations, we expect pairs of counter-rotating vortices (Zhao and Lieber 1994; Fresconi and Prasad 2007). The parameter dictating the formation and strength of this type of secondary flows is usually considered the Dean number, Dn, which represents the ratio of centrifugal forces to viscous forces and is defined here in each branch (Dean 1927; Doorly and Sherwin 2010):

$$Dn_i = Re_i \sqrt{\frac{D_i/2}{R_i}}$$

Re_i is the local Reynolds number associated to the ith generation branch with diameter D_i and velocity U_i, R_i being the radius of curvature of the airway centerline in the carinal region of the bifurcation upstream of the ith branch. In the present geometry, the bifurcation centerlines do not follow exactly circular trajectories, but are closely approximated by circular arcs with radii of curvature $R_1 = r_1 + D_1/2 = 50$ mm and $R_2 = r_2 + D_2/2 = 56.3$ mm where r_i is the radius of curvature with respect to the outer

wall of the carina (see **Fig. 2.1**). The values of both Re_i and Dn_i are reported in **Table 2.2**, accounting for the measured asymmetry in flow partitioning and (therefore in Reynolds number). For all branches, Dn_i is well above the critical value of 10 for which counter-rotating Dean vortices were observed by Fresconi and Prasad (2007), suggesting that Dean vortices should be found in all branches and stronger ones in the proximal generations.

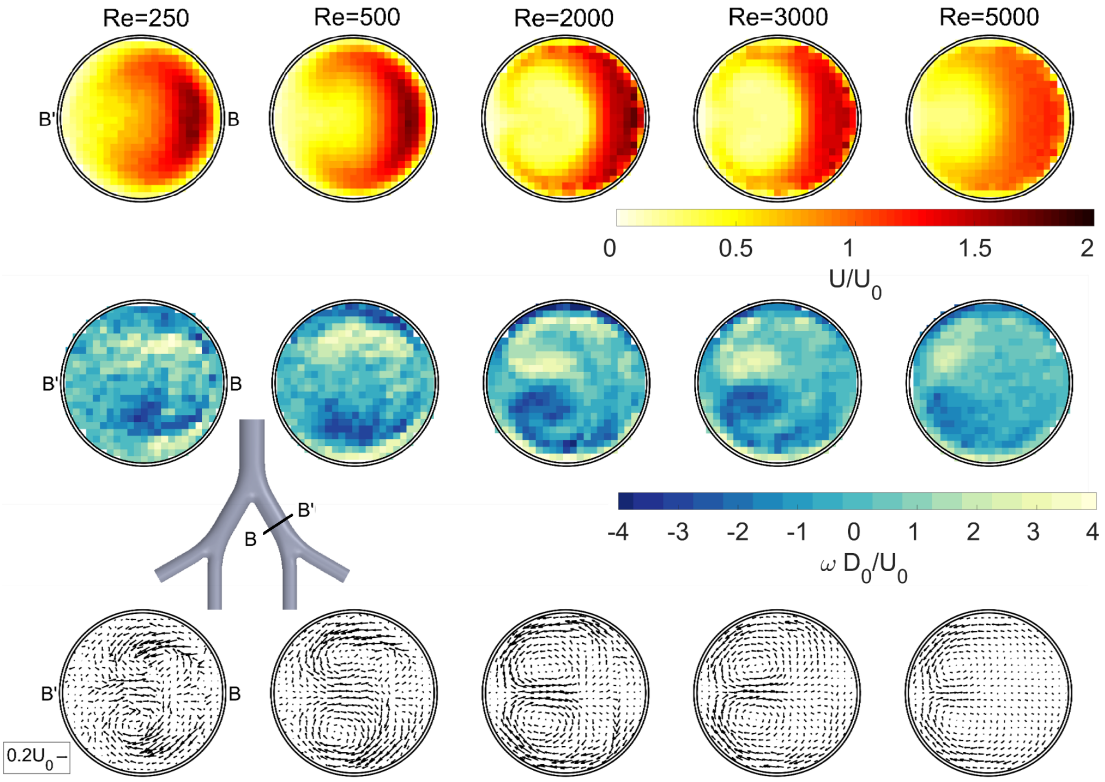

Figure 2.12: Contours of normalized streamwise velocity (top), out-of-plane vorticity (middle), and in-plane velocity vectors (bottom) vectors at cross section BB for selected Reynolds numbers

Figure 2.12 shows vectors of in-plane velocity superimposed to contours of streamwise vorticity ω along a cross section of the daughter branch G_1. Vorticity is calculated from a standard second-order central difference scheme for each component and then projected along the streamwise direction. For all considered Reynolds numbers, the Dean mechanism drives the formation of secondary flows in this generation: the low

momentum fluid far from the plane of the bifurcation (i.e., far from the xy symmetry plane defined in **Fig. 2.1**) experiences a transverse pressure gradient stronger than the centrifugal force and is pushed toward the center of curvature of the airway (i.e., away from the carina and toward the outer side of the bifurcation, side B in the figure). These fluid layers merge at the plane of the bifurcation and push the core fluid away from the center of curvature of the airway (i.e., toward the inner side of the bifurcation, side B in the figure). This produces a pair of counter-rotating vortices flanked by near-wall shear layers. The strength, shape, and position of the vortices change significantly with Re. As Re increases, the vortex cores move toward the outer side of the bifurcation and move toward the xy symmetry plane and closer to each other. The high vorticity cores display elongated tails that stretch along the near-wall shear layers. The streamwise vorticity increases up to Re = 2000, in which the transverse velocities can be as high as 17 % of the local bulk velocity. At higher Re, ω becomes weaker and more diffuse, again as a consequence of turbulent diffusion smoothing the mean velocity gradients.

Re_0	Re_1	Dn_1	$Re_{2,M}$	$Dn_{2,M}$	$Re_{2,L}$	$Dn_{2,L}$
100	62	25.3	47.5	14.8	42	13.1
250	153.5	62.6	121.7	38	99.4	31.0
500	291.7	118.9	236.2	73.7	187.6	58.6
1000	579.7	236.1	489	152.7	295.4	92.2
2000	1148.3	468	1012.2	316	683.4	213.4
3000	1599	651.7	1490.5	465.4	911.3	284.6
4000	1963.9	800.3	1853.4	578.7	1136.6	354.9
5000	2710.2	1104.5	2421.8	756.2	1614.6	504.2

Table 2.2: Summary of Reynolds numbers and Dean numbers in all generations

Figure 2.13 shows streamwise velocity contours as well as secondary velocity vectors overlaid to streamwise vorticity contours along cross sections of G_{2M} and G_{2L}. For Re up to 250, the medial granddaughter branch shows a qualitatively similar trend as the previous generation, with counter-rotating vortices and shear layers oriented as dictated by the Dean mechanism. This is in agreement with the PIV measurements of Fresconi and Prasad (2007). For Re = 500, however, the pattern is more complex, and an

additional vortex pair appears close the inner side of the bifurcation (side C in the figure) and pushes the Dean vortices toward the branch perimeter. A similar four-vortex pattern was found in the study of Leong et al. (2009) in a double bifurcation at Re = 280. Above Re = 500, the latter vortex pair dominates, and as a result the secondary flow pattern is characterized by two counter-rotating vortices oriented in the opposite way with respect to the classic Dean mechanism. These secondary velocities are also particularly strong, being as high as 30 % of the local bulk velocity for Re = 2000. Such change in topology is due to influence of the Dean vortices generated in G_1 and extending into G2.

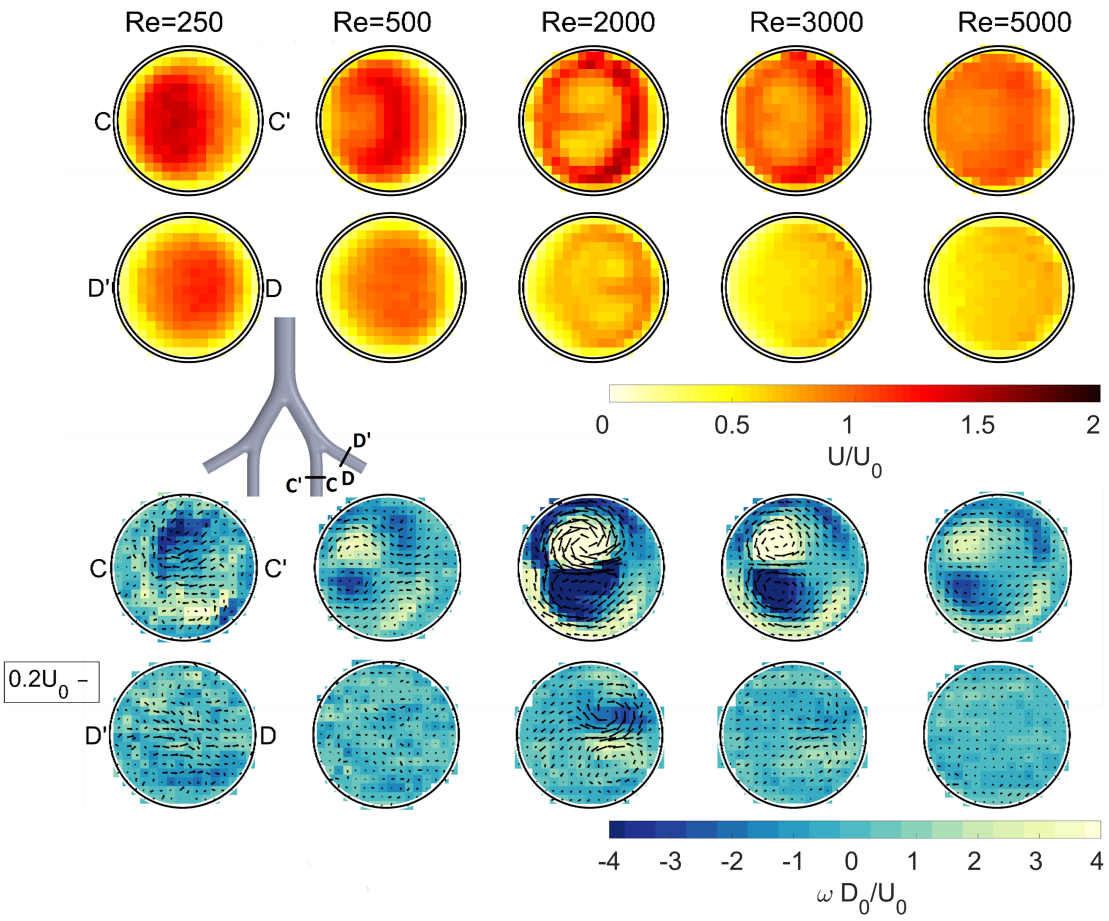

Figure 2.13: Contours of normalized streamwise velocity (top) and out-of-plane vorticity with superimposed in-plane velocity vectors (bottom) at cross section CC and DD for selected Reynolds numbers. The change in vortex sense of rotation in the medial branch occurs from Re = 250 to 500

The vortices in G_1 are indeed increasingly strong with higher Reynolds number and persist beyond the second bifurcation. Their position and the asymmetric partitioning of the flow cause the vortices in G_1 to be preferentially directed into G_{2M}. This is illustrated in **Fig. 2.14**, which shows 3D isosurfaces of Γ_2. The latter is a scalar (defined formally below in **Eq. 6**) which identifies rotation in normal planes to the streamwise abscissa and has the same sign as the local streamwise vorticity. From these volumetric fields, it is clear that for sufficiently high Re, the vortical structures found in the medial granddaughter branches are indeed the extension of the vortices in G_1. In

particular, though the Dn values would suggest Dean-like secondary flows in all branches (see **Table 2.2**), in G_{2M} these are only prevalent below Re = 500; for Re = 1000 and above, the influence of the upstream flow is dominant.

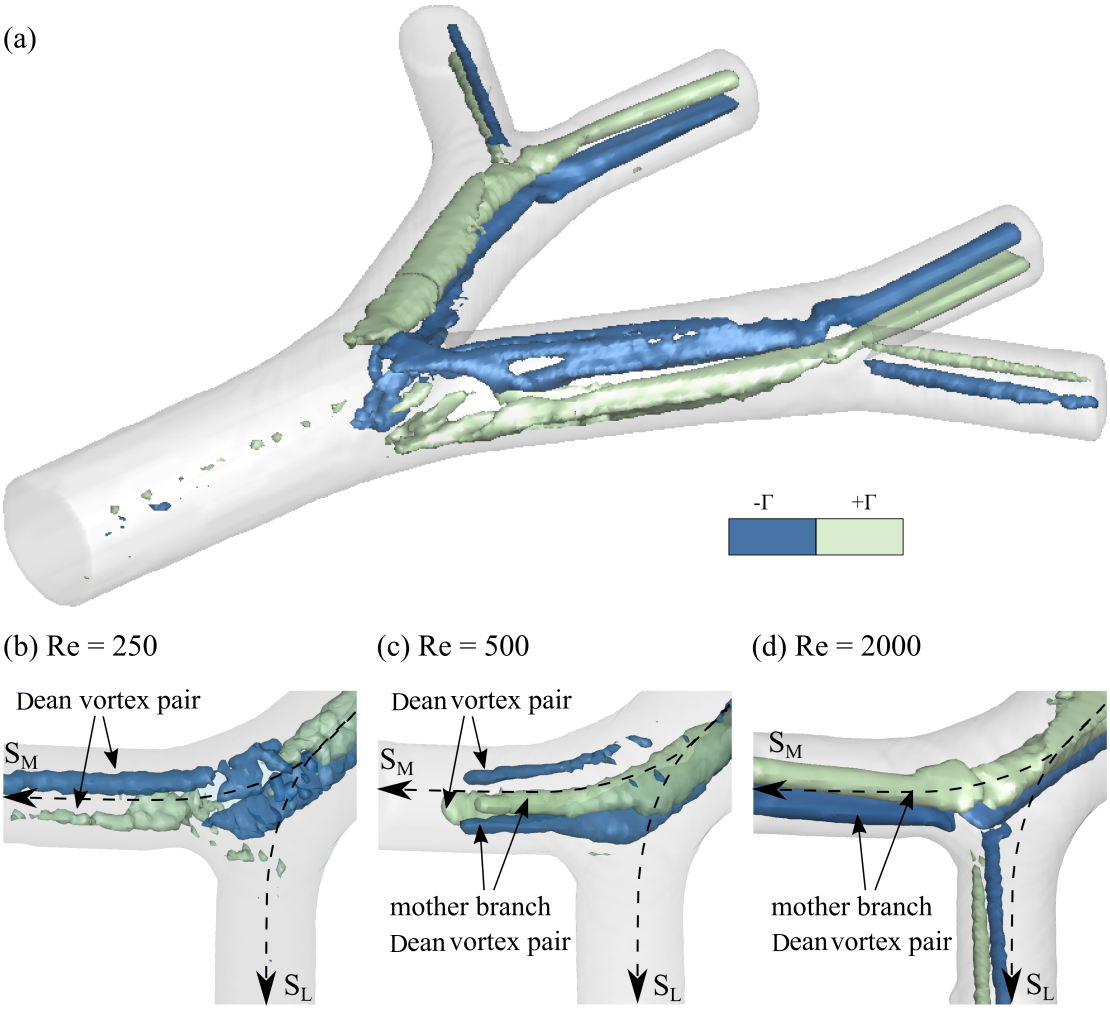

Figure 2.14: Isosurfaces of positive (green) and negative (blue) Γ_2 representing the dominant coherent structures oriented along the medial, S_M, and lateral, S_L, streamwise abscissa. Top panel a shows streamwise vorticity for Re = 2000 in the second bifurcation. After the inflow, Dean vortices develop along the daughter branch, G_1, and are then advected into the medial granddaughter branch, G_{2M}. The bottom panel shows the change in vortex topology across Re = 250, 500, and 2000, evolving as, b a Dean vortex pair forming in G_{2M} for Re = 250, or c switching to a quadruple vortex pattern that rapidly loses coherence in G_{2M} for Re = 500 as the mother (G_1) Dean vortex pair are advected into G_{2M}. Finally d only the appearance of the mother (G_1) Dean vortex pair is visible for Re = 2000

The measured flow pattern in G_{2M} for Re = 500 and 2000 is in qualitative agreement

with the numerical studies of Comer et al. (2001) at the same Re. At higher Re, the fundamental topology does not change, but the strength and size of the vortex cores are reduced, which we again attribute to turbulent diffusion. For all considered cases, the vorticity is mostly propagated from G_1 to G_{2M}, and in G_{2L} the secondary flows are far less intense (see **Fig. 2.13**). The only case that shows a coherent pair of vortices in the lateral branches is Re = 2000, with a sense of rotation opposite to a Dean vortex pair (and also visible in **Fig. 2.14 (d)**). This is the case with strongest vortices in G_1, but also with fastest fluid in the upper and lower near-wall layers, which have higher streamwise velocity than the core of the branch. This is the opposite situation with respect to a canonical pipe flow, and it causes the centrifugal forces to push the near-wall fluid toward the carina and the core fluid away from it. This produces the observed counter-rotating vortex pair in G_{2L}, which has the opposite sense of rotation with respect to the classic Dean mechanism. Because the streamwise vortices drive the lateral dispersion from the mean flow, it is of interest to investigate their evolution along the airway branches. To this end, we use the dimensionless scalars Γ_1 and Γ_2 (Graftieaux et al. 2001) to identify the vortical structures in the plane perpendicular to the streamwise velocity. The Γ_1 and Γ_2 fields are two-dimensional topological filters for the velocity field identifying regions of flow dominated by rotation. The fields are defined, respectively, as:

$$\Gamma_1(P) = \frac{1}{N}\sum_{i=1}^{N} \frac{(PM \times U_M).z}{\parallel PM \parallel . \parallel U_M \parallel} dS$$

$$\Gamma_2(P) = \frac{1}{N}\sum_{i=1}^{N} \frac{(PM \times (U_M - \tilde{U_P}).z}{\parallel PM \parallel - \parallel U_M - \tilde{U_P} \parallel} dS$$

where S is the interrogation window centered on P, N is the number of points M inside S, and z is the unit vector normal to the measurement plane. U_M is the velocity vector at point M, PM is the vector from P to M, and $\tilde{U_P} = \frac{1}{N}\sum_{i=1}^{N} U dS$ is the local convection velocity around P. The method relies on interrogating a neighborhood with an interrogation window of 2 voxels, to identify regions dominated by rotational motion. The path of the vortex core is tracked by calculating the 1 field at the end of the streamwise abscissa first, identifying the core and then tracking the vortex core

upstream. To increase the robustness of the identifier, spurious maxima in $\mid \Gamma_1 \mid$ are avoided by limiting the search in each streamwise location to a neighborhood radius of 0.9 mm (corresponding here to 1.5 times the voxel size) from the center located at the previous step. For the vortex core identification, the Galilean invariant Γ_2 field is similarly calculated, for which the criterion $\mid \Gamma_1 \mid > \frac{2}{\pi}$ defines regions of rotation dominated motion. To fully capture the characteristic kidney shape of the present vortices, the limit on the Γ_2 criterion is modified, so that $\mid \Gamma_2 \mid > 0.4 \mid \Gamma_{2max} \mid$ defines regions of rotation dominated motion, where $\mid \Gamma_{2max} \mid$ is the average of the top 5% of $\mid \Gamma_2 \mid$. Other vortex core identification techniques exist (including the one recently proposed by Bulusu et al. 2014), but the effect of using different approaches is beyond the scope of the present study.

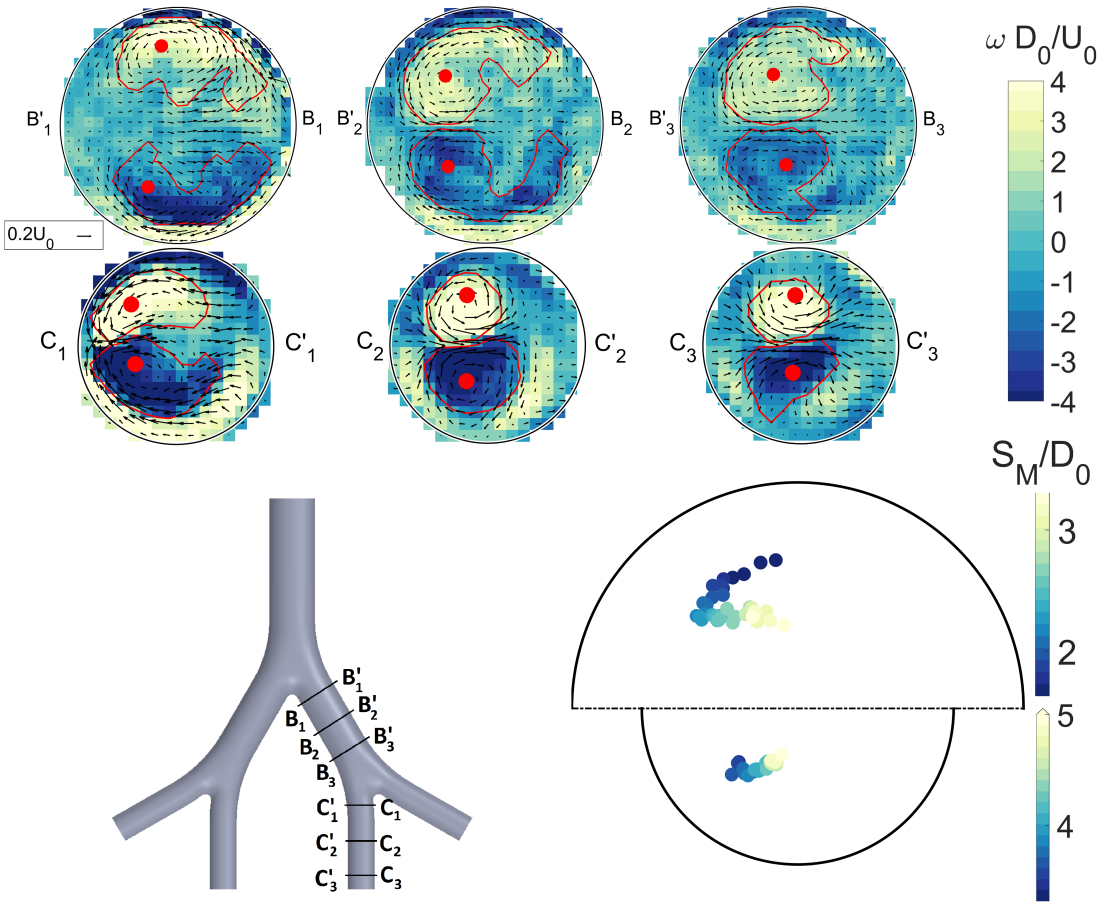

Figure 2.15: Top contours of normalized out-of-plane vorticity with superimposed in-plane velocity vectors and boundaries of vortex cores (red lines) at several cross sections in G_1 and G_{2M} for Re = 1000. Bottom location of vortex core tracked along the streamwise abscissa in branches G_1 (top half-circle) and G_{2M} (bottom half-circle) for Re = 1000. Dark to light represents progression in the streamwise direction (notice different color bars for G_1 and G_{2M})

Figure 2.15 shows the identified vortices along several cross sections in G_1 and G_{2M} for Re = 1000. The vortices in G_1 start relatively close to the airway perimeter, which causes them to interact with the nearby wall and move along it toward the outer side of the bifurcation. As they approach each other, they induce a motion that pushes them in the opposite direction, i.e. toward the center of the branch. In G_{2M} the vortices start from the side of the airway near the carina, already close enough to each

other to interact. As in G_1, the interaction causes them to travel toward the center of the cross section. Although the details of the trajectories of the vortex cores vary with Re, the features and mechanism remain qualitatively similar. The strength of the counter-rotating streamwise vortices in the airway tree is measured by evaluating their circulation along the streamwise abscissa. This is calculated as:

$$\Gamma = \int_{A_{VORT}} \omega dA$$

where A_{VORT} is the area within the detected vortex core region. The value of is computed for both counter-rotating vortices of each cross section and averaged (the difference between both values being typically a few percent). For the case Re = 500, in which a quadruplet of vortices is present in G_{2M}, the vortex pair that descends from G_1 is considered.

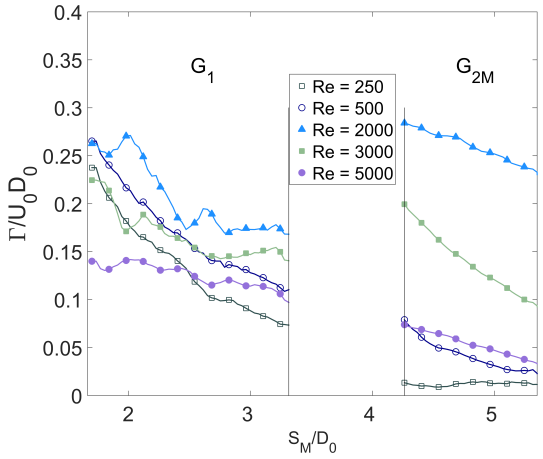

Figure 2.16: Normalized circulation $\frac{\Gamma_2}{U_0 D_0}$ along the medial path for selected Reynolds numbers

Figure 2.16 shows the normalized circulation as a function of the streamwise abscissa for different Re. As with the D parameter, the carinal region is omitted. In branch G_1, the circulation levels increase steadily with increasing Re in the range Re = 1000-2000 and drop sharply at higher Re, as one would expect from the above considerations on the effect of transition to turbulence in dissipating mean velocity gradients. In terms of streamwise evolution, the strength of the vortices declines steeply along G_1 for

Re $\leq$ 500. The decline is less sharp for higher Re, as viscosity has a smaller influence on the evolution of structures located away from the walls. In G_{2M} the circulation is lower than in G_1 for Re $\leq$ 500, while for Re = 1000 - 3000, the levels in G_{2M} are comparable or higher than in G_1. This is remarkable, as the lower local Re and Re would suggest a substantial reduction of the secondary flow strength with further generations. As noted above, however, the streamwise vortices in G_{2M} for high Re are the extension of those in G_1, rather than being Dean-type secondary flows. Their tilting and stretching into the narrower granddaughter branches concur to enhance the vorticity and compensate for the viscous dissipation. Moreover, new azimuthal vorticity is injected in the flow at the second carina and can be partially reoriented in streamwise direction, contributing to increasing in G_{2M}. At Re $>$ 3000, the turbulent diffusivity acts as a sink for vorticity and the streamwise circulation in G_{2M} drops substantially, also declining along the length of the branch. In order to evaluate the importance of all secondary flows, and not only the counter-rotating vortex pair, we calculate the secondary flow parameter, E, which indicates the relative strength of secondary velocity components to the streamwise velocity components over each cross section (Banko et al. 2015):

$$E = \{\frac{\int_A [\vec{u} - (\vec{u}.\hat{n})\hat{n}]^2 dA}{\int_A (\vec{u}.\hat{n})^2 dA}\}^{\frac{1}{2}}$$

Regions with high values of E produce rapid lateral dispersion relative to the rate of streamwise advection. **Figure 2.17** reports the trend of the E parameter for G_1 and G_{2M} (as discussed, secondary flows are marginal in G_{2L}). The dependence with Reynolds number is in keeping with the trends for D and Γ, with an increase up to Re = 2000 followed by a sharp drop at Re $\geq$ 3000. The E parameter also appears to decline steeply along each branch. As this is not entirely due to a loss of circulation of the counter-rotating vortex pairs (see **Fig. 2.16**), this trend is likely caused by the near-wall shear layers being dissipated by viscosity along the airway walls. For comparison, the E values reported by Banko et al. (2015) in their CT-based airway model ranged between 0.07 and 0.23, while the present levels do not exceed 0.07. This suggests that real airway features (such as large bifurcation angles and consequent flow separation, as well as non-planar curvature) can drastically increase the strength of the secondary motions and therefore the augmented dispersion as compared to idealized

representations.

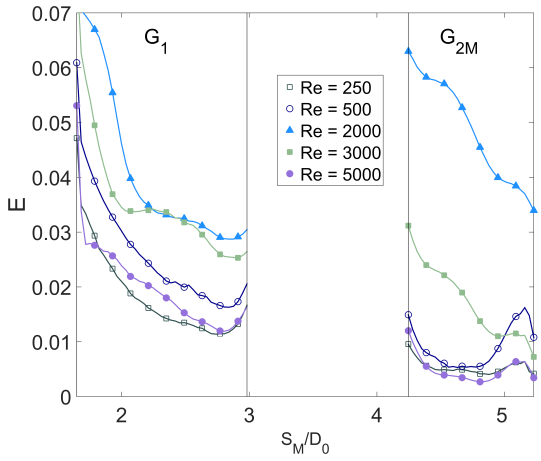

Figure 2.17: Secondary flow parameter along the medial path for Re = 250, Re = 500, Re = 2000, Re = 3000, and Re = 5000

2.5.2 Steady exhalation

Similar to our analysis in the previous subsection, we start our investigation by exploring the streamwise momentum distribution cross sections shown in **Fig. 2.9.**, which indicate the presence of coherent secondary flow structures. In G_1, similar to the inhalation regime, these are locally generated by the Dean mechanism. This creates two counter-rotating streamwise vortices from each grand-daughter branch (lateral and medial), resulting in a system of four vortices. While the flow topology in G_1 is similar for all cases, significant differences are evident at G_0 depending on Re. To localize the streamwise vortices we again use the vortex identifier Γ_2.

In **Figure 2.18**, we contrast the cases Re =250 and 2000, which exemplifies the Reynolds number effects on the secondary flow patterns. Iso-surfaces of 2 = 0.6 are shown (comparable to the level of 2/ adopted by Graftieaux et al., 2001), as well as cross-sectional contour plots. For clarity, we show only iso-surfaces over the regions highlighted in the cross sections. For both Re, we identify the four counter-rotating vortices in G_1 (labeled 1 through 4 at station B-Band 5 through 8 at B-B). At Re =250 these dissipate before the G_1-G_0 junction, where the Dean mechanism leads to the formation of a similar system of four counter-rotating vortices (labeled A through

D) that propagate through the mother branch. At Re =2000, on the other hand, the vortices formed in G_1 are strong enough to survive into G_0. In particular, vortices 1-2 and 7-8 gain strength thanks to mutual interaction and form a quadruplet of intense counter-rotating vortices visible in the core of G_0. This system of eight vortices is bordered on the upper and lower side by four newly formed structures (labeled E through H). These appear to be generated by the interaction of the four core vortices (1-2-7-8) with the fluid layer between them and the upper or lower side of the branch perimeter. In order to quantify the strength of the vortical structures, we evaluate their circulation and its evolution along the streamwise abscissa.

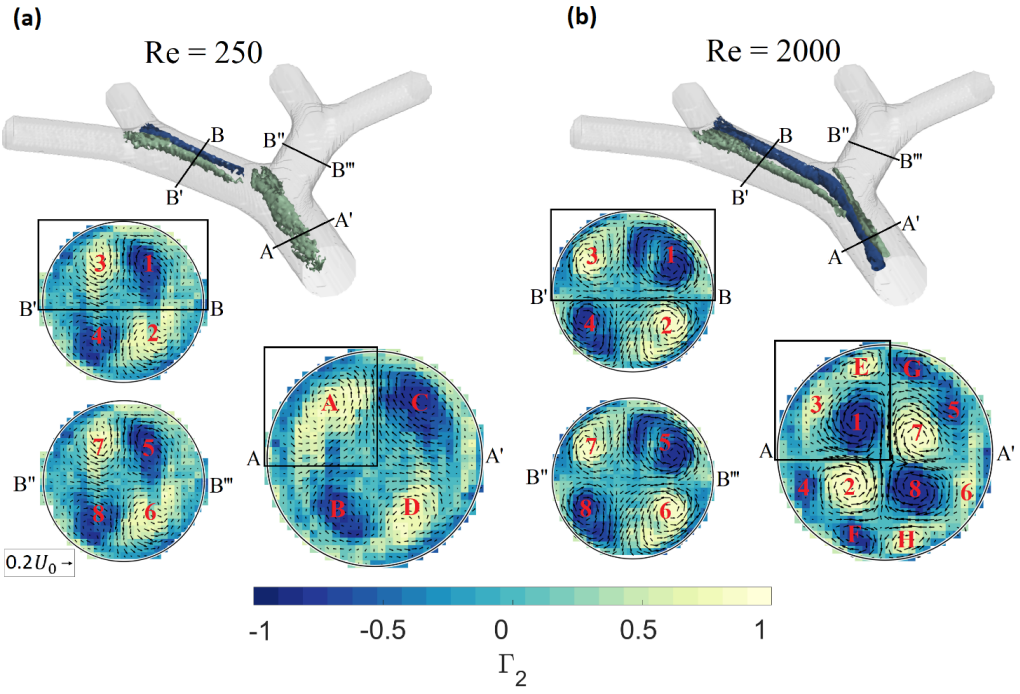

Figure 2.18: Isosurfaces of positive (light color) and negative (dark color) Γ_2 identifying vortical structures, and contour maps of Γ_2 with secondary flow vectors at various cross sections for steady exhalation at Re =250 **a)** and Re=2000 **b)**. The isosurfaces are only shown in the part of the domain boxed in the cross sections.

In **Figure 2.19** we use top-bottom symmetry and plot the average circulation for pairs of mirrored vortices (1-2, 3-4, 5-6, and 7-8) normalized by the fluid viscosity. $/nu$ is essentially a Reynolds number based on the characteristic vortex size and rotational

velocity. At Re =250 [Fig. 2.19 (a)] the vortex pairs on the left and right sides of each cross sections have similar strength, confirming that the local bifurcation geometry (which is left-right symmetric) determines the flow features at this low Re. These vortices dissipate along G_1; the newly created ones in G_0 have comparable circulation but undergo a somewhat milder streamwise decay, possibly because the larger branch provides less confinement. As expected, at Re =2000 [**Fig. 2.19 (b)**] the circulation levels in G_1 are an order of magnitude higher than the ones at Re =250. The nonlocal geometry effects are also significant and show their footprint already at the beginning of G_1: vortices 3-4 are sizably more intense than 1-2, being affected by the later turn into G_0. As they penetrate the branch, their circulation diffuses rapidly but both pairs remain strong enough to propagate into G_0. There, vortices 1-2 become stronger than 3-4 due to the mutual interaction with the twin pair 7-8. Vortices 3-4 instead are squeezed along the lateral side of the branch and loose strength [see cross-section A-A in **Fig. 2.18 (b)**]. Comparing all Re cases it appears that, for the present bifurcation geometry, streamwise vortices that reach the junction with a normalized circulation above $\frac{\Gamma}{nu} \approx 100$ propagate through it and into the downstream branch. This is not proposed as a criterion but rather as an indication. It is consistent with the inspiratory flow results in the previous section, in which only vortices that arrived at the bifurcation with circulation above $frac\Gamma nu \approx 50$ survived to the next generation [see **Fig. 2.16**, where the lower limit appears to be $frac\Gamma U_0 D_0 \approx 0.1$ for Re=500].

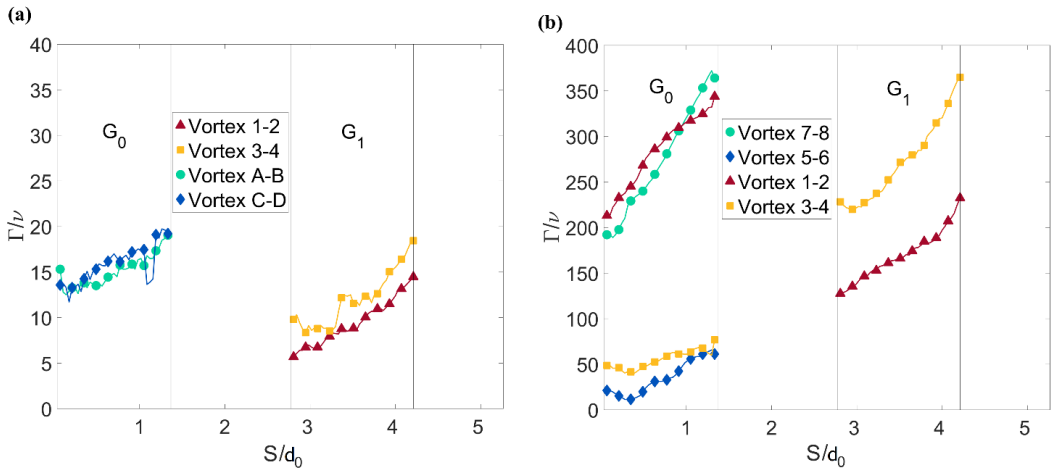

Figure 2.19: Normalized circulation Γ of the streamwise vortices in steady exhalation at **a)** Re=250 and **b)** Re =2000. The flow direction is towards smaller values of the abscissa

Chapter 3

Oscillatory flow in Weibel model

3.1 Overview

During the breathing cycle, the alternation of inspiratory and expiratory phases results in an intrinsically time-dependent flow. Depending on the respiration frequency, the velocity fields may significantly differ from those found in steady conditions, especially close to the inversion between inspiratory and expiratory phases (J. S. Andrade 1998, Z. Zhang 2002) . The level of unsteadiness is quantified by the Womersely number, i.e., the ratio of the unsteady and viscous forces, $Wo = a\sqrt{(\omega/\nu)}$ (where $a = D_i/2$ is the radius of the branch and ω is the angular frequency of the breathing cycle). If the airways are considered rigid and the respiratory waveform sinusoidal (which are reasonable assumptions for the first several bronchial generations (C. Kleinstreuer 2010)) Re and Wo are sufficient to characterize the oscillatory flow regime in a given geometry. A combination of both parameters, the nondimensional stroke length $\frac{L}{a} = \frac{Re}{Wo^2}$ is also commonly used, where L is the average axial displacement of a fluid particle (equal to the stroke volume divided by the local cross-sectional area). Jan et al. (1989) carried out oscillatory flow experiments in a single bifurcation and mapped the flow behavior over the $\frac{L}{a} - Wo^2$ space, distinguishing between viscous, unsteady, and convective regimes.

In a system of successive bifurcations, the situation is complicated by the fact that Re and Wo vary along the bronchial tree. A major impulse for investigating various oscillatory regimes has come from the success of high-frequency ventilation (HFV). This is a technique of mechanical ventilatory support routinely used to treat acute lung injury

and respiratory distress syndrome, which uses higher-than-normal breathing frequencies and low tidal volumes (J. M. Drazen 1984, Y. Imai 2001). In HFV the tidal volume is much smaller than the lung dead space (the volume of inhaled air not taking part in the gas exchange), suggesting that transport modalities other than bulk advection are at play. Fredberg (1980) first argued this could be explained by an augmented diffusion resulting from the interaction between axial convection and radial diffusion, the latter being enhanced by turbulence and secondary motions. However, while the secondary flow strength is expected to increase with Re (F. E. Fresconi 2007, K. Bauer 2012), its dependence on Wo is not clear from the literature. For example, the measurements of Peattie and Schwarz (R. A. Peattie 1998) indicated weaker secondary flows with increasing Wo, while the simulations of Zhang and Kleinstreuer (2002) suggested they are marginally stronger at higher Wo. Beside secondary flows, the fast inversion of flow direction in HFV may produce counterflow, i.e., regions where the fluid moves in expiratory direction during inspiratory phases, and vice versa (K.B.Heraty 2008, J.Choi 2010, K. Bauer 2015,2017) [2730]. This may have important consequences on the fluid dynamics, as the strong shear destabilizes the flow. Additionally, the different inspiratory and expiratory velocity profiles cause a net drift during each respiration cycle, often referred to as steady streaming. This was first identified by Haselton and Scherer (1980), and it has since been regarded as one of the key gas exchange mechanisms in HFV (P. W. Scherer 1982, H. K. Chang 1984, J. J. Pillow 2005). However, Bauer et al. (2015) recently simulated the oscillatory flow in a realistic bronchial tree geometry and concluded that steady streaming plays a minor role in the overall transport. Simulations of respiratory flows in the upper or central airways are challenging, due to both the geometric complexities and the flow regimes, often turbulent or transitional and with spatially varying Re.

Direct numerical simulations and large-eddy simulations provide detailed and reliable insight but are very computationally expensive and often used for steady flow cases (C. L. Lin 2007, S. Miyawaki 2012, L. Nicolaou 2013, F. S. Stylianou 2016). Several studies have used laminar or Reynolds-Averaged Navier-Stokes solvers (J. K. Comer 2001, Y. Liu 2002, Z. Zhang 2005), but recent high-fidelity simulations suggest that significant unsteadiness persists deep in the bronchial tree (J. A. Bernate,2017). In this scenario, accurate and complete experimental measurements are essential. Volumetric

velocimetry techniques have matured in recent years and are increasingly applied to biomedical settings (S. Discetti 2018). Specifically, the 3D respiratory flow was investigated by stereo scanning PIV (T. Soodt 2013), particle tracking velocimetry (PTV) (T. Janke 2017), and MRV (S. Jalal 2016, A.J.Banko 2015). In the present study, we apply MRV to investigate the steady expiratory and oscillatory flow in a planar double bifurcation airway model. Along with the results for steady inhalation reported in Jalal et al. (2016), these experiments provide a detailed account of the fundamental flow features characterizing this canonical configuration. Particular emphasis is given to secondary flow structures, their interaction, and spatio-temporal evolution as a function of Re and Wo.

3.2 Methodology

The bifurcation geometry is identical to the one used in the steady flow studies in **chapter 2**. It is connected similarly to the configuration used in steady exhalation (**Figure 2.1 (c)**). The pumping system consists of the same custom piston pump mentioned in **Chapter 2**, featuring an aluminum piston sliding through a Plexiglas cylinder (85 mm in diameter) driven by a computer-controlled stepper motor (VXM controller, PK266 motor, Velmex). In all tests, four independent valves at the far end of the tubing are adjusted to maintain an equal flow rate through each granddaughter branch. We investigate oscillatory cases with Re = 2000 at peak flow rate and Wo (also defined at G_0) between 1.2 and 12. Taking G_0 as the trachea, this corresponds to respiration regimes ranging from sleeping to HFV. (In an adult, Wo = 12 corresponds to a ventilation frequency of approximately 5 Hz, which is in the typical range of clinical HFV applications (J. J. Pillow, 2005)). We choose a sinusoidal waveform for simplicity (F. E. Fresconi 2007, K. Adler 2007, A. J. Banko 2016) and in consideration of the relatively modest impact of the waveform shapes (J.Choi 2010). For a symmetric divide of the flow rate at each bifurcation, the local Reynolds number at generation G_{i+1} is a factor 2h smaller than at G_i (with $h = d_{i+1}/d_i$), and the local Womersley number is a factor h smaller. Therefore, for a given flow setting, the regime may evolve significantly along the branching tree (D. L. Jan 1989, J.Choi 2010, A. J. Banko 2016). As mentioned in earlier chapters, in the present model h is ≈ 0.8 for

the G_0-G_1 bifurcation and ≈ 0.7 for the G_1-G_2bifurcation, both within the anatomical range for human airways (E.R.Weibel 1963, K.Horsfiel 1968, T. Van de Moortele 2018). **Figure 3.1** displays the position corresponding to each generation in the $\frac{L}{a} - Wo^2$ parameter space for the four oscillatory cases investigated here, along with the regime classification proposed by Jan et al. (1989). The cases at Wo=1.2 and 3 are in zone IIIa, where the convective acceleration term of the momentum transport has leading importance and the viscous term has subdominant influence. The cases with Wo=6 and 12 are in zone IIIb, where the convective acceleration has leading importance and the unsteady acceleration has subdominant influence. According to this classification, the first two cases are expected to exhibit quasi-steady behavior, and the other two be more strongly time dependent. For all cases, the flow in the G_0 branch lies in the turbulent region of the convective zone, although the latter classification was based on dated results (T. J. Pedley 1977), and, to our best knowledge, it never received direct verification. The present MRV approach does not measure instantaneous velocities nor Reynolds stresses, and therefore the question of whether turbulent fluctuations occur is not addressed here.

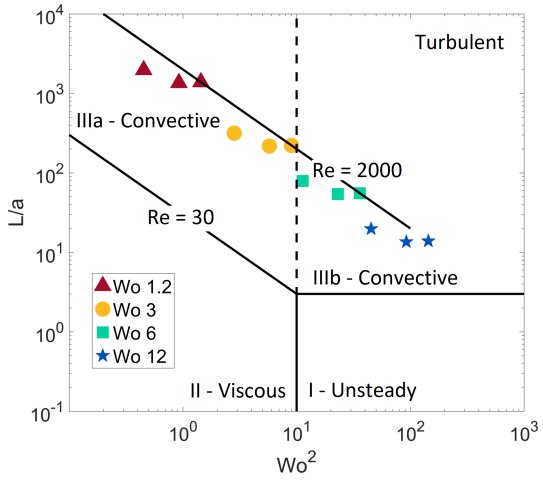

Figure 3.1: Position of the considered oscillatory cases in the flow regime diagram proposed by Jan et al

3.3 Phase-locked MRI

A 3T Siemens scanner for clinical MRI is used to obtain 3D, three-component velocities on a uniform Cartesian grid with 0.6 mm resolution, using the signaling sequence from Markl et al. (2012). The phase-resolved velocity is obtained by gating the MRI signal with a procedure similar to the one used by Banko et al. (2016). The sinusoidal waveform (corresponding to one respiration cycle) is divided into n time increments referred to as phases. The length of each phase defines the temporal resolution (in a phase-locked average sense) of the measurement, the velocity fields being averaged over each phase. In MRI the information is acquired in the spatial frequency domain (k space) and converted to physical space via inverse Fourier transformation.

Re	Wo	Venc [m/s]	SNR	Number of scans,N	$\frac{\delta_u}{u_0}\%$
2000	1.2	0.30	82.4	6	2.2 - 4.2
2000	3	0.50	62.3	6	5.2 - 8.7
2000	6	0.50	67.3	6	4.8 - 8.3
2000	12	0.30	91.5	6	1.5 - 3

Table 3.1: Nondimensional parameters, number of MRV scans, and ranges of relative uncertainty for the investigated cases

During each respiration cycle, only information relative to a specific region of k space is acquired. This is repeated until k space is filled, at the spatial frequency resolution corresponding to the desired resolution in physical space. As a trade-off between accuracy and measurement time, we choose n =18 for Wo=12 and n =10 for the lower Wo cases. Each scan lasts between 20 and 30 min. Similar to the steady cases, the working fluid is water infused with a low concentration (0.06 mol/liter) of CuSO4., which boosts the signal-to-noise ratio (SNR) without appreciably altering the fluid properties. For each case, 6 scans are acquired and averaged, increasing the SNR by a factor 6. Flow-off scans (performed with the same acquisition parameters but at zero flow rate) generate velocity fields that are subtracted from the raw data, removing potential bias errors associated with inhomogeneities of the magnetic field. The expected uncertainty in the MRV measurements, listed in **Table 3.1**, is estimated following Pelc

et al(1994).

Because of the highly 3D nature of the flow in the bifurcation, the same value of Venc is applied in all three directions. Errors can be significantly larger close to the wall, due to the possibility that a voxel intersects a solid boundary (partial volume effect). This is partly mitigated by masking the domain with a threshold based on the signal magnitude. An outlier detection method is applied based on the local normalized median of velocities, and rejected vectors are replaced with the median of the neighboring vectors. This issue does not affect the conclusions drawn from the present study since we do not attempt the analysis of the near-wall dynamics (for example through wall shear stresses). **Figure 3.2** shows the flow rate measured by integrating the MRV velocity field over the cross-section A-A. The scatter around the imposed sinusoidal waveform are attributed to: MRV uncertainty, including partial-volume effect, averaging of the time-varying flow field over each phase, and small compliance of the plastic tubing connecting the pump and the bifurcation model, possibly causing some phase shift.

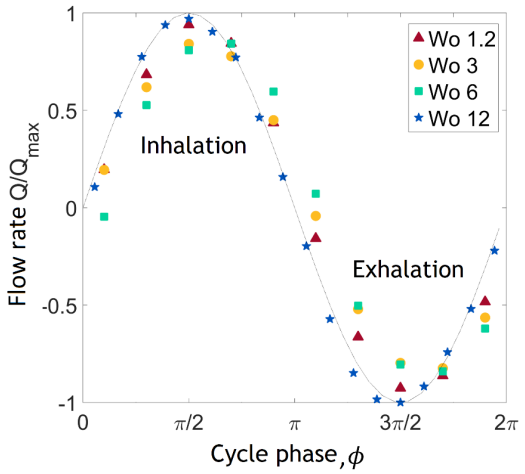

Figure 3.2: Measured flow rate at each phase for all Womersley numbers plotted against the theoretical waveform

3.4 Streamwise velocity

We analyze here the flow features in the case of an imposed ventilation frequency and contrast them with steady inhalation and exhalation. **Figure 3.3** shows contours of

velocity magnitude along the bifurcation plane at Wo=1.2 for 10 successive, equally spaced phases within the breathing cycle. After an initial period in which the velocity is uniformly small (around the exhalation and inhalation inversion), the flow field shapes up to resemble the steady inhalation flow pattern observed in figure 2.5. The signature feature is the skewed velocity profile in G_1, with high-momentum fluid along the inner side of the bifurcation and slow fluid along the outer walls. We note that the boundary conditions are different with respect to the steady inhalation case in **Chapter 2**; here the four G_2 branches have equal flow rates, while in the steady inhalation study had equal outlet pressure; still, the similarity is remarkable.

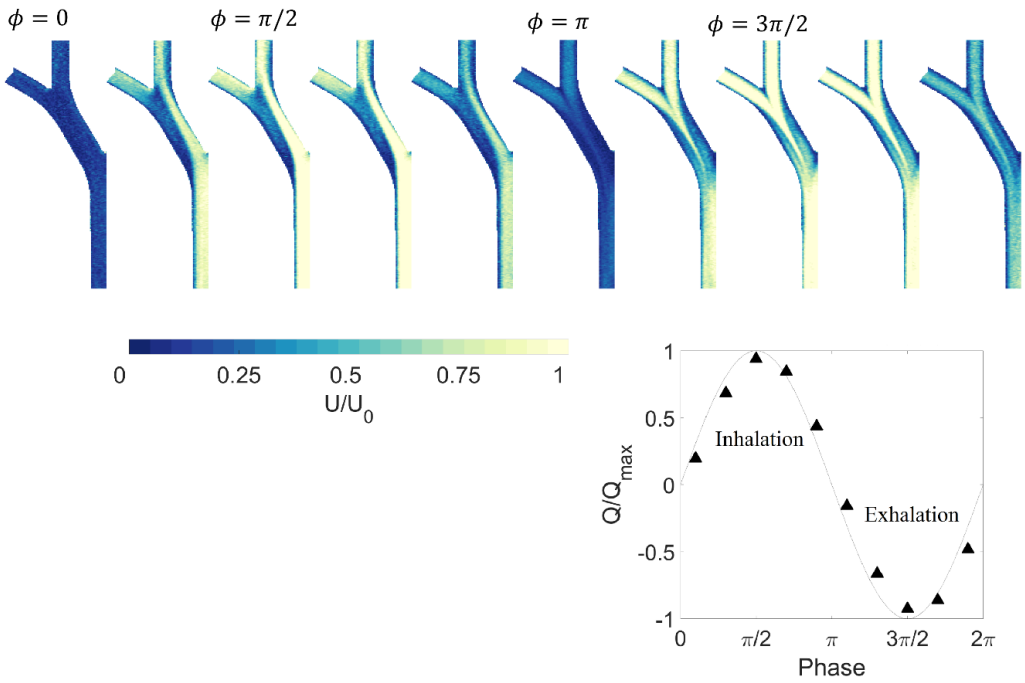

Figure 3.3: Contours of velocity magnitude along the bifurcation plane at Wo=1.2 and peak Re=2000 during the breathing cycle. The corresponding phase within the oscillatory cycle is labeled above the corresponding contour plots and by the flow rate diagram on the bottom right.

During inhalation, the velocity field is modulated in magnitude by the time-varying

inflow, but essentially maintains the same spatial distribution. This is true also during exhalation, where again the flow closely resembles the respective steady condition (see **Fig. 2.9**). The main feature is the jetting from the G_2branches that merge to create a sharp high-momentum region in G_1, propagating almost into G_0. Very similar observations can be made for Wo=3 and Wo=6 (not shown).

Figure 3.4 displays velocity distributions for Wo=12, at 10 out of the 18 reconstructed phases in the cycle. At the beginning of inhalation, the velocity magnitude tends to be higher close to the wall than at the center of the branches. This is due to a phase lag between the core flow and the boundary layer and is a signature feature during the inversion phase of high-frequency oscillatory flows (K.B.Heraty 2008, J.Choi 2010, K. Bauer 2017, J. R. Womersley 1955). During the first part of inhalation (referred to as the acceleration part, during which the flow rate increases with time), the velocity magnitude is quite homogeneous except for slower regions close to the carinas. In the second part of inhalation (deceleration), the flow assumes the characteristic topology found in steady conditions, with high or low momentum fluid on the internal or external side of the G_1 branches. At the inversion between inhalation and exhalation, the flow is again faster along the walls than in the branch core. This is followed by a phase in which the velocity magnitude is almost homogeneous. Then, during the deceleration part of exhalation, the flow from G_{2M} and G_{2L} becomes jet-like and merges into G_1, following the pattern seen in steady exhalation (**Fig. 2.9**).

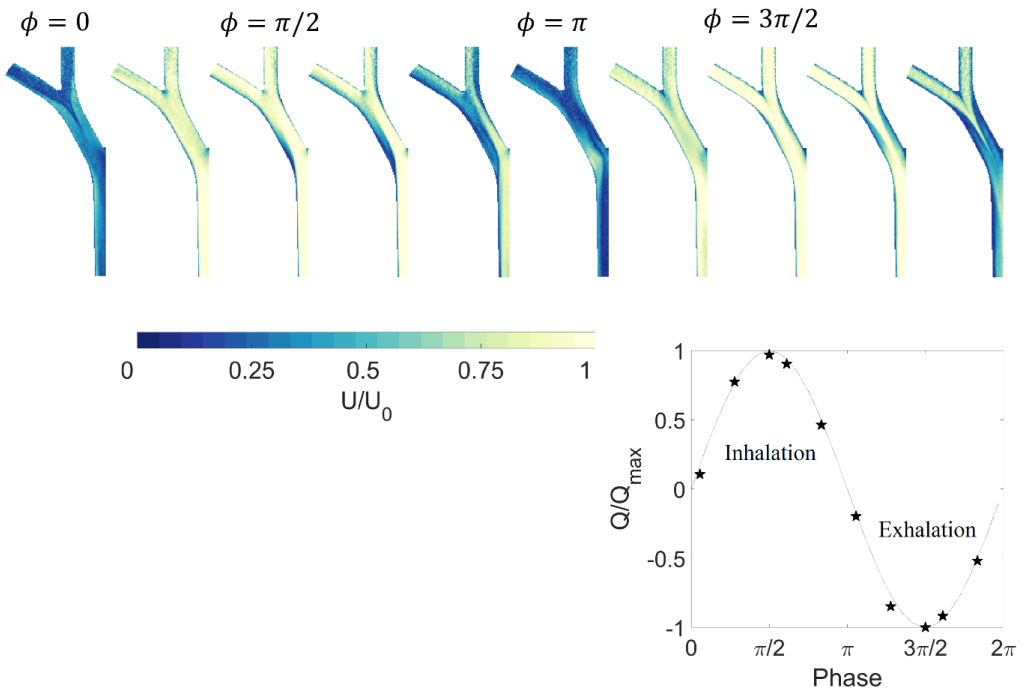

Figure 3.4: Contours of velocity magnitude along the bifurcation plane at Wo=12 and peak Re=2000 during the breathing cycle. The corresponding phase within the oscillatory cycle is labeled above the corresponding contour plots and by the flow rate diagram on the bottom right.

To illustrate the temporal progression of the 3D flow, in **Fig. 3.5** we display velocity iso-surfaces for all 18 successive phases of the cycle at Wo=12. We plot iso-surfaces of Uax, where we take as positive (negative) the velocity in the direction of inhalation (exhalation). The positive or negative levels correspond to 50% of the maximum or minimum velocity at each phase. At the beginning of inhalation [**Fig. 3.5 (a)**], the high-momentum fluid is found mostly along the perimeter of the branches, as noted above. Counter-flow regions appear along the core of the G_1 branches near the G_1-G_2junction and disappear as the inspiratory flow rate increases (b-e). In the deceleration part of inhalation, reverse flow pockets form on the outer side of the G_0-G_1 junction (f) and become larger as the inhalation-to-exhalation inversion is approached (g-i). At the beginning of exhalation (j), the counterflow regions enlarge and dominate the field,

with the fast-moving flow (now from G_2towards G_0) again found near the walls. In this phase, a prominent reverse flow region occupies the central region of the G_0-G_1 junction adjacent to the carina. This recedes as the expiratory flow rate increases, and the high-momentum structures jetting from G_2into G_1 develop in the second part of exhalation (k-q). Finally, close to the exhalation-inhalation inversion, new counterflow regions (directed in inspiratory direction) form on the lateral sides of G_0 and G_1 (r). These will grow into the dominant flow features seen in the inhalation phase (a), closing the cycle. The temporal extent of the counterflow regions is noteworthy. As expected, they tend to form close to the inhalation-exhalation and exhalation-inhalation inversions. In both cases, reverse flow pockets are found both along the core of the branch and along the sidewalls. While these regions are short-lived during the exhalation-inhalation inversion (a, r), they last for the entire deceleration part of inhalation and through the inhalation-exhalation inversion (f-j).

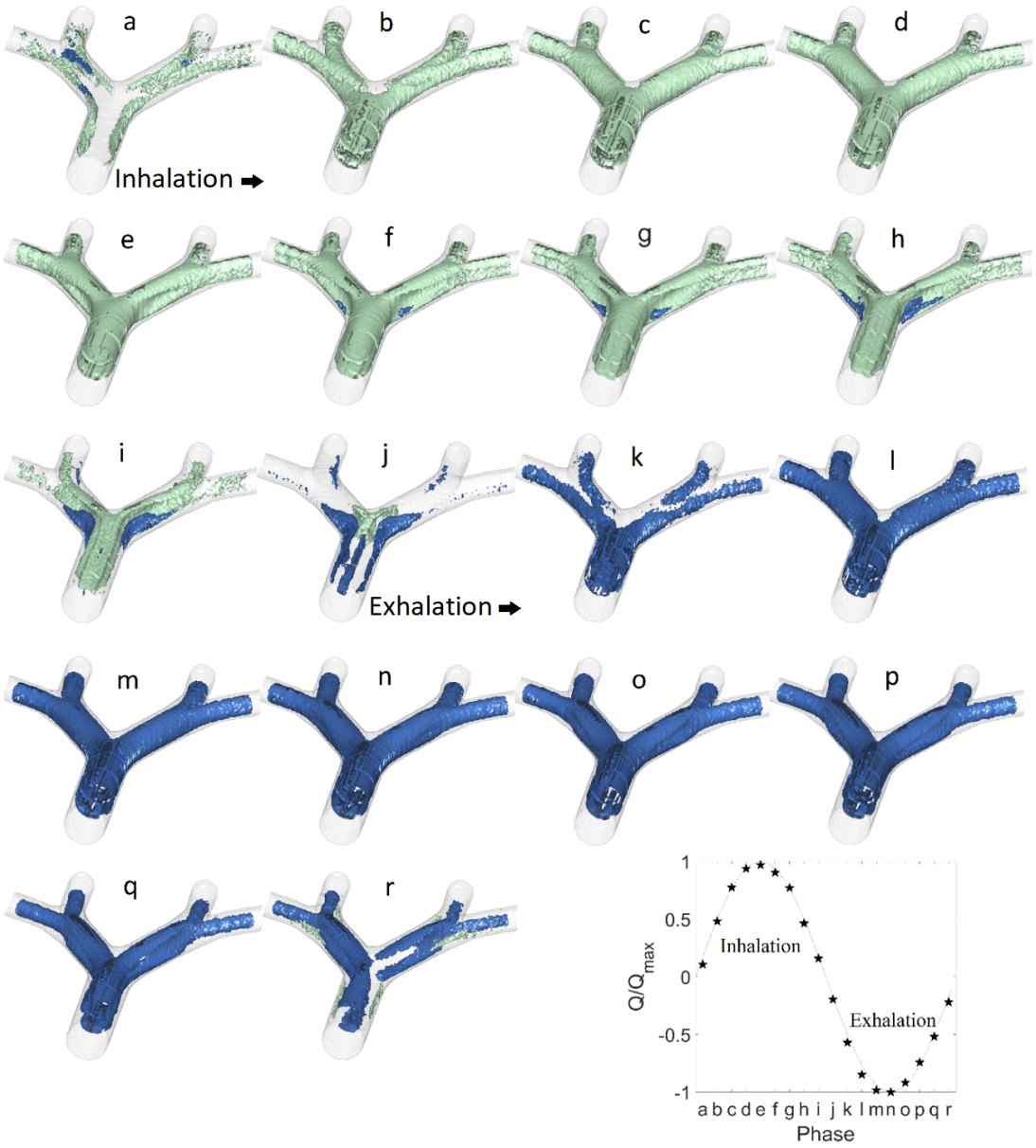

Figure 3.5: Velocity isosurfaces for successive phases of the inhalation and exhalation cycle at Wo=12. Light and dark colors indicate flow moving in the inspiratory and expiratory direction, respectively.

A similar analysis for Wo=6 also reveals the presence of counterflow regions, though

these are smaller and primarily confined to the exhalation and inhalation and inhalation and exhalation inversions. These are highlighted in **Fig. 3.6**, where the positive or negative iso-surface levels correspond to 40% of the maximum or minimum velocity at each phase. Counterflows are hardly visible above the noise floor at Wo=3, and they are absent at Wo=1.2. Past studies have found that forward and reverse flow occupied comparable portions of the bifurcation (K.B. Heraty 2008). Here on the other hand, even at Wo=12 the reverse flow regions account for a relatively small fraction of the fluid volume. Quantitative discrepancies with previous investigations may be due to multiple factors, including: the bifurcation geometry (for example, in terms of h and θ; see the discussion in Choi 2010 on the influence of these parameters); the inflow and outflow boundary conditions; the Reynolds number; and the presence of successive bifurcations. In particular, we note that most previous studies investigating the presence of counterflow considered single-bifurcation geometries (R. A. Peattie 1998, K.B. Heraty 2008, J.Choi 2010).

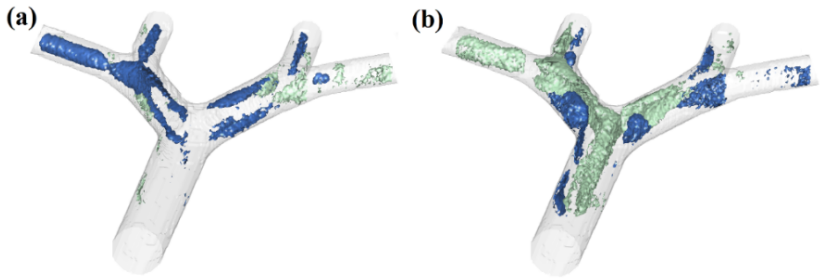

Figure 3.6: a) Velocity isosurfaces at exhalation and inhalation inversion and b) inhalation and exhalation inversion for the case Wo = 6, light and dark colors indicate flow moving in inspiratory and expiratory direction, respectively

3.5 Secondary flows

We now focus on the time-evolving secondary motions, which we describe using similar quantities as for the steady flow. **Figure 3.7** displays iso-surfaces of $\Gamma_2 = \pm 0.45$, as well as cross sections at G_0 and G_1 for the cases Wo=1.2 and Wo=12, close to peak inhalation and peak exhalation. The cases Wo=3 and Wo=6 (not shown) exhibit qualitatively similar features as Wo =1.2. At peak inhalation [**Figs. 3.7 (a)** and **26(b)**],

independently of Wo, the Dean mechanism generates two counter-rotating vortices at G_1, as seen in the steady inhalation case at the same Re. The spatial resolution in the relatively small grand-daughter branches is not sufficient to unequivocally identify the flow structure. However, from the Γ_2 iso-surfaces, it appears that the counter-rotating vortices in G_1 propagate into the medial G_2branch, similarly to the steady case; while for the highest Wo the main secondary motions are consistent with a Dean mechanism driven by the local curvature. At peak exhalation [**Figs. 3.7 (c)** and **3.7 (d)**], G_1 resembles again the steady inspiratory flow, with four counter-rotating vortices present in all investigated Wo cases.

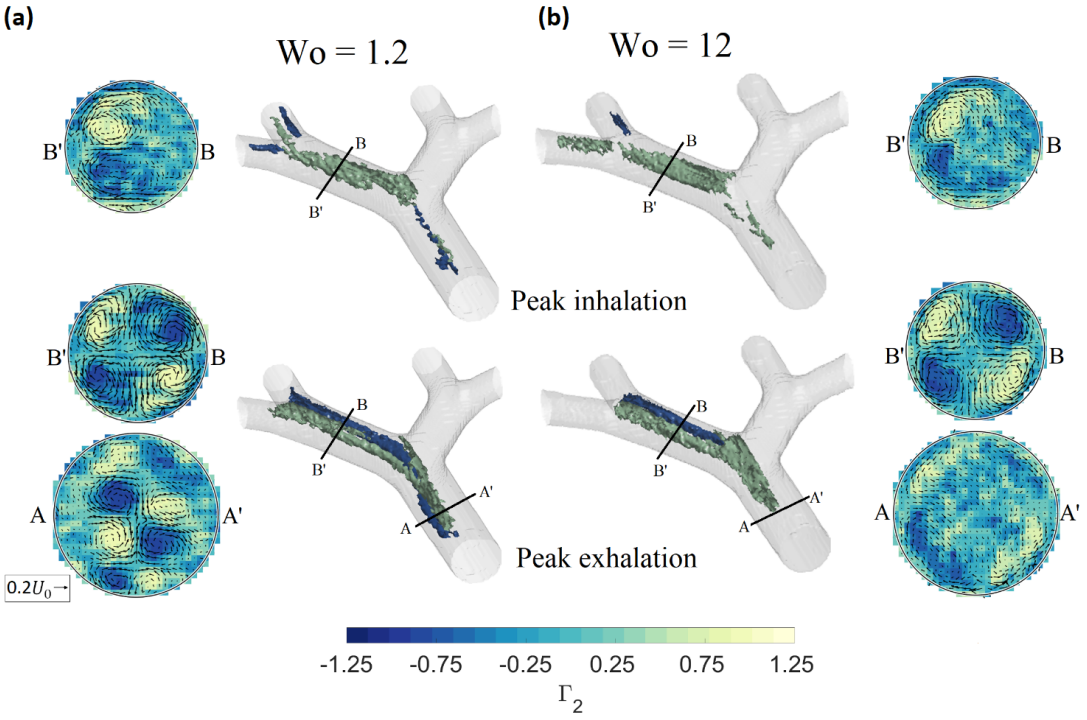

Figure 3.7: Γ_2 isosurfaces and cross section contours with in-plane velocity vectors, identifying vortical structures Wo = 1.2 a) and 12 b), at peak inhalation and peak exhalation

On the other hand, the flow in G_0 is very different depending on the oscillatory frequency: at Wo=1.2 the topology follows the steady exhalation pattern, with a system of multiple counter-rotating vortices propagating from G_1; instead, at Wo=12 only

four vortices are present. The likely reason is that, in the high-frequency case, the core region of the branches is characterized by reduced momentum and thus the vortices located in that area are not advected from G_1 into G_0. Taken together, these results indicate how, at low and intermediate Wo, the secondary flows at peak inhalation and exhalation resemble the steady cases; whereas at high Wo the differences in the momentum distribution are reflected in the transport of streamwise vorticity and result in different secondary flow structures. Beside the presence and spatial extent of specific vortical structures, it is of interest to quantify the evolution of the overall secondary flow strength during the oscillatory cycle. Here we focus on G_1, which is the generation least affected from boundary and inflow conditions.

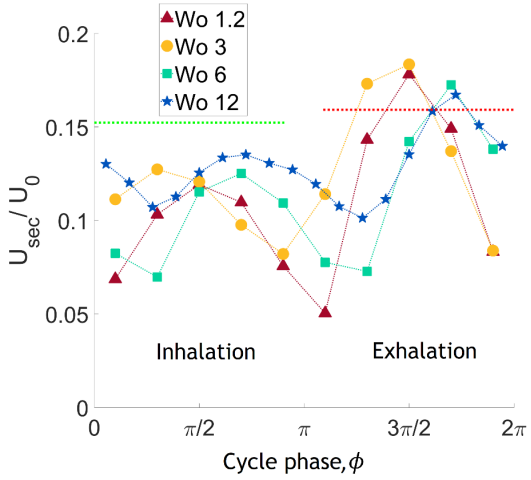

Figure 3.8: Time-varying secondary flow strength averaged along G_1, for all considered Wo; the steady inhalation and exhalation levels are also shown for comparison

Figure 3.8 plots the secondary velocity (normalized by the peak bulk velocity U_0) averaged along the straight portion of this branch, for all phases and all investigated Wo; the steady inhalation and steady exhalation levels are also shown for comparison. Several observations are in order. The peaks of secondary flow strength are reached close to the phases of maximum flow rate, which is consistent with the fact that the streamwise flow induces the pressure gradients driving secondary motions. The peaks for the higher Wo cases tend to lag those at lower Wo, possibly due to the lag between pressure (and therefore pressure gradients leading to secondary flows) and velocity waveforms at high

Wo (Z. Zhang 2002); however, this effect is hard to quantify due to the limited temporal resolution. The secondary motions are more intense in exhalation than in inhalation, in both steady and oscillatory conditions. This can be explained by the fact that the bulk streamwise velocity decreases along the inspiratory path and increases along the expiratory path; therefore, during exhalation the spatial acceleration acts to augment streamwise vorticity (via the vortex-stretching term in the vorticity transport equation), and vice versa during exhalation. A similar argument was used by Coletti et al. (2013) to illustrate the stronger and weaker counterrotating vortices formed by a jet issued into a crossflow under favorable or adverse pressure gradient.

The secondary flow strength at peak inhalation is lower compared to the steady case at matching Re, while the opposite is true for peak exhalation. A possible explanation is that the change in secondary flow strength is not symmetric in time, but rather follows a cliff-ramp pattern, as suggested by the curve for Wo=12. This may result in the temporal acceleration term playing a larger role during the first part of exhalation, when the rate of change of Usec is steeper. The different boundary conditions between the steady cases and the oscillatory ones might also explain, at least in part, the behavior. This point, however, deserves further investigation. Overall, the higher Wo cases display smaller temporal variations of secondary flow strength, and therefore the Wo=12 case is closer to the steady levels compared to those at lower frequency. In terms of Wo dependence, the conclusion is that (at the considered Re) higher Wo leads to stronger secondary flows during inhalation and weaker secondary flows during exhalation.

3.6 Steady streaming

The measurements of spatially and temporally resolved velocity fields allow us to quantify the phenomenon of steady streaming. At each location, we calculate the streaming (or drift) velocity U_D as the cycle-average of the streamwise velocity Uax, thus generating a volumetric field. A similar approach was followed by Peattie and Schwarz (1998), who, however, used LDV and reported only a few profiles along the plane of the bifurcation. UD is taken as positive (negative) when directed in inspiratory (expiratory) direction.

In **Fig. 3.9** we display iso-surfaces at UD =30% of the maximum or minimum

velocity and selected cross-sections for all considered Wo cases. At Wo=1.2, the drift velocities are relatively high in both directions, with peaks of $U_D/U_0 = \pm 0.4$ in G_1. (We remark that the inspiratory and expiratory drift need to balance out since the cycle-average over each cross section is zero.) At G_0, most of the cross section sees a weak inspiratory drift, flanked by layers of expiratory drift along the top and bottom sides. This is in contrast with the common picture of steady streaming in the mother branch, where the expiratory drift rather occupies the lateral side of the cross section. This latter type of pattern was obtained in single bifurcations with long mother branches (R. A. Peattie 1998, F. R. Haselton 1980) and non-planar multiple bifurcations (K. Bauer, 2015). The discrepancy with the present results underscores the impact of the geometry and inlet conditions on the drift velocity field. G_1 shows the greatest contrast between inspiratory streaming along the inner part of the bifurcation, and expiratory streaming over the central and outer part of the branches. This is consistent with the behavior observed during the inhalation and exhalation phases: in the former the high momentum is located close to the carina, while in the latter the merging jets from the granddaughter branches dominate the core of the cross section. A similar drift pattern is visible in G_{2M}, although there the inspiratory drift region wraps around the expiratory drift core. In G_{2L} the steady streaming is negligible. The U_D fields are qualitatively similar at higher Wo, but the magnitude decreases with increasing ventilation frequency. Overall, the drift velocity is about twice as high at Wo=1.2 compared to Wo =12. This can be ascribed to the more skewed streamwise velocity profiles in the low-Wo cases, as compared to the flatter profiles at higher oscillation frequency.

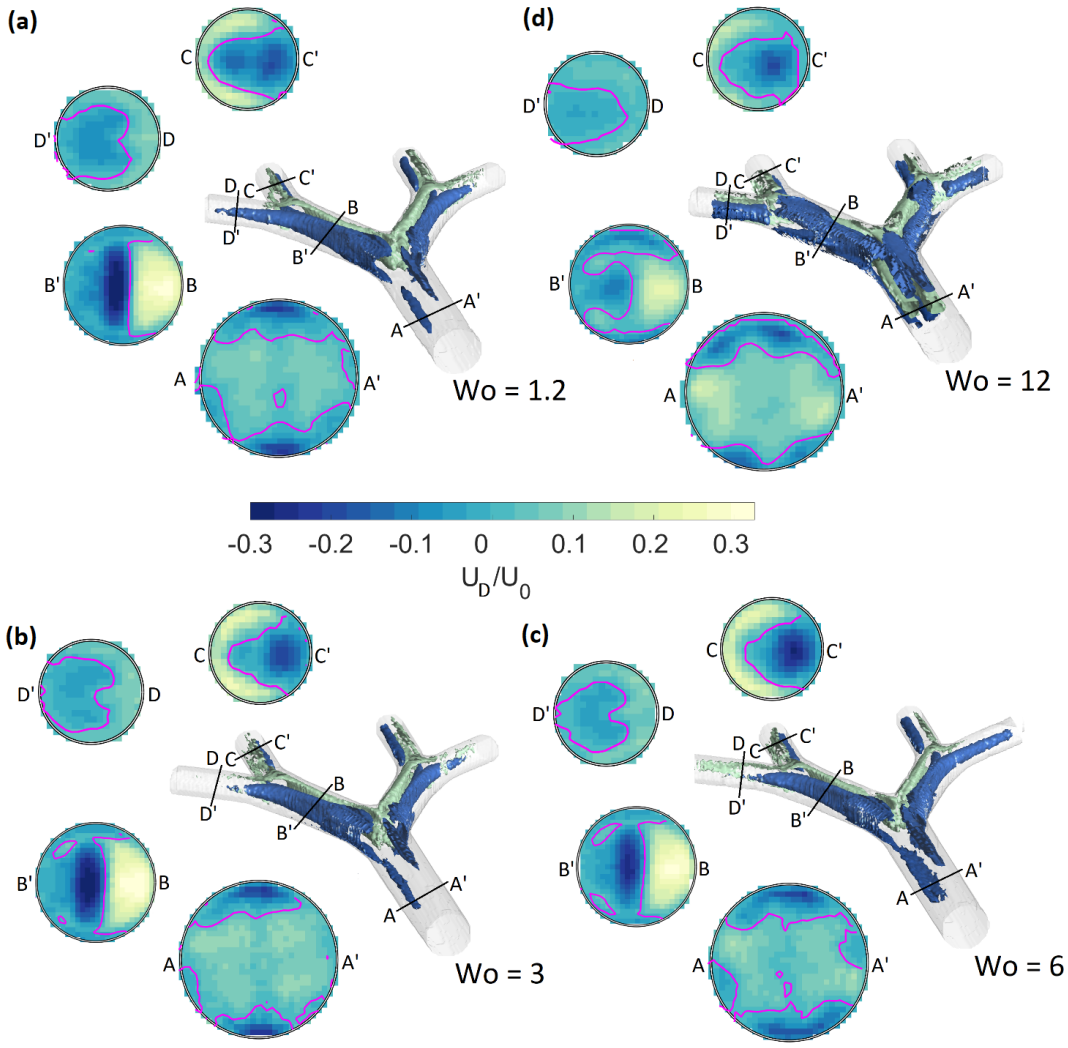

Figure 3.9: Isosurfaces and cross section contours of cycle-averaged drift velocity for all considered oscillatory cases Wo=1.2 **a)**, Wo=3 **b)**, Wo=6 **b)**, Wo=12 **d)**. Light and dark colors indicate inspiratory and expiratory drift. The purple lines indicate zero drift

Figure 3.10 quantitatively illustrates this fact by plotting, for several phases, Uax profiles at station B-B along the bifurcation plane [the same location of the profiles in Fig. 2.10 (a)], comparing cases Wo=1.2 and 12. At lower Wo, the inspiratory and expiratory peaks are more pronounced and placed at different locations in the cross

section. This sharpens the inhalation and exhalation asymmetry which is at the basis of the steady streaming mechanism (P. W. Scherer, 1982), and results in larger net transport. Recent simulations from Bauer et al. (2017) in a double-bifurcation geometry also indicate that the mean square displacement of non-diffusive particles over a given ventilation time decrease with the oscillation frequency. One should remark that Bauer et al. kept L/a constant (rather than Re) and therefore a direct comparison with the present data cannot be made.

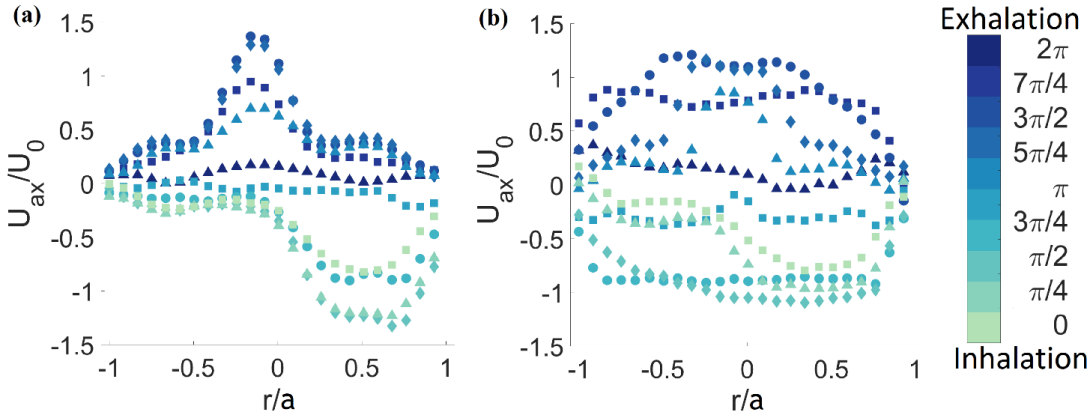

Figure 3.10: Streamwise velocity profiles along the bifurcation plane at B-B' for **a)** Wo=1.2 and **b)** Wo= 12, for the different phases in the cycle.

Chapter 4

Steady & oscillatory flow in a patient-specific model

4.1 Overview

While the idealized model provides fundamental knowledge about key mechanisms happening in the bronchial tree, it does not capture the full picture of respiratory fluid dynamics. Extending our study from the Weibel model to realistic airways is the obvious next-step to take, in improving our understanding. Several numerical studies (Zhang et al (2012), Lambert et al. (2011), Choi et al (2009), and more) were carried out on anatomically accurate models but only a few have (Banko et al. (2015,2016)) investigated this in an experimental setting. More specifically, in this chapter, we consider steady inhalation, steady exhalation and oscillatory flow in a healthy patient-specific geometry. The latter is directly related to High Frequency Ventilation (HFV), a technique often used to treat acute lung injuries and ventilate neonates who need ventilatory assistance during the first days of their lives. We also carry out the first experimental evaluation of steady streaming in realistic airways and deliver a comprehensive comparison with the Weibel geometry.

4.2 Methodology: CT scan, experimental setup and flow regimes

We considered a female subject (1.58 m and 79 kg, body-mass index of 31.45) with no smoking history and healthy lung function. Chest scans were acquired as part of the COPDGene study (Regan et al. 2011) using multi-detector computer tomography (MDCT) that resulted in a nearly isotropic image voxel size of about 0.3 mm3 (Washko et al. 2014). Scans are available both at full inhalation (total lung capacity, TLC) and at full exhalation (functional residual capacity, FRC). We segment the five lobes [right upper lobe (RUL), right middle lobe (RML), right lower lobe (RLL), left upper lobe (LUL), and left lower lobe (LLL)] at both TLC and FRC. This allows us to quantify the subject-specific ventilation ratios, i.e. the fractions of inhaled air directed to each lobe. These are listed in **Tab. 1** and are consistent with previously reported values (De Backer et al. 2010, Yin et al. 2010).

	RUL	RML	RLL	LUL	LLL
Ventilation fraction [%]	14	5	32	17	32

Table 4.1: Ventilation fractions in each of the five lobes

The experimental methodology to build the physical model is described in detail in Van de Moortele et al. (2018a, 2018b), and is summarized here for completeness. We use the TLC scan to reconstruct the bronchial tree from the trachea to the 7th generation of bronchial branching (in average), and the tree centerline is extracted via a semi-automatic skeletonization process. The bronchial branches belonging to each lobe are highlighted in **Fig. 4.1**. The reconstructed airways are used to generate a life-size hollow model. This is fitted in a vessel partitioned in five cavities, each collecting the distal bronchi of the respective lobe. The vessel and the airway tree are 3D-printed in one piece with a resolution that ensures hydrodynamically smooth surfaces. In using a rigid model based on a TLC scan for both inhalation and exhalation, we neglect the change in airway geometry during respiration. This is usually considered a fair assumption when investigating the central airways, due to their limited motion and

small change in cross-section (Kleinstreuer & Zhang 2010).

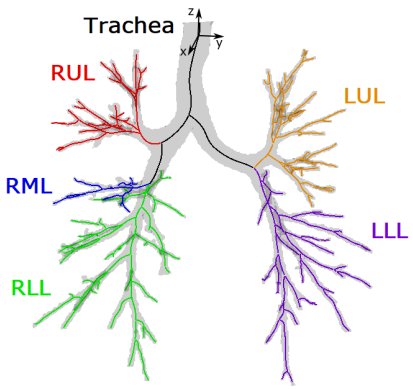

Figure 4.1: Geometry of the patient-specific model with centerlines at the trachea and each of the five lobes

The model is inserted in a flow loop circulating water doped with 0.06 mol/L of CuSO4, with plastic tubing connecting the trachea to a pumping system and the five lobes to a holding tank. For the steady inhalation and steady exhalation cases we use a centrifugal pump attached to a digital flow regulator (for details, see Chapter 2), while for the oscillatory flow case we use a computer-controlled piston pump (described in Amili et al. 2018 and in Chapter 3). The outlets of the lobar plena are each provided with needle valves and monitored via a clamp-on transonic flow meter. For the steady flow cases each lobar flow rate is adjusted to match the ventilation ratios in **Tab. 1.** The same valve settings are used for the oscillatory cases, which results in close agreement (within a few percent) with the same ratios at peak inhalation and peak exhalation. During the inversion phases (inhalation/exhalation and exhalation/inhalation), the lobar flow distribution changes significantly due to the impedance of the different segments in the bronchial tree, as we shall discuss in the Results section of this chapter.

In the MRV measurements the model is lodged in a helmet-shaped coil connected to a 3T MRI scanner. Three-dimensional, three-component velocities are obtained on a Cartesian grid at an isotropic resolution of 0.6 mm. Those are either time-averaged (steady cases) or phase-averaged (oscillatory cases), as described in chapter 2 and 3, where the acquisition and processing procedure are detailed. In all cases, four scans are

averaged to increase the signal-to-noise ratio, resulting in uncertainties of 5.5% (10.6%) of the bulk flow velocity (peak inhalation bulk velocity) at the trachea in the steady (oscillatory) case. For the oscillatory case, the waveform period corresponding to one breathing cycle is divided into 15 phases, and a velocity field is reconstructed for each of them. The piston pump generates a sinusoidal mass flow rate. The relatively high frequency, however, produces a dynamic load on the plastic tubing connected to the model. This causes a slight (sub-mm) dilatation of its diameter, which in turn results in a deviation of the imposed flow rate at the model inlet, thus only approximating a sine wave (**Fig. 4.2**). Using completely rigid piping would prevent this effect; but this would be hardly feasible given the several meters between the MRI scanner and the control room where the pump is located to shield it from the magnetic field. Past studies indicated that the precise shape of the waveform does not a have qualitatively significant impact on the fluid dynamics (e.g., Choi et al. 2010), though some effect was recently reported (Alzahrany et al. 2014).

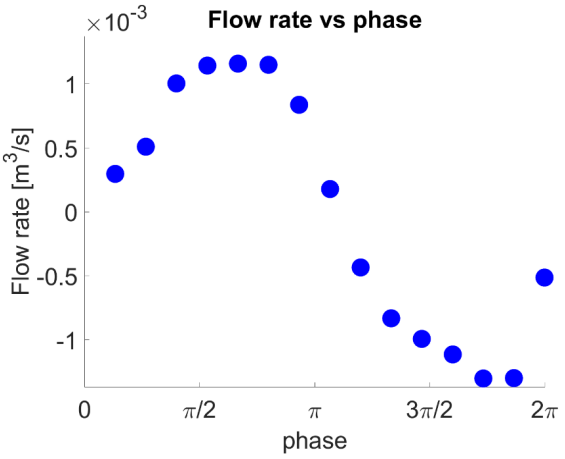

Figure 4.2: Measured flow rate for one breathing cycle

Table 4.2 summarizes the investigated cases. We characterize the flow regimes using the Reynolds number and (for the oscillatory case) the Womersley number, as defined previously. Here D_0 is the trachea hydraulic diameter at the location of the coordinate system , about 3 diameters upstream of the main carina), $U_0$is the corresponding bulk velocity, ν is the kinematic viscosity, and ω is the angular ventilation frequency. Re for steady exhalation, as determined by the MRV, is somewhat (less than 10%) lower than

in steady inhalation. Significant changes in flow features are not expected due to such difference (also in light of the inhalation results reported below over a much broader range of Re); therefore, in the following both steady cases are nominally labeled as Re = 1500. The two steady regimes (Re = 1500 and 4500) span conditions between quiet breathing and light exertion, while the oscillatory case at Wo = 12 is relevant to HFV.

	Steady Inhalation	Steady Exhalation	High Frequency Ventilation
Re_0	1500; 4500	1370	1500
Wo_0	-	-	12

Table 4.2: Nondimensional parameters for the investigated cases

4.3 Steady regimes

We begin by considering the evolution of the Reynolds number along the bronchial tree. This is defined by the local hydraulic diameter and bulk velocity at each branch cross-section. The bulk velocity is the cross-sectional average of the axial velocity Uax; this is defined at each voxel as the component parallel to the closest centerline segment, whose orientation is fine-tuned via an automatic optimization procedure based on continuity (Van de Moortele et al. 2018a).

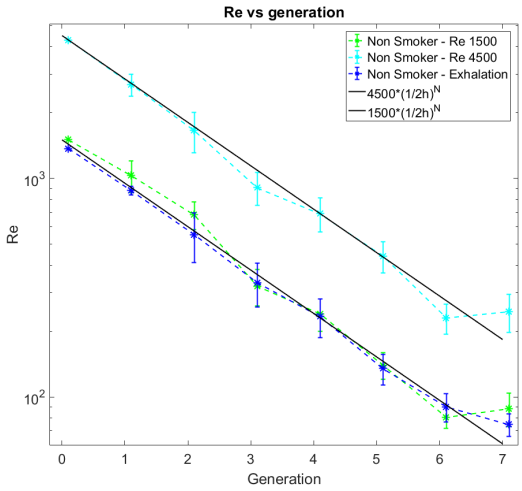

Figure 4.3: Generation-averaged Reynolds values, with error bars representing the standard deviation among the various branches 56at that generation.

In **Fig. 4.3** we plot the generation-averaged Re values, with error bars representing the standard deviation among the various branches at that generation. In these and in following plots, the generation-averaged quantities are measured along the central 50% of the length of each branch, avoiding the influence of the bifurcation region. Moreover, one should keep in mind that in the expiratory case the flow is from higher to lower generation numbers. The trend follows closely the theoretical behavior expected in a symmetric dichotomous model where the flow rate splits equally between both sibling branches: $Re_{i+1} = \frac{Re_i}{2h}$. Here the subscript indicates the generation number and h is the child-to-parent diameter ratio. The latter is taken as $h = 2^{\frac{-1}{3}} \approx 0.79$ according to the Hess-Murray law that minimizes viscous dissipation (Hess 1914; Murray 1926; Weibel 1963). We recently found that this value closely predicts actual anatomic proportions in a cohort of 36 subjects, including the present one (Van de Moortele et al. 2018). In the same study we also showed frequent large asymmetries in the size of sibling branches. Yet, the simple estimate from Eq. 1 appears to predict the trend reasonably well for all steady cases. The logarithmic scale in the plot, however, should not hide to the viewer the potentially large local differences between branches as suggested by the significant standard deviations. These will be discussed below.

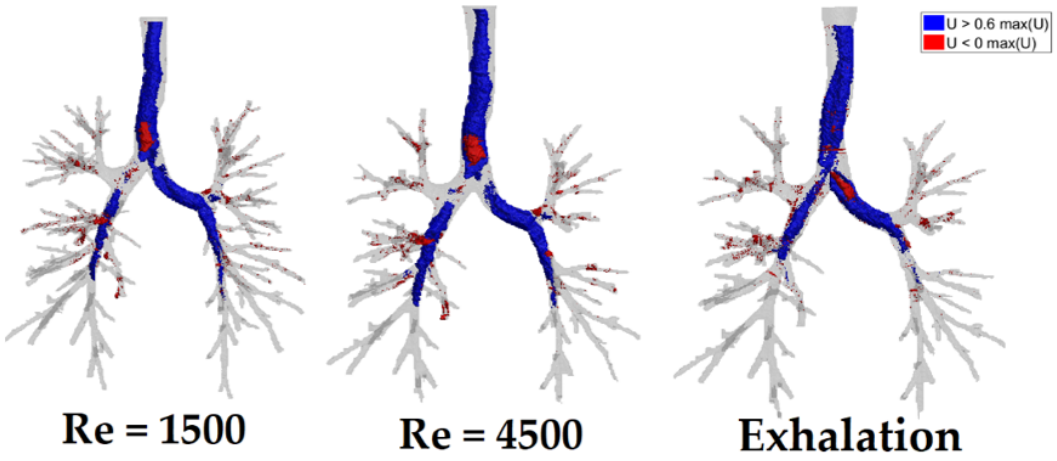

Figure 4.4: Contours of positive (blue) and negative (red) axial velocity distribution along the airway tree at all regimes

Figure 4.4 also provides information on the axial velocity distribution by displaying, for the steady cases, isosurfaces of $U_{ax} = 0.6 \times U_{axmax}$, in blue; Uax,max is the maximum axial velocity in the flow field) and $U_{ax} \leq 0$ (in red). The former represents high momentum regions, which again appear to extend deeper in the lower lobes. The latter represents reverse flow region, as the fluid inside those isosurfaces has negative axial velocity. Flow reversal is consequential for gas mixing, particle transport, and mechano-transduction at the epithelium, and was documented for HFV regimes in both idealized and realistic geometries (Heraty et al. 2008, Choi et al. 2010, Jalal et al. 2018). Here sizeable pockets of flow reversal appear also in steady conditions, especially at the main bronchial bifurcation. This is true for both inhalation and exhalation. However, the position and extent of such pockets is different, and in general flow reversal is less prevalent in exhalation. This is consistent with the expiratory velocity profiles being, and so less prone to separation, than the inspiratory. This was noted in previous studies focused on idealized geometries (e.g., planar, symmetric bifurcations), and appeared due to the flow merging and associated secondary flows at the bronchial junctions (Pedley 1977, Zhao & Lieber 1994, Jalal et al. 2018). In inhalation, the Reynolds number only weakly affects the shape and location of the reverse flow regions, although it increases their size. Compared to the idealized cases, we see large differences in the reverse/slow

flow regions: here they are located above the main bronchial bifurcation, whereas in idealized bifurcations they are found along the external sides (Jalal et al. 2016).

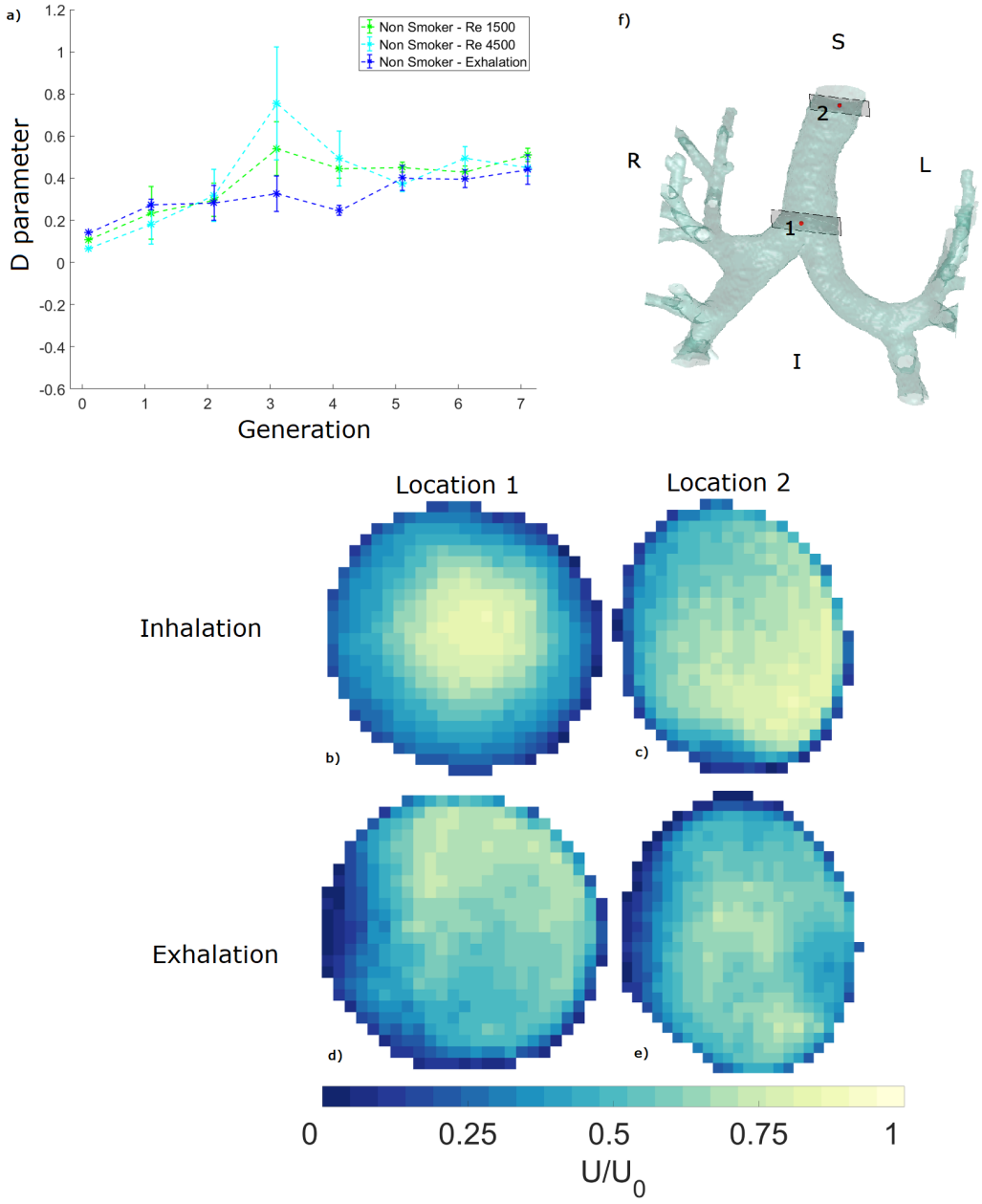

Figure 4.5: **a)** D parameter at all generations for all regimes **b)- e)** cross-sections of axial velocity normalized by U_0 at two locations shown in **f)**

To characterize the profile of axial velocity, we use the momentum distortion parameter D defined in **Equation** in **Chapter 2**. D represents the relative difference between the measured momentum flux and that of a plug flow carrying the same flow rate. It is a measure of axial dispersion due to the mean flow, being associated to the amount of longitudinal strain experienced by the fluid at each cross section. **Figure 4.5 (a)** shows its evolution across the generations for the different steady cases. In inhalation, D increases up to the third generation, indicating that the flow velocity profiles become rapidly pointier, and then declines/plateaus. The close similarity between cases at Re0 =1500 and 4500 suggests that this trend is unlikely to be caused by a transition from turbulent to laminar flow along the tree. It is rather rooted in the propagation of flow features across successive bifurcations, contributing to an increasing skew-ness of the velocity profiles (Jalal et al. 2016). The plateau at higher generations is probably affected by the lack of resolution in the smaller branches, where the near-wall fluid layers cannot be captured accurately. In exhalation, D is generally lower, and it decreases along the flow path. This confirms that the velocity profile is flatter than in inhalation, which is illustrated by axial velocity contours in two sample locations (**Fig. 4.5(b,c)**) indicated in **Fig. 4.5 (f)** where S, I, R and L denote the Superior, Inferior, Right and Left orientation of the lung. The values are generally similar to those found in an idealized bifurcation by Jalal et al. (2016, 2018).

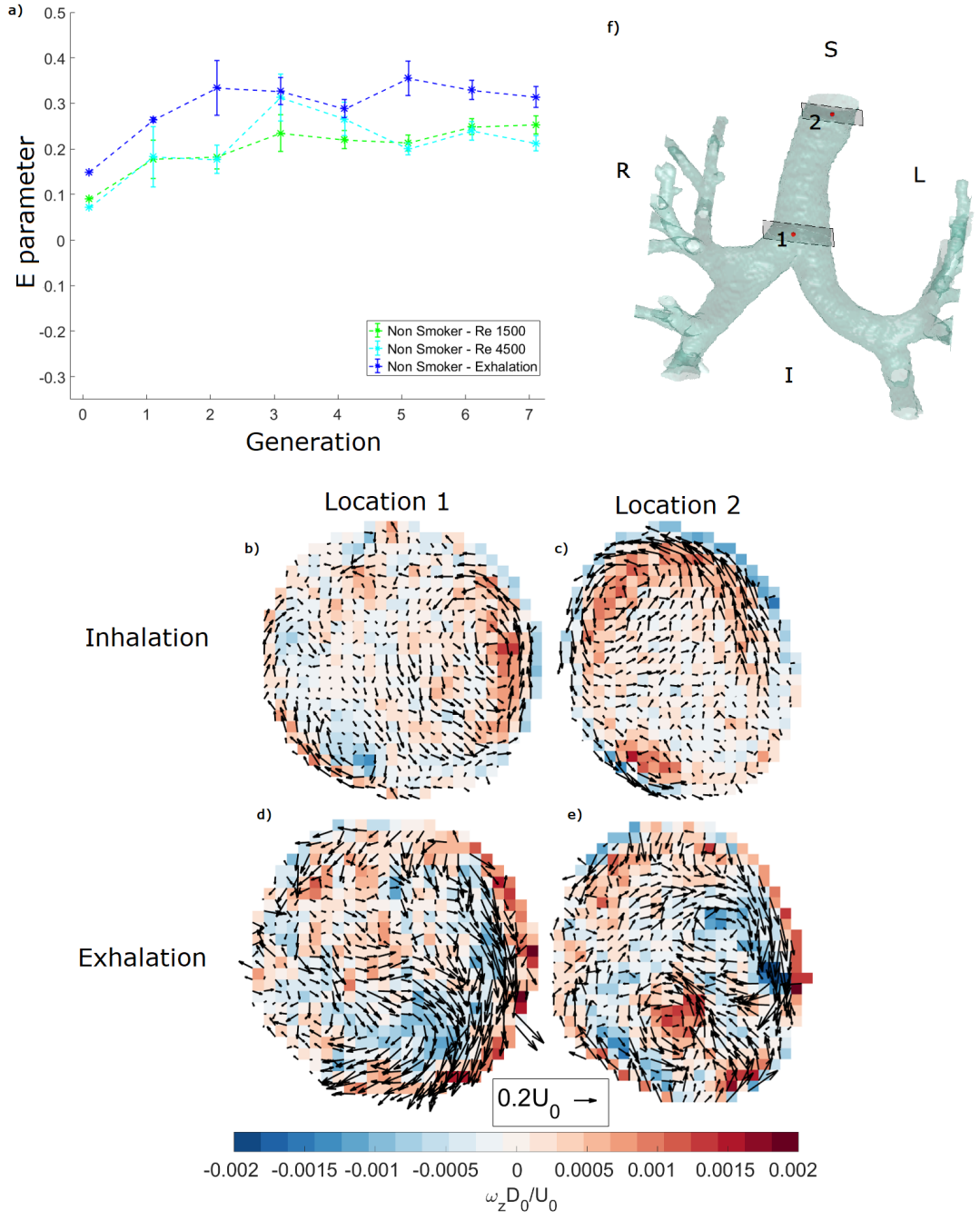

Figure 4.6: **a)** E parameter at all generations for all regimes **b)- e)** cross-sections of out-of-plane vorticity normalized by D_0/U_0 at two locations shown in **f)**

In order to quantify the secondary flows, which correlate with mixing in the airways (Fresconi & Prasad 2007), we utilize the E parameter, as defined earlier in **Equation** in **Chapter 2**. It represents the relative strength of the secondary velocity compared to the streamwise components over each cross-section. **Figure 6a** shows the evolution of E along the branching generations for all steady cases. During inhalation it increases sharply through the first three generations and plateaus deeper in the bronchial tree, with marginal effect of Re in the considered range. During exhalation E follows a similar trend across the bronchial tree but is significantly higher. This is consistent with the presence of intense secondary flows caused by the expiratory flow merging at the bronchial junctions, generating more numerous and vigorous streamwise vortices compared to inhalation (see sample cross-sections in Fig. 4.6 (b,c)). At various locations, we recognize the pattern of quadruplet generated by the interaction of two couples of Dean vortices (Zhao & Lieber 1994). However, the secondary flows in this realistic geometry are even stronger than in idealized bifurcations (Jalal et al. 2016, 2018).

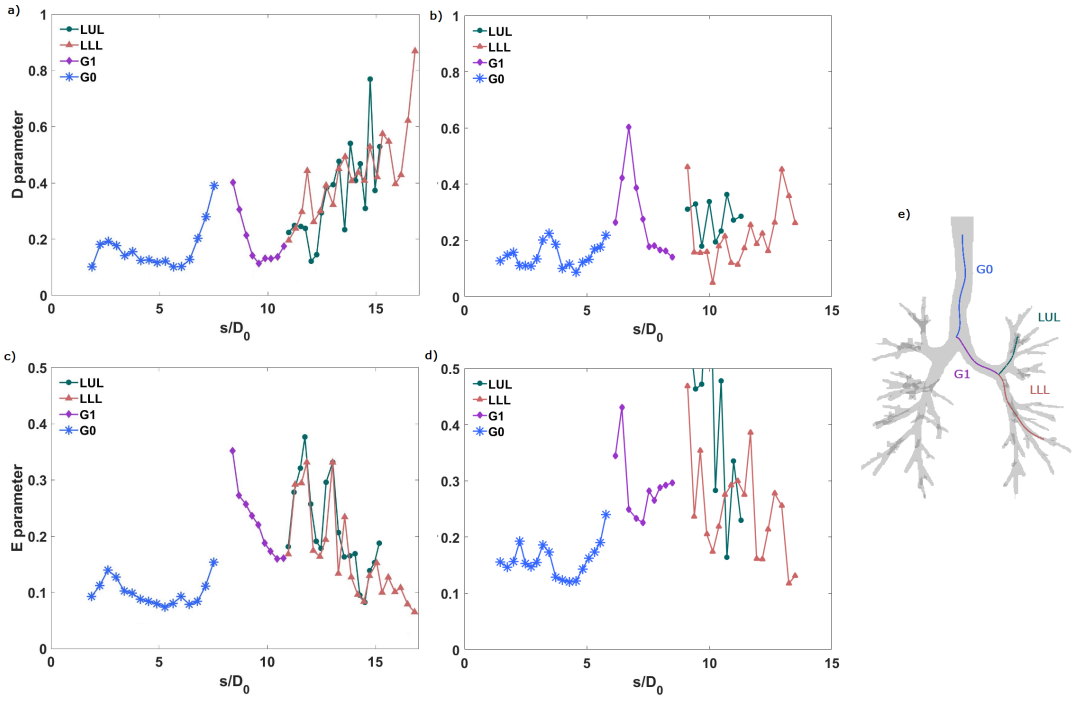

Figure 4.7: D **a), b)** & E **c), d)** parameters along sample path shown in **e)** for inhalation and exhalation

The generation-averaged plots, while capturing the ensemble picture, smear the strong local flow variations. To illustrate the latter, in **figure 4.7** we plot both D and E parameters along sample paths (**Fig. 4.7 (e)**) during steady inhalation (**Fig. 4.7 (a, c)**) and steady exhalation (**Fig. 4.7 (b, d)**). The normalized abscissa s/D_0 runs along the entire centerline, including the carinal region of the bifurcations. The notation Gi refers to the i-th branching generation (the main bronchi being the 1st generation). The selected paths in the LUL and LLL are representative of the behavior in the other lobes. Although the global behavior reflects what reported in Figs. 4.5 and 4.6, strong local variations are visible. The sharp peaks in D coincide with the carinal regions, where the streamwise flow is highly non-uniform. Concurrent peaks in E correspond to locally intense secondary motions, indicating that also the latter are enhanced at the carinas.

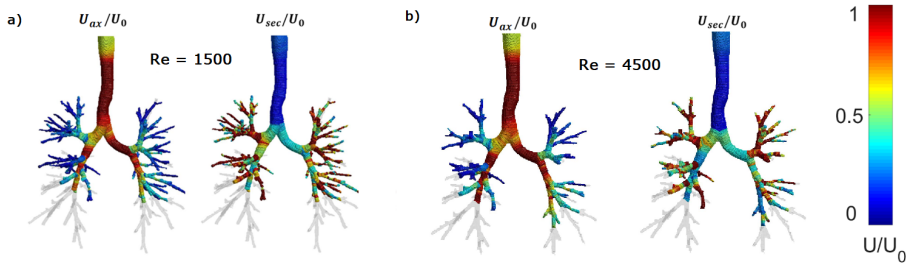

Figure 4.8: Normalized magnitude of axial and secondary velocity in the entire bronchial tree under steady inhalation for both Re = 1500 **a)** and Re = 4500 **a)**

Figure 4.8 a and b displays the normalized magnitude of axial and secondary velocity in the entire bronchial tree (down to the resolved generations) under steady inhalation for both Re = 1500 and Re = 4500 respectively. For illustration, the airway surface is color-coded by the magnitude of U_{ax}/U_0 and U_{sec}/U_0 at the corresponding cross-section. The resulting picture points again to a strong heterogeneity of both velocity components, beyond the trends indicated by generation-averaging. While the axial velocity globally decreases in further generations as expected, there are notable exceptions: regions of relatively fast flow deep in the lower lobes, and sudden velocity increases/decreases. In general, the distribution of axial velocity appears very heterogeneous. The spatial changes in secondary velocities are even more abrupt, with sharp differences along bronchial pathways and between sibling branches. The exhalation case shows qualitatively similar trends. Despite some local difference, the Re = 1500 and Re = 4500 cases appear overall similar, confirming that the steady inspiratory topology changes only slightly within the considered range of flow rates.

As it is important to understand and quantify the differences between idealized and patient specific models, we assess secondary velocities at the first bronchi (G_1) and compare them at the same generation against the Weibel model, for both steady inhalation and steady exhalation, at the same regime. **Figure 4.9** shows the averaged secondary flow velocities at G_1 normalized by U_0in both models and at both regimes where the red bars in the patient specific denote the range of variations between right and left bronchi. At inhalation, secondary flows in the patient specific model are somewhat higher (about 30%) with respect to the Weibel model. For exhalation, secondary motions are almost

twice as strong in the patient-specific model, indicating that geometry effects such as curvature, out-of-plane bifurcation, variability of branching angles do play a significant role in dictating the secondary flow behavior, and will undoubtedly influence respiratory fluid dynamics.

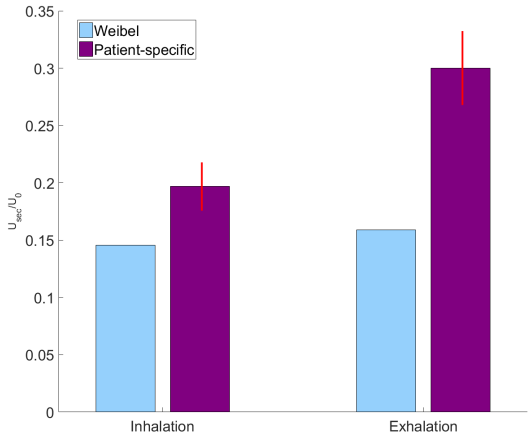

Figure 4.9: Averaged secondary flow velocities at G_1 normalized by U_0in patient-specific and Weibel models at steady inhalation and steady exhalation

4.4 Oscillatory regimes

4.4.1 Streamise velocity

We begin the study of the HFV regime by observing the distribution of the momentum within the bronchial tree during the various phases of the ventilation cycle. In **Figure 4.10** we plot iso-surfaces of Uax corresponding to 50% of the maximum axial velocity magnitude at each phase, with positive (red) and negative (blue) values associated to inhalation and exhalation, respectively. The fifteen panels correspond to the phases resolved in the phase-averaged MRV, one for each symbol plotted in **Fig. 4.2**. In the exhalation/inhalation and inhalation/exhalation transitions (phase 1 and 8, respectively), regions of both positive and negative velocities co-exist along the airway tree. Such counter-flow regions were documented in both idealized and realistic airway models (Heraty et al. 2008; Choi et al. 2010; Bauer et al. 2015; Jalal et al. 2018). At

the beginning of inhalation (phases 2 and 3), high-momentum fluid is found mostly in the trachea and the first two bronchial generations leading to the upper lobes. At peak inhalation and during its deceleration part (phases 5 to 7), the high-momentum region shifts towards the branches leading to the lower lobes. Similarly, at the beginning of exhalation, the high momentum regions are prevalently located in the branches leading to the upper lobes; while they are rather found in the lower lobes during the second part of exhalation. The asynchronous behavior of the branches leading to upper and lower lobes, which is specific to HFV, will be discussed in the next sub-section.

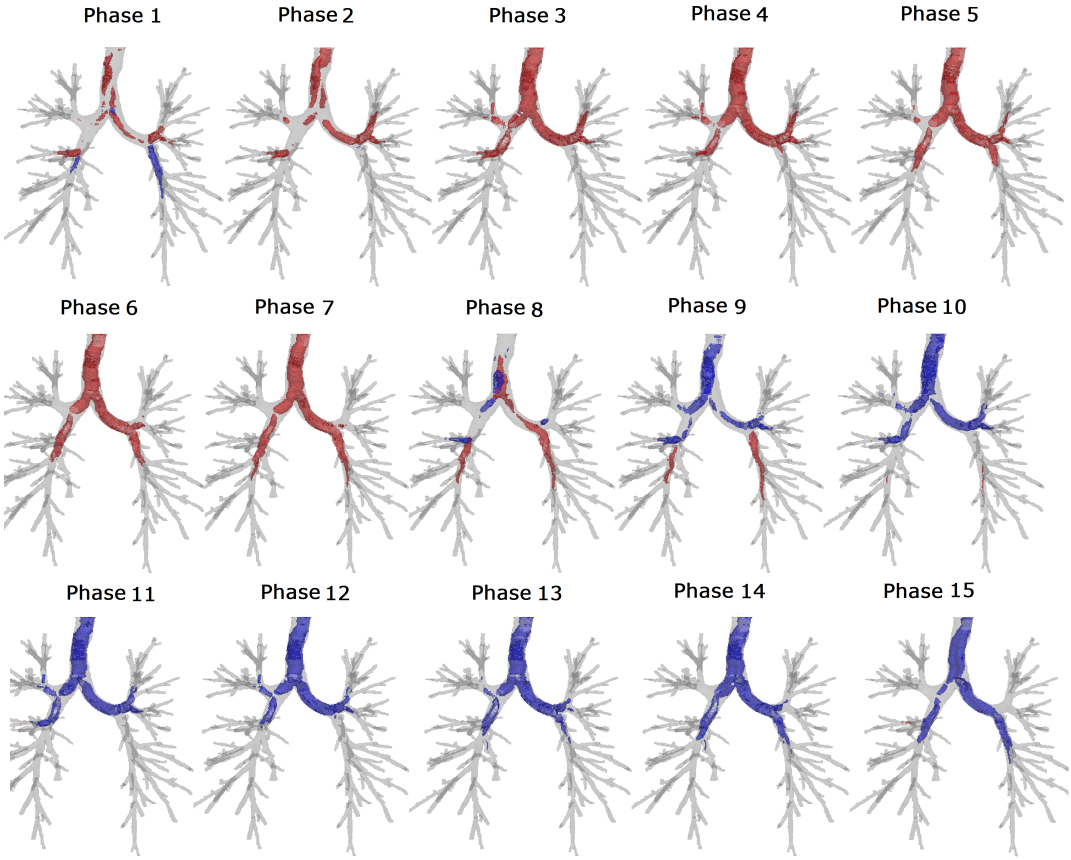

Figure 4.10: Velocity isosurfaces for successive phases of the inhalation and exhalation cycle at Wo=12. Red and blue colors indicate flow moving in the inspiratory and expiratory direction, respectively.

Figure 4.10 illustrates counter-flow regions at two locations along the trachea (**Fig**

4.10 (a)), during exhalation/inhalation (**Fig 4.10 (b, c)**) and inhalation/exhalation (**Fig 4.10 (d, e)**) transitions. In the straight part of trachea, the boundary layer along the airway perimeter shows the characteristic inversion of flow direction due to phase lag typical of high-Wo regimes (Womersley 1955). However, the non-canonical geometry breaks the anterior-posterior symmetry and prevents this feature from clearly appearing in both the transitions phases. Close to the carina, large pockets of reverse flow are observed along the lateral sides of the airway, adjacent to the main bifurcation (hence expansion of the cross-section and consequent acceleration/deceleration) where the flow experiences strong streamwise pressure gradients. These features are qualitatively similar to what observed in a symmetric Weibel model at similar Re and Wo (Jalal et al. 2018). We note that the specific flow topology is expected to be influenced by the upper airways, which are not included in the present model. The potential influence of those on the results is discussed in Section 4.4.2 of this chapter.

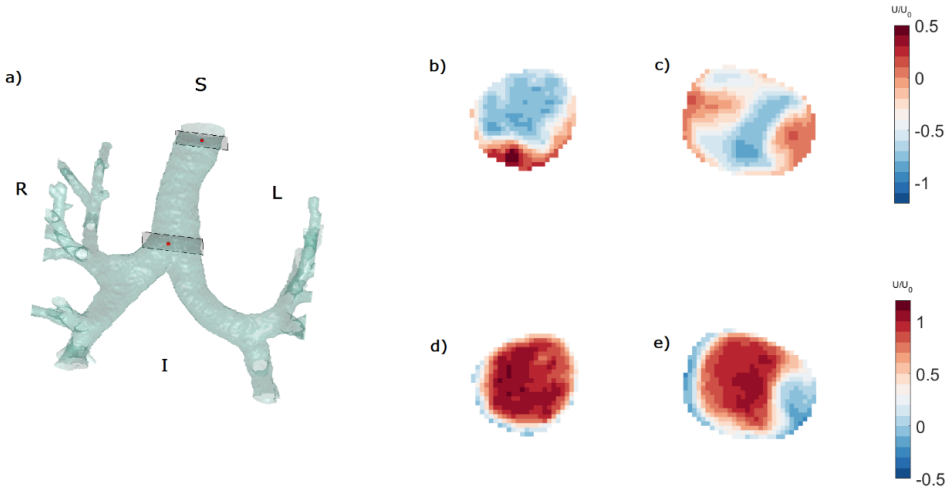

Figure 4.11: Cross-sections of normalized axial velocity at two locations shown in **a)** during exhalation/inhalation **b), c)** and inhalation/exhalation **d), e)**

4.4.2 Asynchronous flow and pendelluft

The asynchronous behavior of the branches leading to upper and lower lobes is due to unequal mechanical time constants between parallel lung units (Otis et al. 1956). At physiological breathing frequencies, the impedance offered by of a bronchial segment is mostly a combination of resistance and compliance. On the other hand, at higher breathing frequencies typical of HFV, the dominant factor becomes the different response of air mass in parallel regions of the lungs to rapid pressure changes (High et al. 1991, Greenblatt et al. 2014). Assuming sibling branches have similar diameter, such responsiveness (or inertance) is roughly proportional to the branch length. The upper lobes have visibly shorter branches, which results in lower inertance, hence lower impedance. When an oscillatory ventilation is applied to a bifurcation, the flow rate in the higher-impedance sibling branch will lag the inflow waveform in the parent airway, whereas the lower-impedance branch will anticipate it (Ultman et al. 1988). This is seen in **Fig. 4.10** and confirmed by **Fig. 4.12 (b)**, where we plot the axial velocity through a bifurcation splitting between LUL and LLL, normalized by U0.

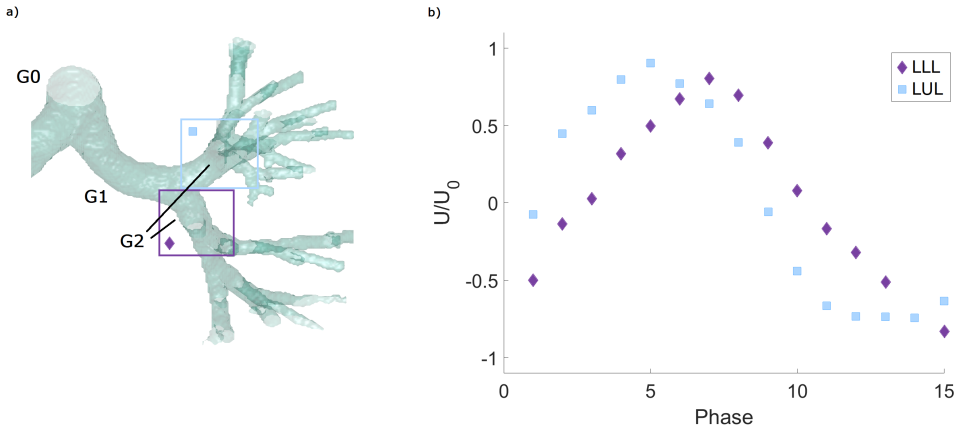

Figure 4.12: Normalized axial velocity at $G_2$for all phases **b)** at the LUL and LLL bifurcations shown in **a)**

A remark is in order concerning the realism of the present model, and the consequent relevance of the above observations to actual lung physiology. The rigid airway replica

cannot, by definition, account for the airway compliance. The latter, however, has decreasing impact on the impedance for increasing ventilation frequencies, and is expected to be inconsequential at the present Wo (Greenblatt et al. 2014). The resistance also plays a secondary role at this regime. In our model the resistance is largely determined by the valve setting downstream of the plena, which sets the boundary conditions at peak inhalation/exhalation to match the lobar partition at steady state. If the resistance was a main determinant, then the branches leading to the upper lobes (which receive low flow rate than the lower lobes, see **Tab. 1**) would be lagging. Instead, the opposite is observed. This confirms that inertance, which is well captured by our model reproducing the largest branches, dominates over resistance. In conclusion, the deficiencies of our model in capturing the compliance and resistance of a real human bronchial tree, while affecting the quantitative results, are unlikely to affect the main conclusions.

The asynchronous flow rate typical of HFV is often reported to cause transfer of mass between adjacent airway segments, also known as pendelluft (Otis et al. 1956, Greenblatt et al. 2014). While generally believed to be a crucial mechanism for gas exchange in HFV, pendelluft was rarely observed in simulations of realistic airway trees, and evidence from experimental measurements has been limited to idealized models (Drazen et al. 1984, Bauer et al. 2010, 2012, 2017, Alzahrany et al. 2014, Roth et al. 2018). The velocity fields in **Fig. 4.10** suggest that pendelluft is indeed happening around the exhalation/inhalation and exhalation/inhalation transition, with sibling branches simultaneously experiencing opposite flow directions. The specific locations are highlighted in **Fig. 4.13 (a,b)**, which however only demonstrate instantaneous flow patterns.

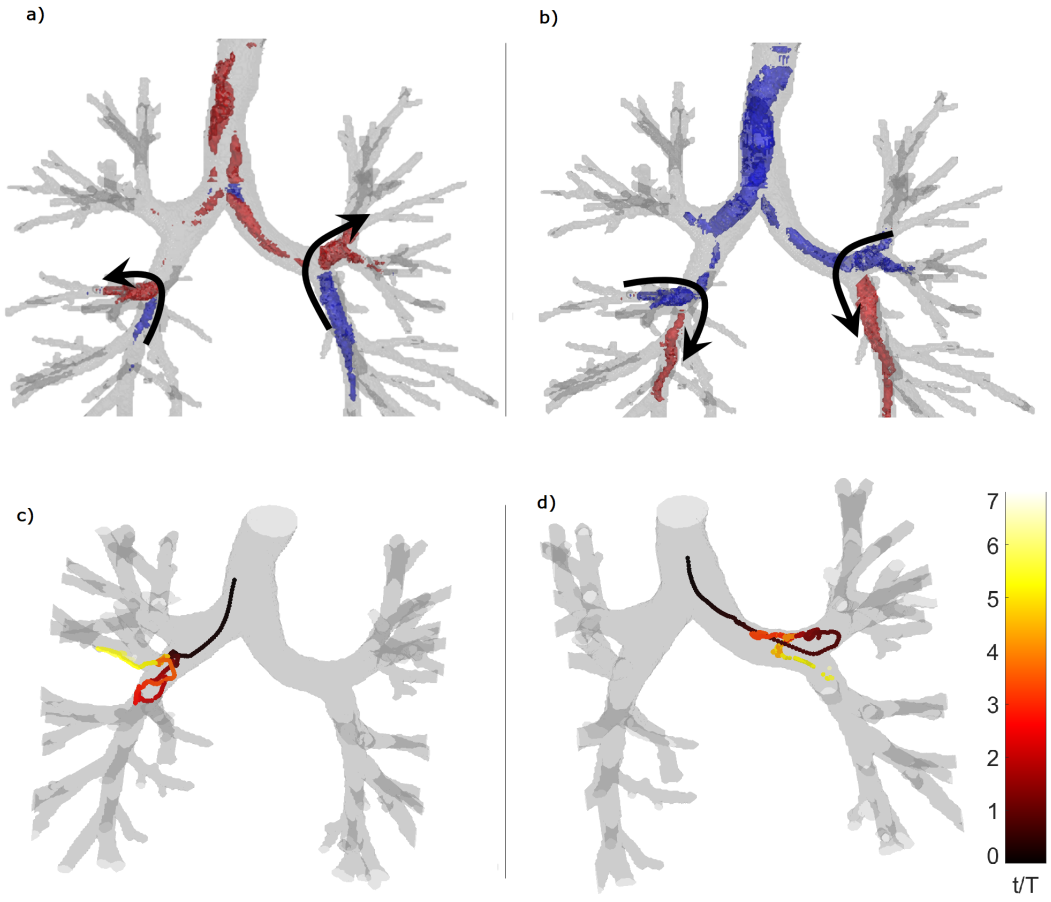

Figure 4.13: Asynchronous flow at the exhalation/inhalation transition **a)** and inhalation/exhalation transition **b) c), d)** sample Lagrangian trajectories color-coded according to the phase in the ventilation cycle

To verify whether fluid elements are actually transported between sibling branches, a Lagrangian analysis is needed. We therefore leverage the method developed and validated in Amili et al. (2019a, b) to track particles using 3D Eulerian velocity fields. In those studies, the focus was on inertial particles advected by a steady flow; here the approach is applied to mass-less particles (i.e., tracers) in a time-dependent flow.

The reduction from inertial to mass-less particles is trivial, while the extension to time-dependent flow requires a temporal interpolation between the phases. Linear interpolation is applied, which was verified not to produce significantly different results compared to higher-order schemes. The time step is chosen as 1/23 of the ventilation period, which corresponds to spatial integration steps smaller than 1/600 of the voxel size. For details on the methodology and validation against optical particle tracking, the reader is referred to Amili et al. (2019a, b). **Figure 4.13 (c, d)** show sample Lagrangian trajectories color-coded according to the phase in the ventilation cycle. The tracers are released from a 2-th generation branch at peak inhalation. After penetrating a daughter branch, some tracers do switch to the other sibling branch, providing the first direct observation of pendelluft in a realistic airway geometry. Similar paths (not shown) are observed at other locations. Quantifying the relative amount of exchanged fluid at multiple locations would require the integration of a large number of trajectories and is beyond the scope of the present work.

Secondary flows are crucial in the HFV regimes, as they are responsible for lateral dispersion and contribute to strong mixing (Fredberg 1980), especially in the transition phases where the streamwise bulk velocity is small. In **figure 4.14 (b)** we present the normalized secondary velocity U_{sec}/U_0 in the main bronchi (averaged over the branch length, **Fig 4.14 (a)**) during the ventilation cycle. Steady inhalation and steady exhalation levels are also indicated. Other branches in the first few generations show similar trends. We focus on the main bronchi as they allow for a direct comparison with measurements in a Weibel model (Jalal et al. 2018), for which we plot values measured at the 1st-generation bifurcation under similar conditions. During the inhalation phase, the secondary flows in both main bronchi are relatively constant and comparable in strength to the steady inspiratory case. During exhalation, the secondary flows quickly grows in intensity until they reach a maximum around peak exhalation for both right and left bronchi. The growth is associated to the streamwise vortices merging from the deeper airways into the main bronchi, as we shall discuss. The expiratory secondary flows during HFV reach levels about 50% higher than during inhalation, and comparable to the steady exhalation levels.

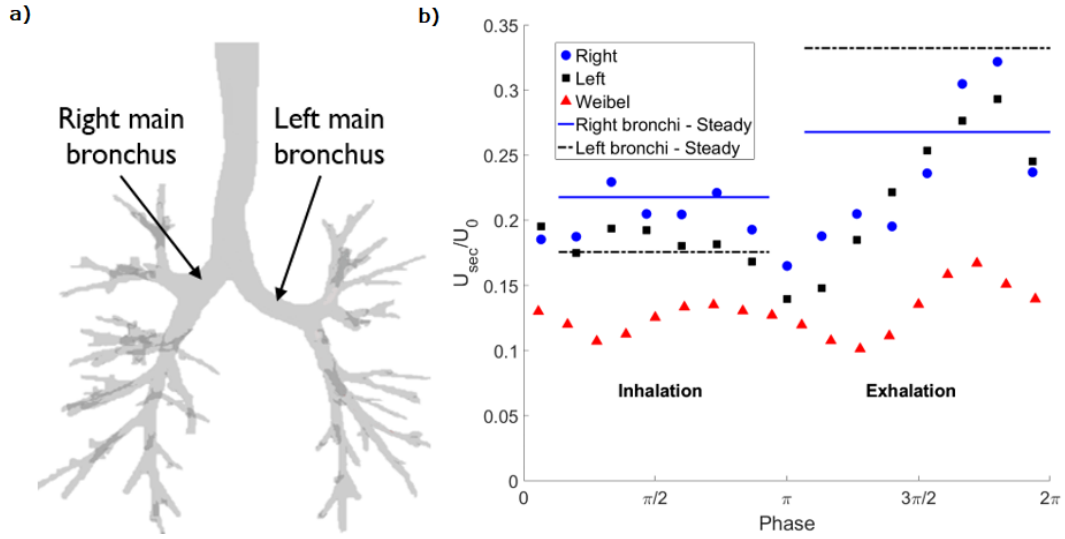

Figure 4.14: Normalized secondary flows averaged at the main bronchi **a)** for patient-specific and idealized airway model **a)**

Throughout the respiration cycle, the secondary flow levels are twice to three times stronger in the realistic model than in the Weibel model. This is consistent with the steady flow measurements (see Section 4.4.1) and is attributed to a combination of factors related to the airway tree structure. First, compared to the idealized model in Jalal et al. (2016, 2018), the realistic model has naturally curved airways that contribute to strengthening the Dean-type vortices. Second, the average opening angle between sibling branches, which is 60° in Jalal et al., is here larger. Van de Moortele et al. (2018) analyzed the airway morphometry of a cohort of subjects including the present one (with relatively small inter-subject variability), and found an opening angle of approximately 90° in the first three generations. Third, unlike the model of Jalal et al. (2016, 2018), the bronchial bifurcations show significant non-planarity (average rotation angle of 54°, see Van de Moortele et al. 2018). Comer et al. (2001) compared planar and non-planar idealized models and showed much stronger secondary flows in the latter. Fourth, and perhaps most importantly, the length-to-diameter ratio in the anatomically accurate model is significantly smaller than the canonical value of 3.5: Van de Moortele et al. (2018) reported values ranging from 1.5 to 3 in the first five generations. A small airway length contributes to secondary flows propagating across

successive generations, counteracting the dissipation of streamwise vortices (Jalal et al. 2016).

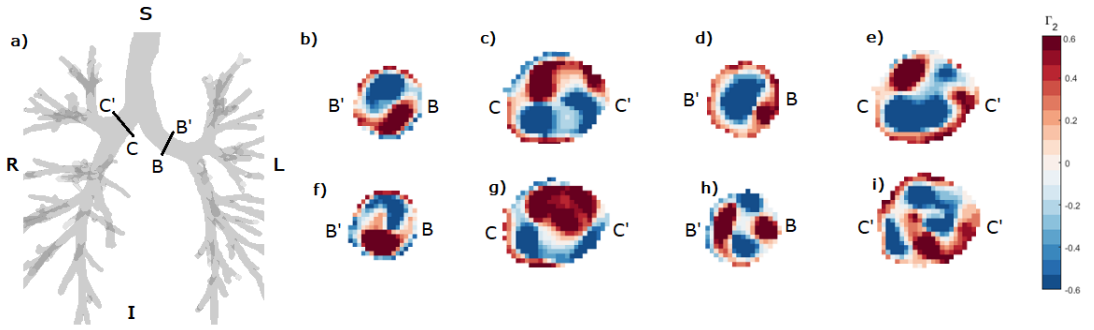

Figure 4.15: Cross-sections of $|Gamma_2$ levels at the main bronchi **a)** at peak inhalation **b), c)** and peak exhalation **d), e)** compared to steady inhalation **f), g)** and steady exhalation **h), i)**

Figure 4.15 illustrates the secondary flow structures along sample cross-sections in the main bronchi, at peak inhalation (**Fig. 4.15 (b, c)**) and peak exhalation (**Fig. 4.15 (d, e)**) compared to steady inhalation (**Fig. 4.15 (f, g)**) and exhalation (**Fig. 4.15 (h, i)**). To highlight the streamwise vortices, we use the vortex identifier Γ_2 (Graftieaux et al. 2001) as defined in **Equation X, Chapter 2**, which has the same sign as the local out-of-plane vorticity but is more effective at locating rotation-dominated over shear-dominated regions. At peak inhalation, the flow structure is overall similar to the steady inhalation case, in that the field is dominated by Dean-type vortices. At peak exhalation, on the other hand, the oscillatory case displays a simpler flow topology, with less numerous vortices in both bronchi. This is likely due to the fast ventilation frequency not allowing for the secondary flows to propagate as far through the branches. Therefore, while the U_{sec}/U_0 levels are comparable, the flow fields in HFV regime are significantly different from their steady counterparts.

4.4.3 Steady streaming

It has long been theorized that the asymmetry between the inspiratory and expiratory flow profiles, and the consequent net drift during each respiration cycle, contributes to the efficient gas exchange in HFV (Haselton & Scherer 1980; Chang 1984; Pillow 2005).

Yet this mechanism, often termed steady streaming, has rarely been documented beyond the mere observation of the asymmetry in the flow profiles (Roth et al. 2018). Peattie & Schwarz (1998) were the first to measure the streaming (or drift) velocity U_D, i.e., the cycle-average of the streamwise velocity, but they used point-wise velocimetry and could only report on a few linear profiles in a single idealized bifurcation. Bauer & Brucker (2015) performed numerical simulations in a more complex and realistic airway tree, and could map the full UD field. They found, however, minimal correlation between steady streaming and ventilation frequency. Jalal et al. (2018) measured the drift velocity in a planar Weibel model, and found its magnitude to be relatively weak and anti-correlated with the ventilation frequency. They explained this finding with the tendency of the flow profiles to be flatter (hence less asymmetric) with increasing Wo. Still, the highly idealized nature of that geometry may have influenced those quantitative results.

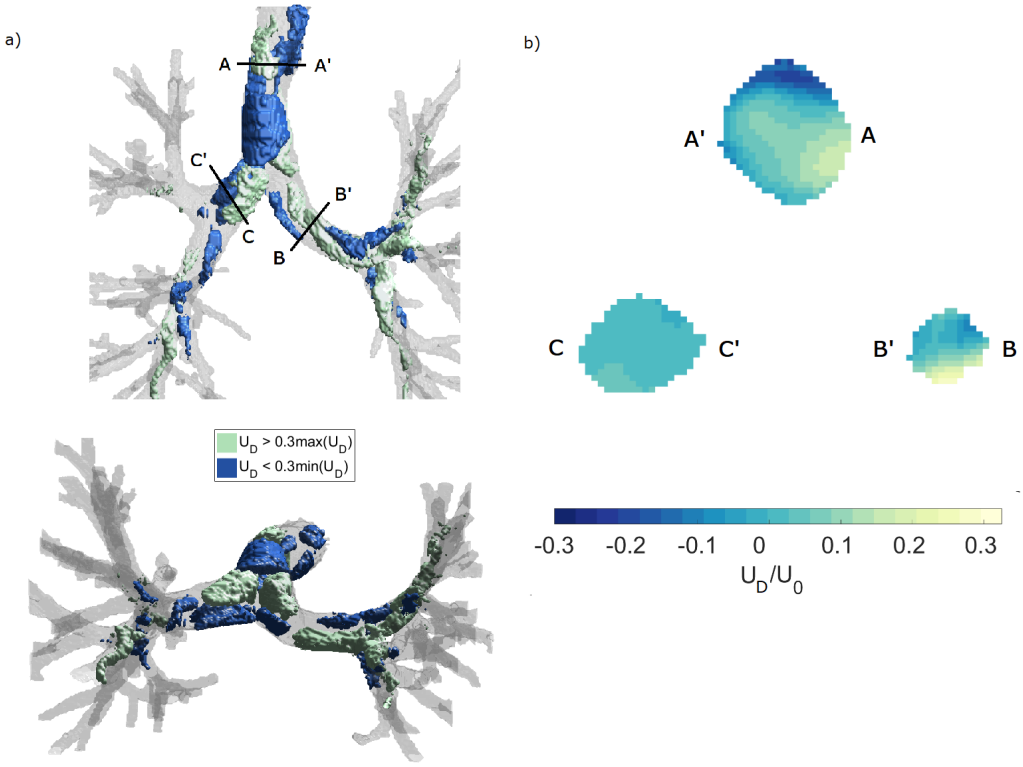

Figure 4.16: **a)** Iso-surfaces of positive/negative UD at 30% of the maximum velocity in the domain; **b)** contour plots along selected cross-sections at the trachea and the main bronchi

With the available 3D and phase-resolved velocity measurements, we carry out the first experimental evaluation of steady streaming in realistic airways. As in **Chapter 2**, we calculate the U_D volumetric field by cycle-averaging Uax at each spatial location. U_D is taken as positive (negative) when directed in inspiratory (expiratory) direction. **Figure 4.16** displays iso-surfaces of positive/negative U_D at 30% of the maximum velocity in the domain, as well as contour plots along selected cross-sections at the trachea and the main bronchi. Inspiratory drift is prevalent on the anterior side of the main bifurcation, whereas expiratory drift is found on its posterior side. The complex pattern in the main and secondary bifurcations challenges the common view of inspiratory/expiratory drift being located along the internal/external sides of bifurcations (Haselton & Scherer 1980; Chang 1984; Jalal et al. 2018). Clearly the realism and complexity of the tree

geometry heavily impacts the streaming flow topology.

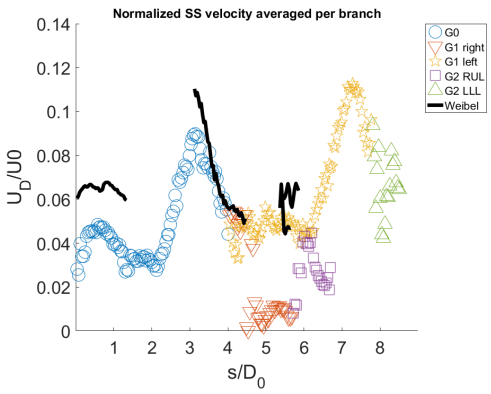

Figure 4.17: Magnitude of U_D versus the centerline abscissa, for two different pathways through both main bronchi(RUL & LUL) compared with the corresponding values at G_1 of the Weibel model.

In **Fig. 4.17** we plot the magnitude of U_D (i.e. the cross-section average of its absolute value) versus the centerline abscissa, for two different pathways through both main bronchi. For comparison, we also plot the corresponding values calculated with the data from Jalal et al. (2018) in their two-generation planar Weibel model at similar Re and Wo. Despite the above-mentioned topological differences, the amount of steady streaming and its streamwise evolution is comparable in both the realistic and idealized cases. An important consideration concerns the contribution of steady streaming to the overall transport. The bulk velocity in each branch is expected to be approximately $2h^2$ times smaller than in an earlier generation ($h \approx 0.8$ is the daughter-to-mother branch diameter ratio, Weibel 1963, Van de Moortele et al. 2018). Thus, we expect (and the measurements confirm) a bulk velocity at peak inhalation/exhalation around $U_0/(2h^2) \approx 0.8U_0$ in the first generation and $U_0/(4h^4) \approx 0.6U_0$ in the second generation. From the magnitude of U_D in **Fig. 4.17**, we conclude that the steady streaming flow under the present HFV conditions is much smaller than but not altogether negligible compared to the advective flow. Future studies shall clarify how (and whether) steady streaming is correlated with the ventilation frequency in similarly realistic airway trees.

Chapter 5

Steady inhalation investigated by Particle Image Velocimetry (PIV) in idealized model

5.1 Overview

While MRV provides us with 3-dimensional 3-component velocity fields, it remains a time-averaged methodology and as such lacks instantaneous flow information. While it is theoretically possible to measure Reynolds stresses using MRV, this is technically challenging and usually associated to substantial uncertainty (Elkins et al. 2009) and it is not attempted here. To complement our knowledge of fluid dynamics in bifurcations, we build a refractive-index matched Particle Image Velocimetry (PIV) facility to measure instantaneous 2-D velocity fields in 3D-printed models. Measuring instantaneous fields allows us to quantify unsteadiness embedded in the mean flow features, and associated Reynolds stresses.

Past studies have investigated flow in idealized airway models by PIV. Fresconi and Prasad (2007) measured secondary flows in a Weibel-type planar triple bifurcation using particle image velocimetry (PIV) along planes perpendicular to the main flow direction. They also matched the refractive index of their working fluid (a water-glycerol mixture) and the material of their model (elastomer) to explore steady inhalation and exhalation,

as well as in oscillatory regimes. Early experiments reviewed by Pedley (1977) as well as more recent PIV measurements of Theunissen and Riethmuller (2007) suggested unsteadiness and transition to turbulence already for Reynolds below 1000 (based on the local diameter) in bifurcating branches.

Using PIV in an idealized model, Heraty (2008) showed evidence of instability in the flow, in the form of high-frequency velocity uctuations. These uctuations vary from cycle to cycle, and do not appear in their phase-averaged velocity. Peattie and Schwarz (1998) also observed turbulent bursts in the parent branch of an idealized bifurcation at peak expiration. Grobe (2007) used PIV with water/glycerin mixture as a working fluid to match the index of refraction of their silicon, patient-specific lung model. Their setup allowed them to examine instabilities under steady and oscillatory flow conditions. In this chapter, we investigate the inspiratory flow at the symmetry plane of the Weibel bifurcation model over physiologically relevant Reynolds numbers. Instantaneous 2D velocity fields are obtained using PIV and ensemble-averaged to compared with the corresponding mean velocity data collected using MRV at G_0 and G_1. Moreover, we analyze the vorticity/shear distributions along with RMS fluctuations at the symmetry plane of the bifurcation. Finally, we investigate the unsteadiness of the flow and conduct a Proper Orthogonal Decomposition (POD) analysis to explore the details of the unsteadiness and their relationship to the nature of the structure (i.e. bifurcation effects) and inlet conditions effects on the flow downstream.

5.2 Methodology

Similar to the Weibel geometry used in **Chapter 2**, we investigate a planar, idealized double bifurcation model. The geometry is the same as in **figure 2.1 (a)**. This model was designed to fit in the reservoir shown in **Figure 5.1 (a)**. The bifurcation geometry is used to 3D print a model in Watershed XC 11122 with a wall thickness of about 1mm at the W. M. Keck Center (University of Texas El Paso, TX) to minimize optical distortions. The high-resolution print (25-m layer thickness) guarantees that the inner walls of the model are hydrodynamically smooth. The bifurcation model is attached to two 3D-printed pipes which connect to the rest of the rig as seen in **ure 5.1 (b)**. The upper tube is 219 mm long and includes 3 uniform grids at the inlet which help dissipate

flow disturbances caused by the valve. The lower tube is 250mm long and connects the upper pipe to the bifurcation model. The total length of 16 diameters helps provide a developed inlet conditions at the trachea. However, as we shall notice, this is still not sufficient to provide a fully developed inflow. The bifurcation model is enclosed in a reservoir with glass windows 6 mm thick allowing full optical access.

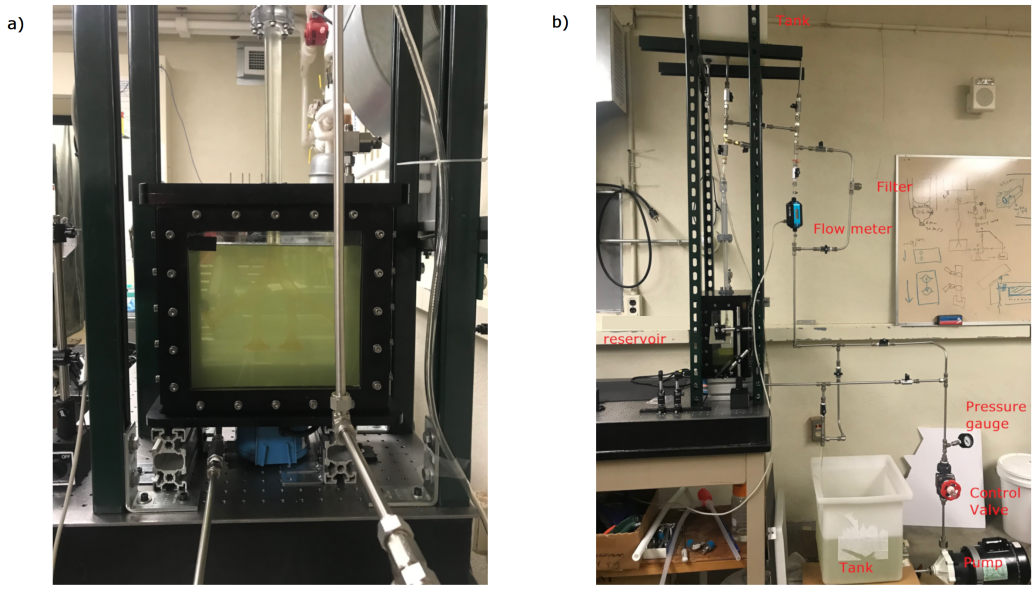

Figure 5.1: **a)** Picture of the reservoir with the model inside submerged in anise oil/mineral oil mixture connected to **b)** the rest of the setup

In order to match the index of refraction of Watershed XC 11122, we use as working fluid a combination of anise oil and mineral oil that matches the refractive index of WaterShed (n = 1.5131). In the past Butscher et al. (2012) obtained refractive-index-matched PIV measurements in a 3D printed model manufactured with WaterShed using anisole. However, anisole is expensive and deteriorates the material relatively quickly. For the same purpose, Hafeli et al. (2014) used a tunable and less aggressive mixture of NaI and ZnI2 , which however oxidizes and loses clarity in contact with air. The mixture of anise oil and mineral oil used here is not aggressive to WaterShed (although it can attack other plastics), is obtained with relatively inexpensive products, and does not oxidize when exposed to air. Using a 57%-43% mixture by volume of anise oil and mineral oil (CQ Concepts Inc.), the refractive index of Watershed is matched at 24C,

as measured by an optical refractometer and visually verified. The composition and properties of the mixture are reported in **Table 5.1**.

Composition by weight	Anise oil 57% - Mineral oil 43%
Density	950 Kg/m^3
Kinematic viscosity (at 24°C)	$2.5 \times 10^{-6} m^2/s$
Refractive index (at 24°C)	1.5131

Table 5.1: Working fluid parameters

The PIV setup was designed and built for three configurations: forced inhalation (**figure 5.2**), exhalation and gravity-driven inhalation (**figure 5.3**). In all configurations, the fluid is circulated in through stainless steel tubing using the 5-MD-SC LittleGiant pump. In series with the flow loop is the Atrato 760-V-1-0-SD ultrasonic flowmeter and in parallel with the flow loop is the stainless-steel tee-type Swagelok particulate filter with a 7-micron pore size. The flow was seeded with 10-micron glass beads particles as tracers and a pressure gauge is placed right after the control valve to monitor the overall pressure in the system.

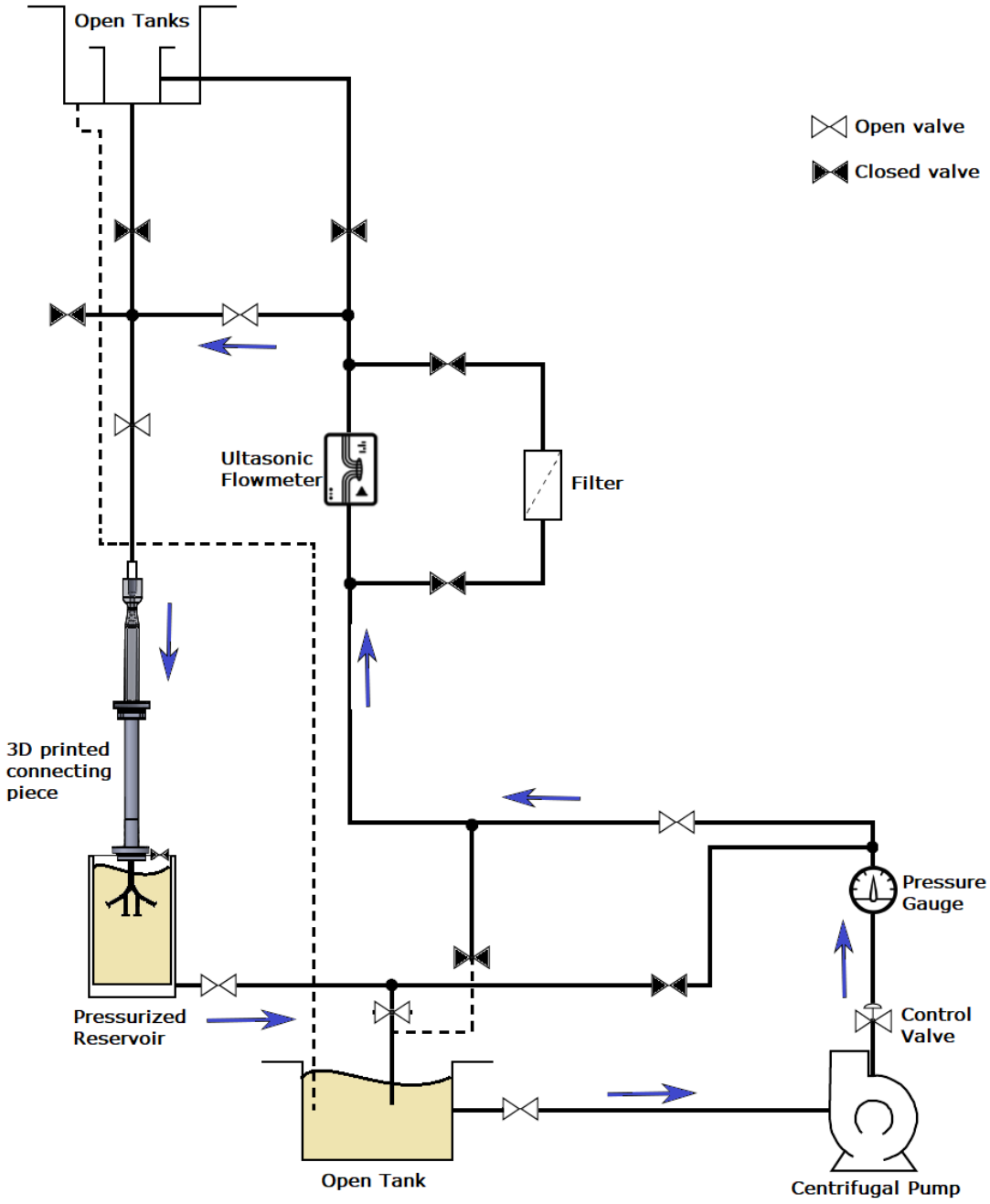

Figure 5.2: Schematic of the PIV setup in inhalation configuration

In the forced inhalation configuration, shown in **figure 5.2**, the flow is circulated by the pump. The fluid goes through G_0 and comes out through the outlet connected at the bottom of the reservoir, into the open tank. In the exhalation configuration (**figure 5.3, a**), the fluid is moved through G_2towards G_0 with the pump, then up the 3D printed connections and coming out into the open tank again. Finally, in the gravity-driven configuration (**figure 5.3, b**), the fluid is circulated through the outer loop of the setup, using gravity to get the fluid to the reservoir. In this case, using the pump, the small tank (tank 3) is filled until it starts to overflow onto tank 2. Then, valve A is opened allowing the fluid to flow down to the reservoir, while the pump is still pushing the flow to tank 3, making sure it is always overflowing. Any excess fluid in the outer tank (2) drains back to tank 1.

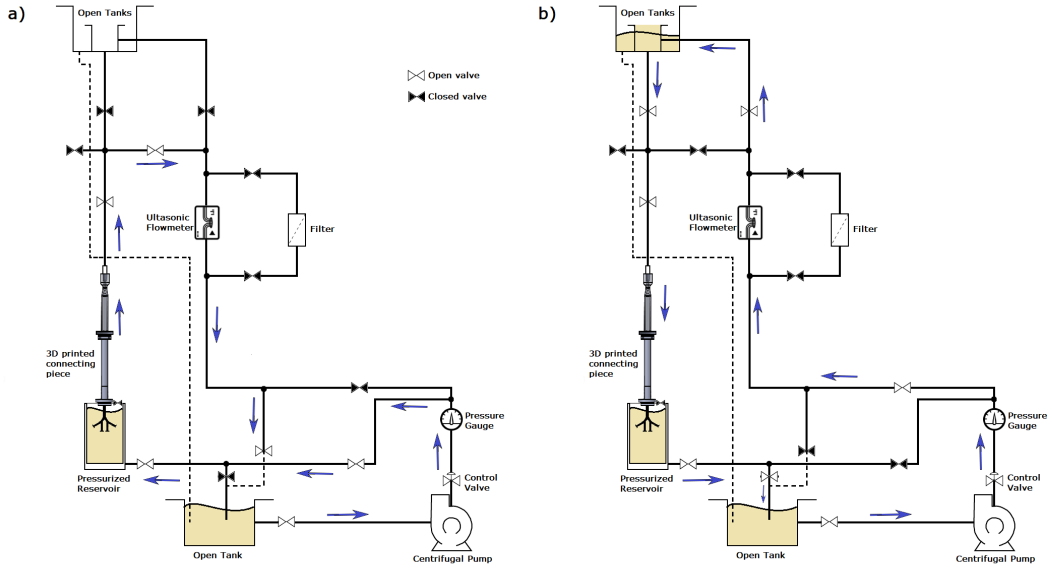

Figure 5.3: Schematic of the PIV setup in **a)** exhalation and **b)** gravity-driven configuration

In the current study, we focus on configuration 1 to explore steady inhalation in the double bifurcation airway model. **Figure 5.4 (a,b)** shows the rest of the setup, which includes a 2D LaVision PIV system composed of a CCD LaVision Imager camera (1 Megapixel) oriented perpendicular to the light sheet, a double-pulse Nd:YAG laser (532 nm of wavelength) with optics for laser-sheet generation, and pulse/delay generator to

synchronize illumination and image grabbing. The laser sheet was about 1-1.5mm thick for measurements at the symmetry plane. The refractive index is very well matched, with minimal distortion at the wall, as shown with a raw PIV image in **Figure 5.4 c**. Velocity vectors are computed using an in-house code (Nemes et al. 2015). A multi-grid interrogation was used, starting with 64-by-64-pixel = window, and then refining the grid to a 32-by-32-pixel window, with vector spacing at 75% overlap. 5000 image pairs were acquired for each case.

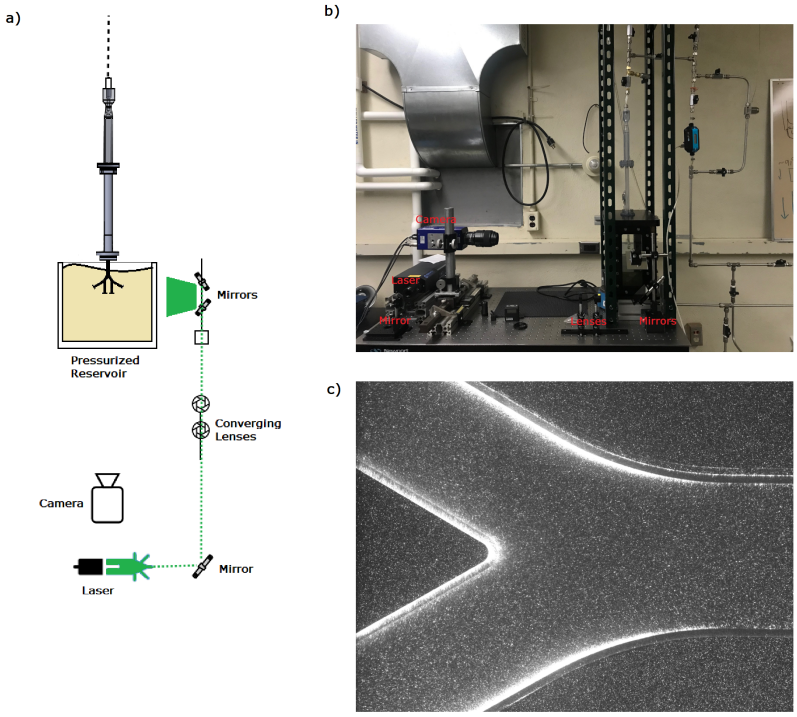

Figure 5.4: **a)** Schematic of the optics; **b)** a photo of the rest of the optics setup; **c)** an example of a raw PIV image

5.3 Velocity and vorticity comparison: PIV vs MRV

We first focus on a comparison of the streamwise velocity fields. **Figure 5.5** shows normalized streamwise velocity contours at the symmetry plane of the bifurcation model

between PIV and MRV during steady inhalation at $1000 \leq Re \leq 2000$. These PIV measurements are not at the same Reynolds number as the MRV, due to initial difficulties in setting up the flow rates and evaluating the fluid viscosity. More recent measurements at matching Re (shown below) indicate that the conclusions are not affected by the mismatch, especially considering that PIV is compared to MRV in a range that encompasses the PIV. The PIV velocity contours show qualitatively the same pattern as the MRV measurements, with high/low momentum along the inner/outer side of the bifurcation, and no measurable reverse flow.

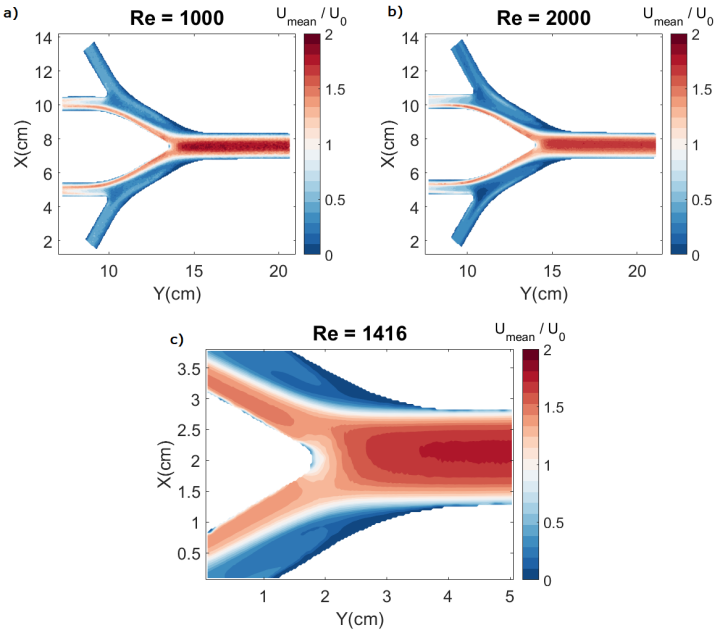

Figure 5.5: 2D streamwise velocity contours of **a)** Re = 1000 and **b)** Re = 2000 using MRV compared to **c)** velocity contours at Re = 1416 using PIV

Figure 5.6 (a) shows the 1D streamwise velocity profile along the bifurcation plane, about 2 D_0 above the carina. In MRV measurements, the profile is fairly symmetrical around the branch centerline. The velocity profile for Re = 2000 is slightly flatter than the one at Re = 1000 since the latter is closer to being to a fully developed laminar flow of parabolic profile. The PIV measurements, on the other hand, show a somewhat asymmetric and flatter profile. This suggests that valve upstream is producing

some perturbance that is not fully dissipated at this measurement station. **Figure 5.6 (b)** presents a similar comparison where the 1D profile is taken halfway through G_1. The PIV profile here is less pointy than both MRV profiles, implying that any disturbances stemming from the inlet conditions and the bifurcation itself carry on until the first generation. This is consistent with our conclusions from Chapter 2 stating that unsteadiness starts to play a role already in this regime, due to the geometry expansion, the curvature, and the impingement on the carina.

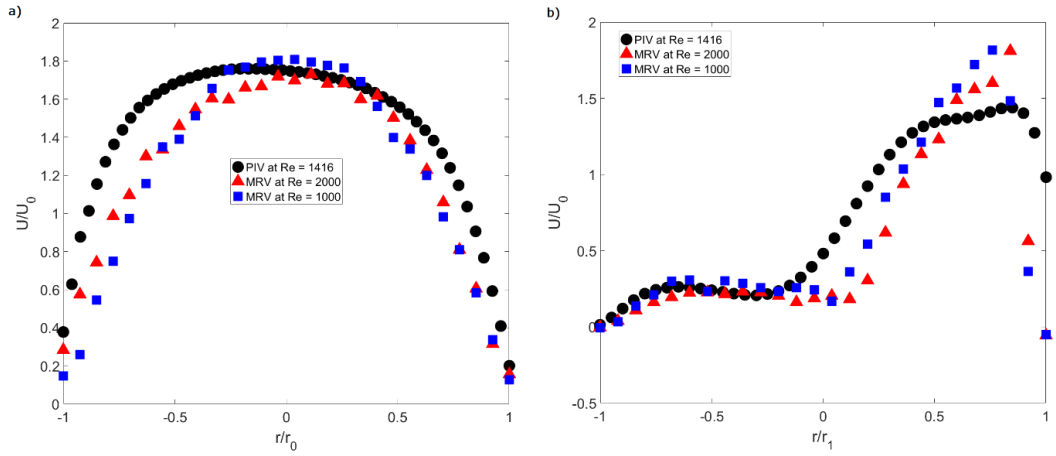

Figure 5.6: Streamwise velocity profiles along the bifurcation plane at G_0 **a)** and G_1 **b)** for MRV and PIV

To quantify the unsteadiness happening at this regime (Re = 1416), we look at the rms fluctuations of the velocity. **Figure 5.7** displays the rms fluctuations across normalized by U_0 the whole field of view, where regions near the wall at the trachea show increased levels of rms. Additionally, the flow separation (along with secondary flows induced by curvature effects) leads to regions of high shear stress which correlate with the high rms values.

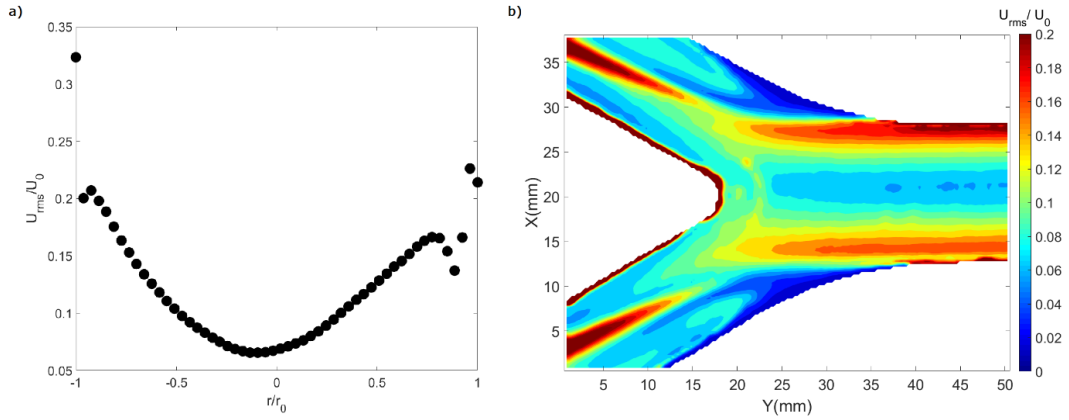

Figure 5.7: 2D contours of normalized RMS fluctuations of the streamwise velocity at Re = 1416, over the whole field of view across 5000 frames

Another noteworthy aspect is the strong shear occurring at G_1. **Figure 5.8** shows a comparison of the mean out-of-plane vorticity between PIV and MRV measurements during steady inhalation. In PIV measurements (**figure 5.8 c**), the shear is stronger in the middle of the branch where the velocity profile is skewed due to curvature effects and the contrast between high and low momentum regions is the strongest. However, in MRV, the shear layer region is even sharper and closer to the inner and outer walls of the bifurcation. The fact that, in the PIV case, the shear layer is more diffused through the branch diameter is likely a consequence of the strong unsteadiness, causing diffusion of momentum and smoothing of the mean velocity gradients. Taken together, these results indicate that the PIV case has non-negligible fluctuations in the inflow, and that those propagate through the bifurcation, affecting the momentum transport.

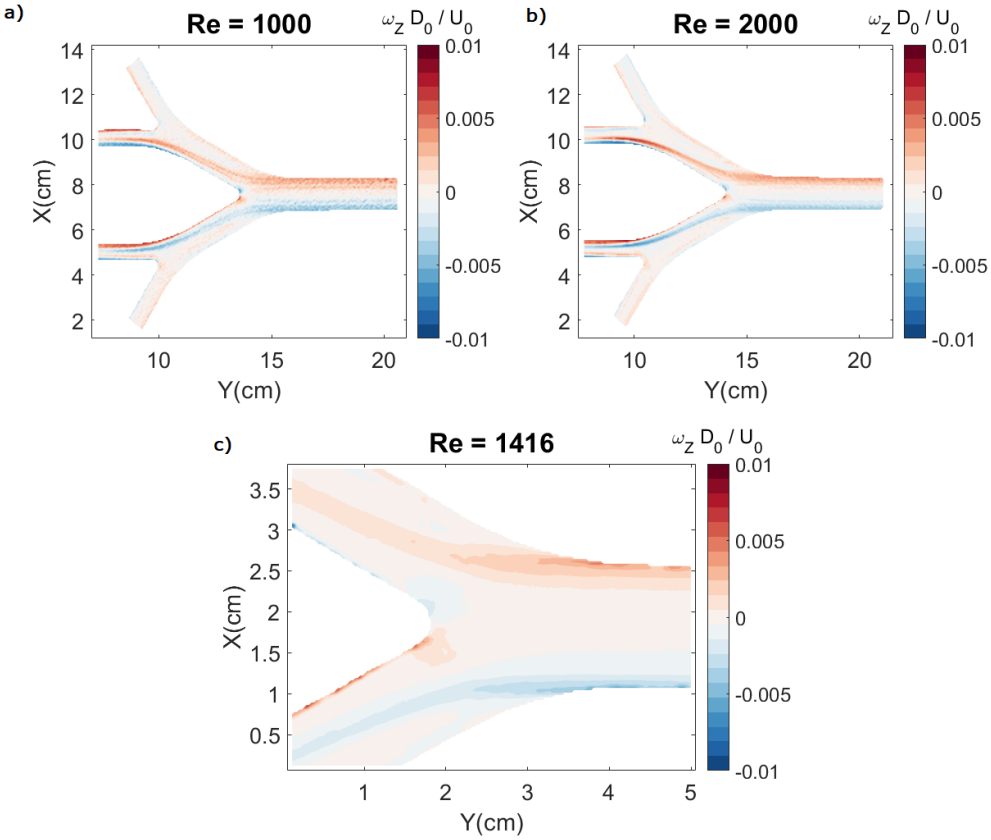

Figure 5.8: **a)** 2D out-of-plane vorticity contours at Re = 1000 and **b)** Re = 2000 using MRV compared to **c)** vorticity contours at Re = 1416 using PIV

To investigate the effects of inflow conditions, we also considered a scaled down version of the idealized double bifurcation model, with $D_0 = 8.55$mm, half of the original model, which is inserted in the PIV loop for instantaneous flow measurements. The mean flow features appear again similar between PIV and MRV, as expected (**figure 5.9 (a)** and **b**). The 269mm long inlet tube now allows for 32 diameters of developmental length compared to 16 previously and helps achieve a more developed flow at the trachea. The velocity profile for the PIV case displayed in **figure 5.9 (c)** is symmetrical compared to the PIV results in the larger model, but it is still flatter than the MRV case. This could be partly due to the Reynolds number being somewhat larger, and partly to upstream perturbations still not being dissipated. Overall, the inlet conditions

here allow for a fully developed inflow.

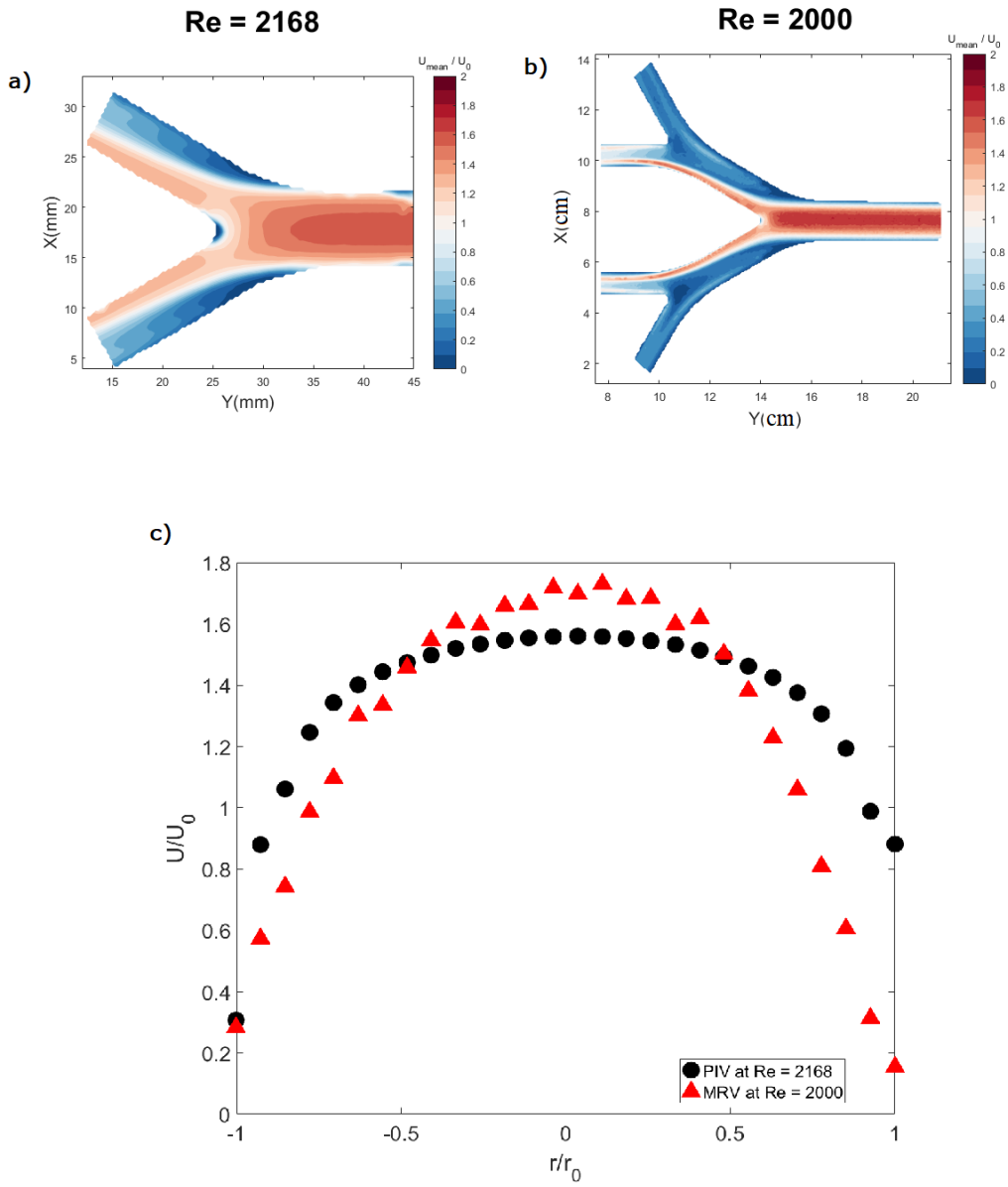

Figure 5.9: **a)** 2D streamwise velocity contours in the scaled-down model at Re = 2168 compared with **b)** velocity contours in the original model at Re = 2000 using MRV, **c)** Streamwise velocity profiles comparison along the bifurcation plane at G_0

5.4 Proper Orthogonal Decomposition (POD) analysis

While the mean flow features between the two PIV models are similar, the time-dependent behavior of the flow is different. Here we use Proper Orthogonal Decomposition (POD), a post-processing method to extract basis functions (Phi), i.e. spatial modes which provide an optimal basis for expansion of the flow, because they capture more energy than any other basis (Holmes et al., 1998). Here we apply POD to the streamwise velocity fluctuations in order to extract trends associated to the instantaneous flow field. **Figure 5.10** shows a comparison of the first and second modes between the regular and scaled-down bifurcation models. We only highlight the first two modes here since they are the ones that contribute the most to the fluctuating energy. Panels a and b highlight the first two modes in the scaled down bifurcation model, where there is a clear symmetrical contribution from both sides of the model and from both modes. However, in the original bifurcation model, there is an obvious asymmetry showing up through the first and second modes in panels c and d. The velocity profiles showed a level of flapping (i.e., momentum excess alternating between both sides of the bifurcation) which is picked up in the POD analysis of the original model.

Inspection of instantaneous flow fields confirm this flapping for this specific model and its associated inflow. However, the absence of flapping in the scaled-down (geometrically identical) model indicates instabilities in this geometry are extremely sensitive to the inflow conditions. This observation has actual physiological implications: in reality, the laryngeal jet causes strong perturbations in the trachea and the upper airways overall. Consequently, some flapping phenomenon is likely to happen and may affect the momentum transport in the conducting zone of the airways. Further investigations of this type in realistic airway geometries are warranted.

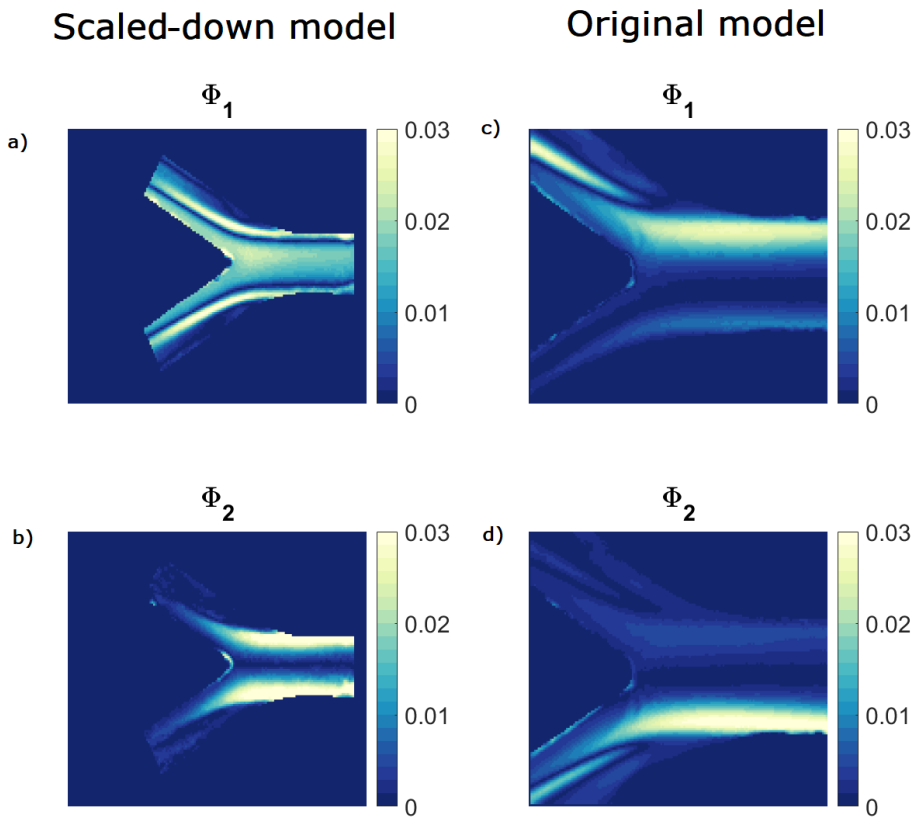

Figure 5.10: **a), b)** First and second POD modes in the scaled-down bifurcation model at Re = 2168 compared with **c), d)** first and second modes in the original bifurcation model at Re = 1416

Chapter 6

Conclusions & recommendations

6.1 Further discussion & summary

6.1.1 Weibel geometry

This study was aimed to develop a comprehensive understanding of respiratory fluid dynamics, a subfield that is critical to many aspects of our health, yet still lacking some fundamental knowledge of the mechanisms behind it. We first report on the three-dimensional flow in a symmetric double bifurcation airway model, focusing on steady inhalation and steady exhalation. Although highly idealized, the model follows the canonical proportions of the human bronchial tree, and indeed similar geometries have been studied extensively both experimentally and numerically. Nevertheless, because of the challenges posed by the highly three-dimensional flow, a comprehensive description across the range of physiologically relevant Reynolds numbers has been lacking. We perform 3D-3C measurements of the velocity field in the entire fluid volume using MRV, which provides a complete picture of the momentum and vorticity transport over a wide range of respiratory regimes.

During inhalation, and even at the lower Re, inertial forces cause the fluid to favor the internal side of the first bifurcation, and consequently the medial branches at the second bifurcation. This trend, however, reaches a plateau around Re = 2000. Beyond this regime, the transverse gradients of streamwise velocity become milder, as reflected in the values of the streamwise momentum flux (D parameter). Although Reynolds stresses

are not directly measured, the turbulent transport at Re = 3000 5000 is the prime candidate for causing the observed flattening of the mean velocity profiles, and indirectly the plateau in the asymmetric flow partition among medial and lateral G_2branches.The secondary motions in the bifurcation, related to the lateral dispersion in the airways, also depend greatly on the flow regime, both in magnitude and in topology. Dean-type counter-rotating vortices are formed in the first-generation daughter branches as a result of the local curvature.

In the granddaughter branches, the secondary flows are determined by the local curvature only for the lower flow regimes (Re = 100, 250), in which case the classic Dean mechanism dominates. At higher flow regimes, streamwise vortex pairs rotating in directions opposite to the Dean mechanism are observed in the medial granddaughter branches. These vortices are an extension of those in the upstream branches, and their strength also increases up to Re = 2000 and then declines. The flow in the lateral granddaughter branches is instead associated with weak secondary motions. The streamwise vortices meander considerably in the transverse direction, interacting both with each other and with the airway walls. For Re $>$ 500, they lose negligible circulation along each branch due to viscous diffusion. In fact, being fed by new vorticity injected at the first carina, the vortices can be stronger in the medial granddaughter than in the upstream daughter branches

Expanding on the steady inhalation results, we also focus on the steady expiratory flow for a range of Reynolds numbers, and the oscillatory flow for a range of Womersley numbers. In comparison with steady inspiration, we confirm that the expiratory flow exhibits atter velocity proles, which become progressively blunter in the flow direction. This is mainly due to the redistribution of momentum by the secondary motions, which are stronger in exhalation than in inhalation. The reason for this is twofold. First, at branch bifurcations (where a branch splits in two) the Dean mechanism typically induces two counter-rotation vortices, while at branch junctions (where two branches come together) four vortices are formed. Second, the positive gradient of bulk velocity during exhalation enhances streamwise vorticity, while the opposite occurs during inhalation. The Reynolds number effect on the expiratory flow topology is conceptually similar as in steady inhalation. At the lower Re, the local geometry primarily determines the flow features: the momentum distribution follows the symmetry of the junctions,

and the branch curvature dictates the secondary flow orientation according to the Dean mechanism. This is in keeping with previous experimental studies, that however focused only on relatively low Re (e.g., Fresconi and Prasad (2007), who investigated Re $\leq$ 350). At Re =1000 and higher, on the other hand, the mutual inuence of successive junctions is evident in both the axial and secondary velocities. In particular, the streamwise vortices generated at the G_1-G_2 junction have sufcient strength to reach G_0, and radically change the secondary flow pattern. This effect is analogous to the propagation of the inspiratory flow vortices generated at the G_0-G_1 bifurcation, which at Re =500 and above are strong enough to reach G_2. The determination of the Re level at which this change in topology occurs would require additional measurements, and the precise value will depend on the details of the geometry. We suggest that, in the steady cases, streamwise vortices propagate through successive generations depending on their circulation-based Reynolds number Γ/ν.

In order to evaluate the viability of transport models for biomedical settings, it is important to assess whether steady flow results can be extended to pulsatile conditions. We nd that, as long as Wo is in the normal ventilation range (Wo $\leq$ 6), the phase-averaged 3D flow topology during both inhalation and exhalation phases is similar to the corresponding steady case during most of the ventilation cycle. This is in agreement with previous studies that found steady-like flow structure despite the oscillatory nature of the boundary conditions (Bauer 2015, Adler 2007). On the other hand, at Wo levels typical of HFV (Wo=12), the flow structure changes signicantly: the acceleration part of both inhalation and exhalation carries the hallmarks of the previous flow inversion, with the high-momentum regions of the flow located close to the walls. Consequently, the secondary motions are also altered, in particular the pattern of counter-rotating streamwise vortices and their ability to propagate across successive generations. The phenomenon of counterflow is found to be prominent at Wo=6 and 12. Reverse flow pockets are evident during inhalation and inhalation-exhalation inversion, and to a lesser extent during the exhalation-inhalation inversion. Their spatiotemporal extent is smaller compared to what was reported in some previous studies which only addressed single bifurcations; this underscores the importance of considering multiple bifurcations to capture the mutual inuence of adjacent geometric features. The cases at Wo=1.2 and 3 did not show sizeable counterflow. The classication proposed by Jan et al., according to

which these two cases should have quasi-steady behavior, appears remarkably predictive in this regard.

In both oscillatory and steady conditions, the secondary velocity components are more intense in exhalation than in inhalation. Moreover, their magnitude during inhalation (exhalation) is lower (higher) than in the respective steady cases, with the low-Wo cases showing larger temporal variations during the cycle. Overall, for the considered geometry and Re, the secondary motions during inhalation (exhalation) become stronger (weaker) with increasing Wo. These trends may have important consequences for gas and particle transport, which are both heavily affected by secondary motions (Kleinstreuer, 2008). Finally, we have shown that steady streaming, which is often considered a critical mechanism for transport in HFV, is in fact hindered by the at velocity proles at high Wo. The drift velocity obtained by cycle averaging the axial velocity is reduced when the ventilation frequency is increased. Therefore, for the same duration of ventilation, HFV may augment the net transport by steady streaming owing to the large number of cycles per unit time, but not as dramatically as it is often assumed. Recent numerical studies (Bauer, 2015,2017) also point towards a limited role of steady streaming.

Parallel to MRV measurements, we also design and build a refractive-index matched PIV facility to measure instantaneous 2-D velocity fields in the idealized model. While the mean velocity profiles are similar to the ones taken with MRV, the rms fluctuations demonstrate that there is significant unsteadiness. This is consistent with our conclusions from Chapter 2 stating that unsteadiness starts to play a role already at Re = 1400 - 2000, which is often considered laminar in the respiratory fluid dynamics literature. In this regime, unsteadiness is caused by the geometry expansion, the curvature, and the impingement on the carina. Additionally, we compare PIV measurements for the Weibel model to a scaled down version of itself, in order to eliminate any discrepancies from inlet conditions. Through a POD analysis of the streamwise velocity fluctuations, we detect flapping (i.e., momentum excess alternating between both sides of the bifurcation) at the trachea in a larger-scale model, which however is not present in a scaled-down version featuring a longer inflow development length. The absence of flapping in the scaled-down model indicates that the inflow conditions are crucial in determining instabilities in this geometry. Since the laryngeal jet causes strong perturbations in the

trachea, this observation might have direct physiological implications.

6.1.2 Realistic model

Similar to the idealized model, and to ascertain whether such trends and mechanisms are general or rather specific to one type of configuration, we extend our study to a healthy patient-specific airway geometry, under steady inhalation (Re = 1500, 4500), steady exhalation (Re = 1370) and HFV (Re_{peak} = 2000, Wo = 12). During steady inhalation, the flow topology does not vary much with increasing Reynolds number. This is confirmed with the D parameter which shows similar trends between the two Reynolds numbers: D increases up to the third generation where the velocity profiles become pointier then declines/plateaus. During exhalation, velocity profiles are flatter due to the flow merging after each junction, such that the D parameter is overall lower and decreases along the flow path. This result is consistent with our conclusions from the idealized geometry. Furthermore, sizeable pockets of flow reversal are found in both steady inhalation and exhalation, although flow reversal is less prone to happen in the latter. Compared to the idealized cases, the shape, size and location of these pockets vary (Jalal et al 2018) significantly. While in this case they are located above the main bifurcation, in the Weibel model they are mostly found on the outer region of the bifurcation.

Using the E parameter to quantify secondary flows, we note that the trends between the two steady regimes are similar (although stronger during exhalation), such that E is higher in the first few generations, then plateaus deeper in the bronchial tree. A comparison with the idealized geometry at the same regimes confirms that a more realistic geometry does induce stronger secondary flows (two times higher). However, we note that instead of the expected four main vortices identified at the trachea in the Weibel model, we only detect two counter-rotating ones here, due to the differences in geometry and boundary conditions at the outlet of the five lobes. Here again, it is important to assess the phase-averaged 3D flow topology during the ventilation cycle, more specifically under HFV. While the distribution of the momentum within the airway tree and at peak phases follows the expected behavior, the co-existence of asynchronous flow pockets in the transition phases (inhalation/exhalation and exhalation/inhalation) is specific to ventilations under high frequencies. Flow reversal regions are also observed in the

Weibel geometry although at different locations (near the carina and at the outer walls of the bifurcation), but the complex nature of the patient-specific geometry affects their size, location and displacement along the bronchial tree. The asynchronous flow rate typical of HFV is often reported to cause transfer of mass between sibling branches and is also known as pendelluft (Otis et al. 1956, Greenblatt et al. 2014). This phenomenon occurs when two airway segments have different impedances, which in this case, are determined by compliance, resistance and inertance. Under HFV regimes, the inertance, roughly proportional to the branch length plays a larger role than the other two parameters (Greenblatt et al. 2014). Since the upper lobes have visibly shorter branches than the lower lobes, the upper lobes anticipate the peak of the cycle while the lower lobes lag behind, leading to the pendelluft effect in the transition phases. Secondary flows are also crucial for lateral dispersion under this ventilation regime. We note that expiratory secondary flows during HFV reach level 50% higher than during inhalation, and comparable to the steady exhalation case. Moreover, throughout the respiration cycle, secondary flow levels are twice to three times stronger in the realistic model than in the Weibel one. This implies that any realistic effects significantly influence the flow dynamics here, and ultimately affect transport mechanisms and particle deposition.

Finally, we were able to carry out the first experimental evaluation of steady streaming in patient-specific airways. The complex pattern observed here is quite different from the one found in the idealized bifurcation, such that inspiratory/expiratory drift is prevalent on the anterior/posterior side of the main bifurcation. While this is much stronger than in the idealized airway model, it remains much smaller than the advective flow, suggesting that it is not a dominant transport mechanism under the considered HFV regime.

6.2 Future work and recommendations

The present measurements contribute to a more complete description of respiratory flows over a wide range of regimes. However, they also warrant further research to deepen and clarify our understanding of factors that have emerged here as crucial. Using MRV, studies on geometries with three or more successive bifurcations are needed to assess general streamwise trends in terms of momentum flux and secondary flows

along the airway tree. The effect of geometrical features (e.g., local curvature, carinal shape, branching angle) can be varied in an idealized model to encompass a larger range of the structure-function relationship. Moreover, any correlations between steady streaming in similarly realistic airway trees but under various frequency ventilations need to be further researched. At high Re, the importance of turbulent dispersion (with respect to longitudinal and lateral dispersion by the mean flow) could be assessed by concentration measurements of a transported passive scalar. Borup et al, (2018) introduced the technique of Magnetic Resonance Particle concentration (MRP), which obtains 3D volume fraction measurements for a dispersed particulate phase in turbulent water flows and can provide new insight on turbulent dispersion.

State-of-the-art approaches (such as low-field MRI) are often insufficient because of the limited range of measurable velocities, which instead should be as large as possible to tackle physiological flows that vary from mm/s to m/s. One way to bypass this limitation is to use ultra-high ($>$ 3 Tesla) magnetic fields. This can provide us with higher accuracy and better resolution data that can be used to resolve finer flow details. This is especially crucial at the boundaries of the airway walls where there are high regions of shear and where this type of flow has strong 3D aspects (carinal region, flow separation, etc.).

Additionally, using the newly assembled 2D PIV setup, one can collect more thorough measurements of Reynolds stresses that would allow determination of how deep into the airway tree the flow remains turbulent. We can pinpoint more specifically the regime at which inertia takes over as the driving mechanism in vorticity transport, in both inhalation and exhalation. This analysis should also be extended from the idealized model to the realistic airway geometry and capture instantaneous flow features that cannot be detected by MRV. More realistic inlet conditions consistent with the laryngeal jet in the trachea should be explored, along with any resulting flapping or instabilities and their propagation down the airway tree.

Finally, and as part of an on-going collaboration with Professor Josue Sznitman at the Israel Institute of Technology (Technion), we had the opportunity, during a visit in Summer 2018, to use their Tomographic Particle Image Velocimetry (**figure 6.1 (a)**) setup, a technique that enables the instantaneous volumetric measurements of all velocity components (3D-3C).

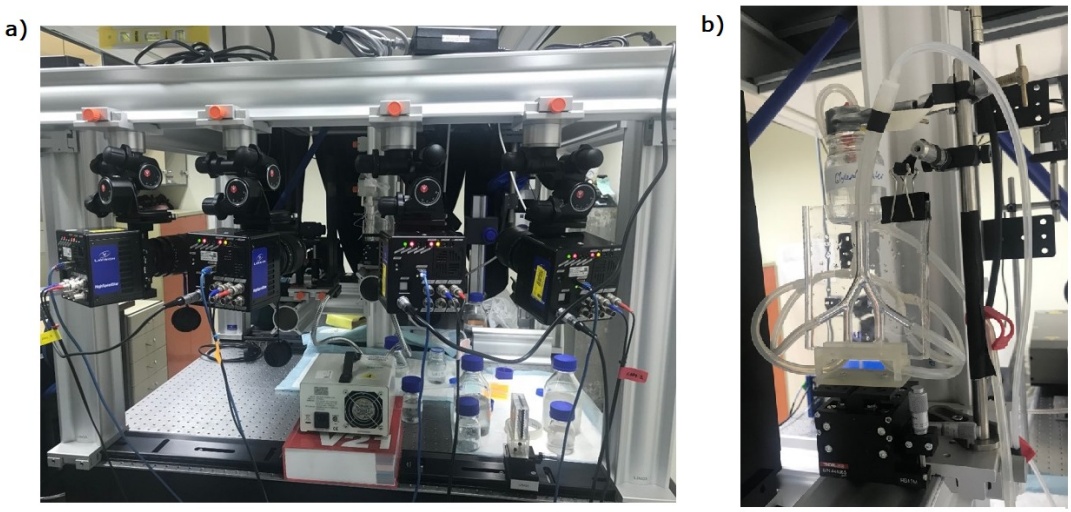

Figure 6.1: **a)** Tomo-PIV setup at Technion **b)** Silicon model of the Weibel geometry inserted in the Tomo-PIV setup

We started from the simple Weibel model (shown in figure b), which is of course easier to manufacture and image. A 3D printed a scaled down version of the Weibel model was used to make a silicone mold (**figure 6.1 (b)**). We used a glycerol-water mixture (58%, 42% by weight respectively) as a working fluid to match the refractive index of the silicone. A description of the rest of the setup is detailed in Bauer et al. (2017). We took data for steady inhalation at Re = 100 to compare and validate it against our MRV case at the same Re number. Preliminary results of Γ_2 isosurfaces are shown in (**figure 6.2**) with $\Gamma_2 = \pm 0.6$,, where the formation of Dean vortices at the first and second generation is present in both MRV and Tomo-PIV. Presently, our colleagues are working on collecting data under HFV for the case of Wo = 12 and peak Re = 100, a regime where we expect significant unsteady and convective forces and that spans velocities which are below the MRV noise floor. This regime is very relevant to the technique of HFV for neonates' lungs where the tidal volume is relatively low, but the ventilation frequency is high.

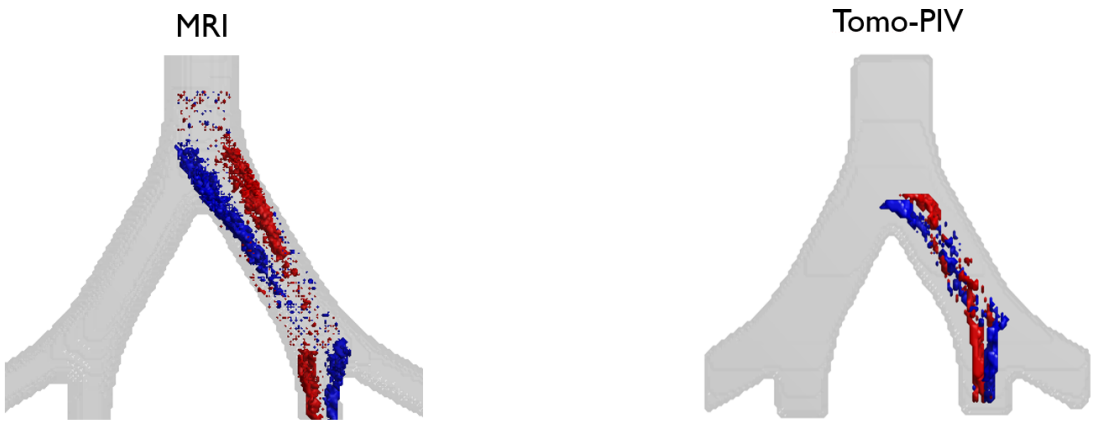

Figure 6.2: Isosurfaces of positive(red) and negative(blue) Γ_2 at ± 0.6 highlighting Dean vortices present in both MRV and tomo-PIV at Re = 100

References

Alzahrany, M., Banerjee, A., & Salzman, G. (2014). Flow transport and gas mixing during invasive high frequency oscillatory ventilation. Medical engineering & physics, 36(6), 647-658.

Amili O., Schiavazzi D., Moen S., Jagadeesan B., Van de Moortele P.F., Coletti F. (2018). Hemodynamics in a giant intracranial aneurysm characterized by in vitro 4D flow MRI. PLOS One, 13(1), e0188323.

Andrade Jr, J. S., Alencar, A. M., Almeida, M. P., Mendes Filho, J., Buldyrev, S. V., Zapperi, S., Suki, B. (1998). Asymmetric flow in symmetric branched structures. Physical review letters, 81(4), 926.

Banko, A. J., Coletti, F., Schiavazzi, D., Elkins, C. J., & Eaton, J. K. (2015). Three-dimensional inspiratory flow in the upper and central human airways.Experiments in Fluids, 56(6), 1-12.

Banko, A. J., et al. "Three-dimensional inspiratory flow in the upper and central human airways." Experiments in Fluids 56.6 (2015): 117.

Banko, Andrew J., et al. "Oscillatory flow in the human airways from the mouth through several bronchial generations." International Journal of Heat and Fluid Flow 61 (2016): 45-57.

Bauer, Katrin, Alexander Rudert, and Christoph Brcker. "Three-dimensional flow patterns in the upper human airways." Journal of biomechanical engineering 134.7 (2012): 071006.

Bauer, Katrin, and Christoph Brcker. "The influence of airway tree geometry and ventilation frequency on airflow distribution." Journal of biomechanical engineering 137.8 (2015): 081001.

Bauer, Katrin, Eliram Nof, and Josu Sznitman. "Revisiting high-frequency oscillatory ventilation in vitro and in silico in neonatal conductive airway." Clinical Biomechanics (2017).

Benson, M. J., Elkins, C. J., & Eaton, J. K. (2011). Measurements of 3D velocity and scalar field for a film-cooled airfoil trailing edge. Experiments in fluids, 51(2), 443-455.

Bernate, Jorge A., et al. "Study of the flow unsteadiness in the human airway using large eddy simulation." Physical Review Fluids 2.8 (2017): 083101.

Bulusu, K. V., Hussain, S., & Plesniak, M. W. (2014). Determination of secondary flow morphologies by wavelet analysis in a curved artery model with physiological inflow. Experiments in Fluids, 55(11), 1-20

Caro, C., Pedley, T., & Seed, W. A. (1974). Cardiovascular physiology.Mechanics of Circulation.

Chang, H. K. (1984). Mechanisms of gas transport during ventilation by high-frequency oscillation. Journal of Applied Physiology, 56(3), 553-563.

Choi J, Tawhai M, Hoffman E, Lin C (2009) On intra-and intersubject variabilities of airflow in the human lungs. Phys Fluids 21(101):901

Choi, Jiwoong, et al. "Numerical study of high-frequency oscillatory air flow and convective mixing in a CT-based human airway model." Annals of biomedical engineering 38.12 (2010): 3550-3571.

Coletti, F., Elkins, C. J., & Eaton, J. K. (2013). An inclined jet in crossflow under the effect of streamwise pressure gradients. Experiments in fluids, 54(9), 1-16.

Comer, J. K., Kleinstreuer, C., & Zhang, Z. (2001). Flow structures and particle deposition patterns in double-bifurcation airway models. Part 1. Air flow fields. Journal of Fluid Mechanics, 435, 25-54.

De Vasconcelos, T. F., Sapoval, B., Andrade Jr, J. S., Grotberg, J. B., Hu, Y., & Filoche, M. (2011). Particle capture into the lung made simple. Journal of applied physiology, 110(6), 1664-1673.

Dean, W. R. (1927). Note on the motion of fluid in a curved pipe. The London, Edinburgh, and Dublin Philosophical Magazine and Journal of Science, 4(20), 208-223.

Discetti, Stefano, and Filippo Coletti. "Volumetric velocimetry for fluid flows." Measurement Science and Technology (2018).

Doorly, D. & Sherwin, S. (2010). Geometry and Flow. In: Formaggia, L., Quarteroni, A., & Veneziani, A. (Eds.). Cardiovascular Mathematics: Modeling and simulation of the circulatory system. Springer Science & Business Media.

Drazen, J. M., Kamm, R. D., & Slutsky, A. S. (1984). High-frequency ventilation. Physiological Reviews, 64(2), 505-543.

Elkins, C. J., & Alley, M. T. (2007). Magnetic resonance velocimetry: applications of magnetic resonance imaging in the measurement of fluid motion. Experiments in Fluids, 43(6), 823-858.

Fredberg, J. J. (1980). Augmented diffusion in the airways can support pulmonary gas exchange. Journal of Applied Physiology, 49(2), 232-238.

Fresconi, F. E., & Prasad, A. K. (2007). Secondary velocity fields in the conducting airways of the human lung. Journal of biomechanical engineering,129(5), 722-732. Glycerine Producers' Association. (1963). Physical properties of glycerine and its solutions. Glycerine Producers' Association.

Golshahi, L., & Finlay, W. H. (2009). Recent advances in understanding gas and aerosol transport in the lungs: application to predictions of regional deposition. In Advances in Transport Phenomena (pp. 1-30). Springer Berlin Heidelberg.

Graftieaux, L., Michard, M., & Grosjean, N. (2001). Combining PIV, POD and vortex identification algorithms for the study of unsteady turbulent swirling flows. Measurement Science and Technology, 12(9), 1422.

Grotberg, J. B. (2001). Respiratory fluid mechanics and transport processes.Annual review of biomedical engineering, 3(1), 421-457.

Guha, Abhijit, Kaustav Pradhan, and Prodosh Kumar Halder. "Finding order in complexity: A study of the fluid dynamics in a three-dimensional branching network." Physics of Fluids 28.12 (2016): 123602.

Haselton, F. R., & Scherer, P. W. (1980). Bronchial bifurcations and respiratory mass transport. Science, 208(4439), 69-71.

Heraty, Kevin B., John G. Laffey, and Nathan J. Quinlan. "Fluid dynamics of gas exchange in high-frequency oscillatory ventilation: in vitro investigations in idealized and anatomically realistic airway bifurcation models." Annals of biomedical engineering 36.11 (2008): 1856.

Hoogenraad, F. G., Hofman, M. B., Pouwels, P. J., Reichenbach, J. R., Rombouts,

S. A. R. B., & Haacke, E. M. (1999). Sub-millimeter fMRI at 1.5 Tesla: correlation of high resolution with low resolution measurements. Journal of Magnetic Resonance Imaging, 9, 475-482.

Horsfield, Keith, and Gordon Cumming. "Morphology of the bronchial tree in man." Journal of applied physiology 24.3 (1968): 373-383.

Huang, Y., & Green, M. A. (2015). Detection and tracking of vortex phenomena using Lagrangian coherent structures. Experiments in Fluids, 56(7), 1-12.

Imai, Y., Nakagawa, S., Ito, Y., Kawano, T., Slutsky, A. S., & Miyasaka, K. (2001). Comparison of lung protection strategies using conventional and high-frequency oscillatory ventilation. Journal of Applied Physiology, 91(4), 1836-1844.

Isabey, D., & Chang, H. K. (1982). A model study of flow dynamics in human central airways. Part II: Secondary flow velocities. Respiration physiology,49(1), 97-113.

Jalal, S., Nemes, A., Van de Moortele, T., Schmitter, S., & Coletti, F. (2016). Three-dimensional inspiratory flow in a double bifurcation airway model. Experiments in Fluids, 57(9), 148.

Jalal, S., Van de Moortele, T., Nemes, A., Amili, O., & Coletti, F. (2018). Three-dimensional steady and oscillatory flow in a double bifurcation airway model. Physical Review Fluids, 3(10), 103101.

Jan, D. L., A. H. Shapiro, and R. D. Kamm. "Some features of oscillatory flow in a model bifurcation." Journal of Applied Physiology 67.1 (1989): 147-159.

Janke, Thomas, Rdiger Schwarze, and Katrin Bauer. "Measuring three-dimensional flow structures in the conductive airways using 3D-PTV." Experiments in Fluids 58.10 (2017): 133.

Kleinstreuer, C., & Feng, Y. (2013). Computational analysis of non-spherical particle transport and deposition in shear flow with application to lung aerosol dynamicsA review. Journal of biomechanical engineering, 135(2), 021008.

Kleinstreuer, C., & Zhang, Z. (2010). Airflow and particle transport in the human respiratory system. Annual Review of Fluid Mechanics, 42, 301-334.

Kleinstreuer, C., Zhang, Z., & Donohue, J. F. (2008). Targeted drug-aerosol delivery in the human respiratory system. Annu. Rev. Biomed. Eng., 10, 195-220.

Leong, F. Y., Smith, K. A., & Wang, C. H. (2009). Secondary flow behavior in a double bifurcation. Physics of Fluids (1994-present), 21(4), 043601.

Lin, C. L., Tawhai, M. H., McLennan, G., & Hoffman, E. A. (2007). Characteristics of the turbulent laryngeal jet and its effect on airflow in the human intra-thoracic airways. Respiratory physiology & neurobiology, 157(2), 295-309.

Liu Y, So RMC, Zhang CH (2002) Modeling the bifurcating flow in a human lung airway. J Biomech 35(4):465473

Liu, Y., So, R. M. C., & Zhang, C. H. (2002). Modeling the bifurcating flow in a human lung airway. Journal of biomechanics, 35(4), 465-473.

Longest, P. W., & Vinchurkar, S. (2007). Validating CFD predictions of respiratory aerosol deposition: effects of upstream transition and turbulence. Journal of biomechanics, 40(2), 305-316.

Markl, M., Frydrychowicz, A., Kozerke, S., Hope, M., & Wieben, O. (2012). 4D flow MRI. Journal of Magnetic Resonance Imaging, 36(5), 1015-1036. Mauroy, B., Filoche, M., Andrade Jr, J. S., & Sapoval, B. (2003). Interplay between geometry and flow distribution in an airway tree. Physical review letters, 90(14), 148101.

Mauroy, B., Filoche, M., Weibel, E. R., & Sapoval, B. (2004). An optimal bronchial tree may be dangerous. Nature, 427(6975), 633-636.

Miyawaki, Shinjiro, et al. "Effect of carrier gas properties on aerosol distribution in a CT-based human airway numerical model." Annals of biomedical engineering 40.7 (2012): 1495-1507.

Murray, C. D. (1926). The physiological principle of minimum work I. The vascular system and the cost of blood volume. Proceedings of the National Academy of Sciences, 12(3), 207-214.

Nicolaou, L., & Zaki, T. A. (2013). Direct numerical simulations of flow in realistic mouththroat geometries. Journal of Aerosol Science, 57, 71-87.

Oakes, J. M., Roth, S. C., & Shadden, S. C. (2017). Airflow Simulations in Infant, Child, and Adult Pulmonary Conducting Airways. Annals of biomedical engineering, 1-15.

Padilla A (2012) The effect of upstream perturbations on 3D annular diffusers. PhD thesis, Stanford University

Peattie, R. A., and W. Schwarz. "Experimental investigation of oscillatory flow through a symmetrically bifurcating tube." Journal of biomechanical engineering 120.5 (1998): 584-593.

Pedley, T. J. (1977). Pulmonary fluid dynamics. Annual Review of Fluid Mechanics, 9(1), 229-274.

Pedley, T. J., Schroter, R. C., & Sudlow, M. F. (1971). Flow and pressure drop in systems of repeatedly branching tubes. Journal of Fluid Mechanics, 46(02), 365-383.

Pedley, T. J., Schroter, R. C., & Sudlow, M. F. (1971). Flow and pressure drop in systems of repeatedly branching tubes. Journal of Fluid Mechanics, 46(02), 365-383.

Pelc, N. J., Sommer, F. G., Li, K. C., Brosnan, T. J., Herfkens, R. J., & Enzmann, D. R. (1994). Quantitative magnetic resonance flow imaging.Magnetic resonance quarterly, 10(3), 125-147.

Pillow, J. J. (2005). High-frequency oscillatory ventilation: mechanisms of gas exchange and lung mechanics. Critical care medicine, 33(3), S135-S141.

Pope, S. B. (1962). Turbulent flows. 2000. Search PubMed, 754.

Sapoval, B., & Filoche, M. (2013). Magic trees in mammalians respiration or when evolution selected clever physical systems. Fractals, 21(03n04), 1350024.

Scherer, P. W., & Haselton, F. R. (1982). Convective exchange in oscillatory flow through bronchial-tree models. Journal of Applied Physiology, 53(4), 1023-1033.

Schroter, R. C., & Sudlow, M. F. (1969). Flow patterns in models of the human bronchial airways. Respiration physiology, 7(3), 341-355.

Soodt, Thomas, et al. "Analysis of basic flow regimes in a human airway model by stereo-scanning PIV." Experiments in fluids54.6 (2013): 1562.

Sznitman, J. (2013). Respiratory microflows in the pulmonary acinus. Journal of biomechanics, 46(2), 284-298.

Theunissen, R., & Riethmuller, M. L. (2007). Particle image velocimetry in lung bifurcation models. In Particle Image Velocimetry (pp. 73-101). Springer Berlin Heidelberg.

Van de Moortele, Tristan, Christine H. Wendt, and Filippo Coletti. "Morphological and functional properties of the conducting human airways investigated by in vivo CT and in vitro MRI." Journal of Applied Physiology (2017): jap-00490.

Wall WA & Rabczuk T. (2008). Fluid-structure interaction in lower airways of CT-based lung geometries. Int. J. Numer. Methods Fluids 57:65375

Weibel, E. R. (1963). Principles and methods for the morphometric study of the lung and other organs. Laboratory investigation; a journal of technical methods and

pathology, 12, 131.

Weibel, E. R. (1997). Design of airways and blood vessels considered as branching tree, Chapter 74. The Lung, RG Crystal, JB West, and PJ Barnes (Eds.), Lippencott-Raven Inc., Philadelphia.

West, B. J., & Goldberger, A. L. (1987). Physiology in fractal dimensions. American Scientist, 75(4), 354-365.

Womersley, John R. "Method for the calculation of velocity, rate of flow and viscous drag in arteries when the pressure gradient is known." The Journal of physiology 127.3 (1955): 553-563.

Zhang, Z., & Kleinstreuer, C. (2002). Transient airflow structures and particle transport in a sequentially branching lung airway model. Physics of Fluids (1994-present), 14(2), 862-880.

Zhang, Z., Kleinstreuer, C., Donohue, J. F., & Kim, C. S. (2005). Comparison of micro-and nano-size particle depositions in a human upper airway model. Journal of aerosol science, 36(2), 211-233. Zhao, Y., & Lieber, B. B. (1994). Steady inspiratory flow in a model symmetric bifurcation. Journal of biomechanical engineering, 116(4), 488-496.